STAR FORMATION AND GALAXY EVOLUTION SINCE Z∼2: RESULTS FROM MULTIWAVELENGTH SURVEYS

A Dissertation

Presented to the Faculty of the Graduate School

of Cornell University

in Partial Fulfillment of the Requirements for the Degree of

Doctor of Philosophy

by

Drew Brisbin

May 2014

STAR FORMATION AND GALAXY EVOLUTION SINCE Z$\sim$2:

RESULTS FROM MULTIWAVELENGTH SURVEYS

Drew Brisbin, Ph.D.

Cornell University 2014

Our recent studies in galaxy evolution have revealed a surprising new paradigm of star formation. Contrary to the notion that major mergers play an increasingly dominant role going backwards in cosmic history, we find that over the last $\sim$10 Gyr, much of star formation has been fueled by accreting cold gas from the cosmic web. Accretion rates were presumably larger in the past, so star forming systems may have very different properties in the early Universe and today. Large scale astronomical surveys, such as the Herschel Multi-Tiered Extragalactic Survey (HerMES), and the Sloan Digital Sky Survey (SDSS) have provided a wealth of extragalactic data covering a statistically large number of sources. Targeted, niche surveys, like our fine structure line survey of star forming galaxies in the early Universe observed with the redshift (z) Early Universe Spectrometer (ZEUS) have provided detailed observations of high interest sources. We have made use of this diverse set of data to study galaxy evolution from the epoch of peak star formation at z=1-2 up to the present.

Data from HerMES is a reliable probe of infrared emission, particularly useful for characterizing the far infrared dust peak, and therefore determining star formation rates out to redshifts of a few. Deep integrations with the Herschel SPIRE photometer rapidly reach the confusion limit, tempering its utility in studying faint high redshift galaxies. With appropriate care taken to identify blended sources, however, HerMES data is useful in identifying bright, red-

shifted, star forming sources. We have compiled spectral energy distributions from HerMES and ancillary data and found that, even sources at high redshift are well fit by local star forming galaxy templates.

In the local Universe, spectroscopic SDSS data has allowed us to estimate crucial galaxy properties on $\sim 10^5$ sources, providing an opportunity to observe general statistical trends, and constrain theories of galaxy evolution. A toy model of cold flow accretion powered star formation reproduces the observed fundamental plane of galaxy stellar mass, metallicity, and star formation for small and medium mass galaxies.

Our fine structure line survey with ZEUS detected the [CII] 157.7 μm line in eight galaxies from the epoch of peak star formation at z=1-2. We augmented this survey with observations of the [OI] 63 μm line and far infrared photometry from Herschel, as well as Spitzer IRS spectra from the literature. Most of our sources have higher than average gas heating efficiency with $L_{[CII]}/L_{FIR} \gtrsim 10^{-2}$. We interpret the majority of them as being dominated by star formation powered PDRs, extending to kpc scales. In two sources there is evidence for enhanced [CII] emission due to heating by low velocity shocks. These findings are consistent with a picture of gas accretion fueling star formation on a near galaxy-wide scale.

In synthesizing this data we find a remarkable consistency in the nature of star formation over the last 10 Gyr. In contrast with the model of sustained hierarchical merging, we find that star formation since z$\sim$2 is fueled largely by cold flow accretion of gas from the cosmic web, which presents itself as moderate density star formation with correspondingly moderate UV fields.

BIOGRAPHICAL SKETCH

Drew Brisbin was born and raised in Minnesota. Early on in his youth Drew developed a strong interest in science and mischief, and spent several years narrowly avoiding burning down his house with a magnifying glass or being electrocuted by improperly discharged capacitors. Late in high school Drew discovered a latent talent for studying and turned his approach to experimentalism in a more scholarly direction.

Drew attended Carleton College in Northfield, MN where he honed his interests in science. In his first research experience as an undergraduate, he got a taste of scientific research, as well as a view of the Magellenic Clouds through the black night of the Warrumbungle Shire in New South Wales, Australia, which immediately convinced him to focus on astronomy. In his junior and senior years of college Drew studied pulsars under the guidance of his advisor, Joel Weisberg.

After graduating with a BA in physics in 2007 Drew immediately began a PhD program at Cornell University. His thesis work, conducted in the research group of Gordon Stacey and also under the guidance of Martin Harwit, focused on galaxy evolution, specifically examining the mechanisms of star formation in the nearby and high redshift Universe. In September 2013, Drew completed his thesis dissertation defense. Shortly thereafter he began his postdoctoral work at the North American ALMA Science Center (NAASC) in Charlottesville, VA.

This dissertation is dedicated to my parents, whose unwavering support made this work possible. Your love and confidence has driven me to find more in myself than I knew existed.

ACKNOWLEDGEMENTS

While I am the one who has at turns dreaded, agonized over, ignored, persisted in, and rejoiced over this thesis, its existence is only due to the incredible cast of people that have shaped my life. This is but a sample of the legions that have given me the character, knowledge, and opportunity to undertake this endeavor. Thank you.

- Cornell, the National Science Foundation, and NASA – Throughout graduate school I was supported by a variety of grants and scholarships. I would like to thank Cornell for the several research, teaching, and travel grants I received. ZEUS observations for this research were supported by NSF grants AST-0705256, AST-0722220, and AST-1109476. Herschel observations were supported by NASA. Without this support my work would not have been possible.

- HerMES collaboration – This research has made use of data from the HerMES project (http://hermes.sussex.ac.uk/). HerMES is a Herschel Key Programme utilising Guaranteed Time from the SPIRE instrument team, ESAC scientists and a mission scientist. HerMES is described in [Oliver et al., 2012]. The HerMES data was accessed through the HeDaM database (http://hedam.oamp.fr) operated by CeSAM and hosted by the Laboratoire d'Astrophysique de Marseille.

- Gordon Stacey – As an adviser and boss you have always been supportive, approachable, and a generally great person to work with, go to dinner with, or pull an all-night-proposal-writing session with. Furthermore, you've taught me the valuable lessons that 'better is the enemy of good enough' and that academic stress does not disappear with advancement. It's more or less a constant condition, and the real talent is being able to

deal with it.

- Martin Harwit – Thank you for exposing me to such a diverse set of research environments, always with confident guidance. While it was stressful at the time, throwing me into the deep end with the HerMES and PEP consortia gave me a confidence in asserting myself scientifically that I would otherwise have missed, and your diplomatic aplomb always saw me through. Your amazing breadth of knowledge and calm demeanor will continue to be an example for me.
- Mom and Dad – I simply can't put into words my thanks for the love and support you've given me for 29 years. You've provided me every opportunity available, encouraged my interests, pushed me to do my best, and occasionally worried about my decisions. (I'm sure I'll still occasionally make you worry, but at least now I can make those decisions with the authority of some fancy letters in front my name!)
- Abra – It does not take a PhD to realize, after following you to both Carleton and Cornell, that you have been an inspiration and a role model to me. Even though I'm taller now, I will always look up to you. We are alike in many ways, but I have always been amazed by your strength and bravery. I am at once admiring, and relieved you have been there to blaze a trail.
- Grandpa George – My grandfather was one of the kindest, smartest, and most sincere people I've known. I still remember him with the awe of a five year old. I didn't know exactly how he had become such a neat person, but I knew at least part of it had to do with him being that thing called a "scientist" and that's exactly what I wanted to be.
- Mr. C – It's a subtle thing to learn how to learn. Your teaching me this was

possibly the main domino that led to my motivation and success in high school, without which I probably wouldn't have made it to the college I did, and been able to walk the path that I have. Thank you.

- Joel Weisberg – At the time I may not have entirely appreciated arguing statistics with you, but in retrospect I am very thankful that you gave me my first real experience of working in academic research.
- Frances – You have been my rock. I cannot say enough thanks for the support you give me. Whenever I have doubt or fear you're there to help me. You kept me sane through the chaos of graduate school. I can only hope I'll repay the favor.
- Steve, Nora, Betsey, Ben – The best house mates a guy could have! There were probably times you wanted to kill me. But you didn't, and frankly that says a lot about our six years of struggling together as a houseful of anxious graduates trying to stave off living in the real world.
- Manolis, Carl, Betsey (again) – For six long years I learned what being a grad student was all about. Sure, I read the graduate student hand book and went to the graduate student meetings, but right through the end it was really watching you that showed me what an astronomy grad could, should, and *absolutely needed* to do. And I had some great times along the way.

TABLE OF CONTENTS

Biographical Sketch . . . iii
Dedication . . . iv
Acknowledgements . . . v
Table of Contents . . . viii
List of Tables . . . x
List of Figures . . . xi

1 Introduction **1**

2 The Deep SPIRE HerMES Survey: Spectral Energy Distributions and their Astrophysical Indications at High Redshift **7**
2.1 Introduction . . . 7
2.2 Primary Aims . . . 9
2.3 Data . . . 11
2.4 The Statistics of Purity Indices in GOODS-N and Lockman North 12
2.5 Spectral Energy Distribution of the Secure Sources . . . 16
2.6 The Nature of the Ultraluminous Sources . . . 20
2.7 Discussion . . . 27
2.8 Conclusions . . . 30

3 Galaxy Mass, Metallicity, Radius and Star Formation Rates **32**
3.1 Introduction . . . 32
3.2 Methods . . . 37
3.3 The Observed Galaxy Sample . . . 40
3.4 Infall and Metallicity Dilution of Native Gas . . . 43
3.5 A Mean-Field-Theory Toy Model . . . 51
3.6 Representative Values of s and V . . . 59
3.7 Difference Between Infall and Star Formation Rates, α . . . 62
3.8 Summary and Discussion . . . 64

4 Strong C^+ emission in galaxies at z$\sim$1-2: Evidence for cold flow accretion powered star formation in the early Universe **67**
4.1 Introduction . . . 67
4.2 Instrumentation and Observations . . . 72
4.3 Notes on observations of individual systems . . . 74
4.4 Results and analysis . . . 76
4.4.1 Line spectra . . . 77
4.4.2 Photometry and SEDs . . . 79
4.4.3 [CII] and the FIR continuum . . . 84
4.4.4 PAHs . . . 88
4.4.5 PDRs . . . 93
4.4.6 Individual sources . . . 94

4.5 Discussion 98
4.6 Conclusions 104

5 Overview, Conclusions, and Future work **107**
5.1 The Deep SPIRE HerMES Survey: Spectral Energy Distributions and their Astrophysical Indications at High Redshift 110
5.2 Galaxy Mass, Metallicity, Radius and Star Formation Rates 116
5.2.1 Extensions 118
5.3 Strong C^+ emission in galaxies at z$\sim$1-2: Evidence for cold flow accretion powered star formation in the early Universe 118
5.3.1 Extensions 121

A One example of SDSS sample summary tables from chapter 3. (Full set available online.) **132**

B Photometry used in SED fitting for chapter 4. **137**

LIST OF TABLES

2.1 HerMES deep field source Π values 15
2.2 Lockman North SED source data 19
2.3 GOODS-N SED source data 20
2.4 High redshift HerMES SED source data 27
2.5 IR to optical flux ratios in HerMES SPIRE sources 30

3.1 Oxygen abundances on the galaxy main sequence 42
3.2 Observed and modeled metalicities 45
3.3 Native gas metallicities 50
3.4 Typical main sequence galaxies model parameters 60

4.1 ZEUS observing log 74
4.2 Fine structure lines and FIR photometry. 79
4.3 Stellar masses and star formation rates 84
4.4 PAH features 91
4.5 PDR model parameter fits 100

5.1 Proposed multi-line ALMA sample 130

A.1 SDSS extracted sample size as a function of SFR and M_* 133
A.2 SDSS sample median Petrosian half light radius 134
A.3 SDSS sample median metallicity 135
A.4 SDSS sample metallicity standard deviation 136

B.1 Photometry used in fitting SEDs for [CII] sources 138

LIST OF FIGURES

1.1 Far infrared Lilly-Madau plot 3

2.1 GOODS-N 24 μm sources and Herschel SPIRE beam comparison 10
2.2 Isolated Lockman North galaxy SEDs 17
2.3 Isolated GOODS-N galaxy SEDs 18
2.4 Infrared source luminosities in deep HerMES fields as a function of z 21
2.5 Most luminous HerMES galaxy SEDs 26

3.1 Metallicity, star formation rate, and stellar mass relationship in SDSS galaxies 41
3.2 Metallicity dilution as a function of star formation rate 46
3.3 Scatter of ρ/α as a function of V 61

4.1 ZEUS/CSO [CII] spectra 77
4.2 Herschel PACS [OI] spectra 78
4.3 Example SEDs with and without scaling 81
4.4 Best fit SEDs 82
4.5 SFR vs. stellar mass 85
4.6 [CII]/FIR vs. L_{FIR} 86
4.7 [OI] 63 μm/[CII] vs. $F_\nu(60)/F_\nu(60)$ 87
4.8 [OI]/FIR vs. L_{FIR} 88
4.9 Spitzer IRS mid infrared PAH spectra 91
4.10 [CII] to PAH ratio vs. $\nu F_\nu(70)/\nu F_\nu(100)$ 92
4.11 PDR diagnostic plots 99
4.12 Star formation schematic representation 102

5.1 HerMES galaxies refit with scaled SEDs 113
5.2 Representative apparent SEDs in confused sources 115
5.3 Spitzer IRS spectrum of 3C 368 122
5.4 [NII] line ratios as an indication of ionized gas electron density . 126
5.5 [CII], [OI] 145 μm, and FIR PDR diagnostic plot 128

CHAPTER 1

INTRODUCTION

The recent ability to observe large numbers of distant galaxies over vast swaths of the electromagnetic spectrum has brought new insight to the long-standing field of galaxy evolution. The methods used to understand galaxies have changed over time, from the empirical cataloging of galaxy morphology by Hubble, to the mathematical star formation / gas pressure models of Schmidt-Kennicutt [Schmidt, 1959, Kennicutt, 1998a], to sophisticated computer particle simulations that include dark matter and stellar feedback [c.f. Springel et al., 2005, Bower et al., 2006, Guedes et al., 2011]. The common thread is that, to be viable, any galaxy relationship or theoretical model must ultimately explain current knowledge and make predictions for future tests.

Galaxy stellar mass, star formation rates, and metallicity are particularly well defined quantities that can be readily measured through various means. While these three data points present a rather Spartan picture of a galaxy, they roughly encapsulate its summed history including star formation, violent merging events, and the creation of new elements. A simple collection of these data extending back in time for a large fraction of the Universe's history represents the formation and subsequent evolution of galaxies. Additional data in the form of spectral lines characterizing radiation fields, densities, and activity of a central engine yield a richer description with a detailed view of the physics powering particular galactic phenomena.

The picture of galaxy formation is complicated with various timescales and punctuated events. Galaxies are thought to have initially formed through hierarchical clustering - a process describing a 'bottom up' formation scenario in

which small structure emerged first from the nearly homogenous soup of the early Universe, and this small structure gradually coalesced, merging into larger and larger systems, eventually forming the collections of gas and stars that we recognize today as galaxies. This picture is usually invoked to explain the earliest formation of galaxies at z$\sim$7 [Bouwens and Illingworth, 2006]. Structural merging continues today, as shown by the occurence of major mergers between galaxies of nearly equal mass that can be seen at various stages of relaxation. Locally, we see examples in the beautiful morphology of interacting systems such as the Antennae, or the Mice galaxies [Whitmore and Schweizer, 1995, Burbidge and Burbidge, 1959]. At higher redshifts we can see evidence for recent mergers in the disturbed morphologies and obvious collisions apparent in both optical (HST) and mm-wave interferometric images [e.g. van Dokkum et al., 1999, Tacconi et al., 2006, Kocevski et al., 2012].

The counterpart to major merger growth is the concept of cold flow accretion, whereby large galaxies grow by accreting streams of intergalactic gas. These two modes of galaxy growth both occur to varying degrees in individual galaxies. One of the major questions then is what are the visible effects of these forms of galaxy growth and how has the prevalence of mergers and cold flow accretion changed throughout the history of the Universe?

Work by S. Lilly and Piero Madau (and followed up by many others [e.g. Lilly et al., 1996, Madau et al., 1996, Dunne et al., 2009, Magnelli et al., 2011, Wang, 2013]) has tracked star formation rate densities of the Universe over the last several Gyr. As shown in Figure 1.1, there is a clear order of magnitude rise in star formation density going back in time to z$\sim$2. The cause of this dramatic change is not obvious, but since star formation and galaxy mass growth are in-

extricably linked, we might expect that a shifting dominance in the mechanism of galaxy growth might lead to observable differences in the resulting star formation. A galaxy that has recently undergone a violent merger, for instance, will look significantly different (in terms of available gas, morphological structure, extent and intensity of star formation, and possibly presence and activity of a central engine,) than a galaxy that has grown quiescently through gas accretion for the last several Gyr.

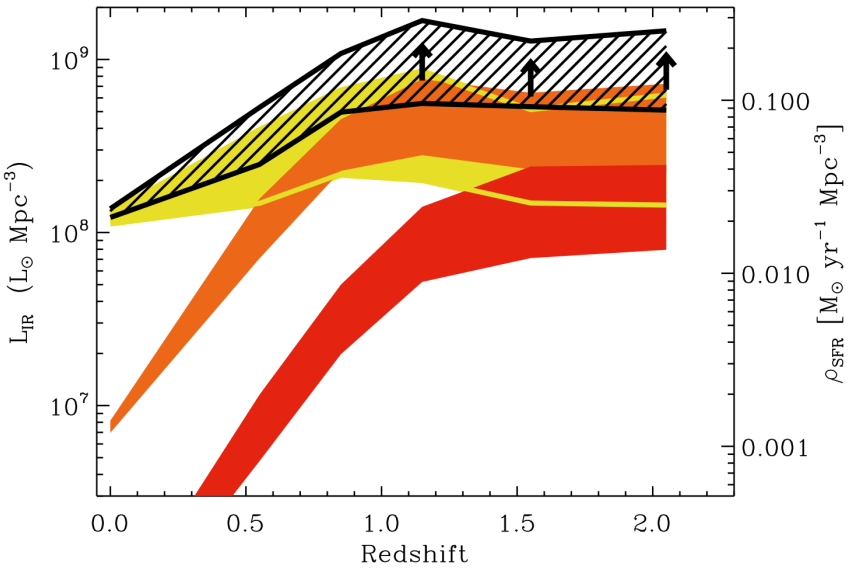

Figure 1.1 A 'Lilly-Madau' plot showing the comoving total infrared (8-1000 μm) energy density (left axis) and the corresponding star formation rate density (right axis) assuming a Salpeter IMF as a function of redshift out to z$\sim$2. The red region represents contributions from ULIRGs ($L_{IR} > 10^{12} L_\odot$), the orange region represents contributions from LIRGs ($L_{IR} > 10^{11} L_\odot$), the yellow region represents contributions from normal galaxies ($10^7 < L_{IR}/L_\odot < 10^{11}$), and the black hashed region represents the total. There is a clear increase in the star formation rate density moving from z=0 to z=1, as well as a trend for increasing contributions from LIRGs and ULIRGs. Figure reprinted from Figure 9 of Magnelli et al. [2011].

Complicating the picture are the detailed roles of stellar and AGN feedback, and the effect of changing metallicity on star formation. Observed properties express the sum total of all these effects. Connecting those observations with

the abstract concepts, however, requires detailed models and simulations which must include all significant galactic influences and observed data. Only recently are we beginning to understand the range and variation in galaxy properties throughout the history of the Universe. We are finally able to tentatively suggest outlines for the individual ingredients (such as a rough idea of star formation history to z$\sim$4, and metallicities of high redshift quasars and local host galaxies.) Now the challenge is putting together those ingredients to make a unifying picture.

Technology is now coming of an age that enables us to obtain the data necessary to study these questions. The advent of mega-project astronomy has allowed deep iconic surveys that give 'whole cloth' representations of the Universe across many portions of the electromagnetic spectrum. Far infrared observations have proven particularly invaluable for their ability to probe the cool dust peak and observe fine structure lines emanating from the hearts of otherwise obscured dense molecular clouds. The Herschel Multi-tiered Extragalactic Survey (HerMES) is a blind 'wedding cake' style survey covering portions of several well known, low Galactic foreground extinction fields [Oliver et al., 2012]. These fields have been covered at several other wavelengths, but HerMES represents the deepest and most resolved far infrared view yet, providing the keystone that supports our understanding of dusty high-z galaxies. The Sloan Digital Sky Survey (SDSS) of $\sim$35% of the entire sky provides the largest optical and near infrared survey of the sky to date. Other optical surveys provide deeper views in select regions, and most of the data in the SDSS extends only out to relatively low redshifts covering the Universe's most recent epoch, but it provides an amazing breadth of coverage, allowing statistical compilation of galaxy properties over much of the Northern sky. These surveys have proven

instrumental in discovering the global composition of our Universe.

Small, targeted surveys, often motivated by specific science research goals, are equally crucial in understanding the Universe. They can specifically target astrophysically interesting and accessible sources, providing necessary data to understand an underlying physical process at work in individual sources and therby serve as a microcosm of the processes at work in the Universe as a whole. In this vein, the spectroscopic mini-surveys undertaken by ZEUS at redshifts z=1-2 have been instrumental in illuminating the nature of galaxies during the epoch of peak star formation.

In this dissertation I present work that I have undertaken in my six years at Cornell University to understand the nature of galaxy evolution. In doing so I have largely focused on the following questions:

- What are the defining galaxy populations at high redshift?
- How has galaxy luminosity and star formation changed in the last 10 Gyr?
- What influences the process of metal enrichment in the last 3 Gyr?
- Does star formation proceed in the early Universe through the same modes as it does locally?

In chapter 2 I address the ability to extract meaningful properties from the deepest and longest wavelength HerMES observations, and compare the overall Spectral Energy Distributions (SEDs) of high redshift galaxies to local galaxy models. In chapter 3 I investigate the statistical relationship between galaxy mass, size, and metal enrichment in relatively nearby galaxies ($0.07 < z < 0.3$.) In chapter 4 I use the spectroscopic mini-survey results from ZEUS to analyze

the energetics, dynamics, and ultimately the star formation in a small, but potentially representative, set of star forming high redshift galaxies. The first two chapters represent published work, while the third represents work submitted for publication. In chapter 5, I summarize my conclusions from this work, provide updated commentary, and describe relevant extensions of this work that are underway or that I plan to work on in the future. Note that in chapters 2 and 4 I make use of the various terms, 'sub-millimeter,' 'infrared,' 'far infrared,' and 'total infrared.' The exact meaning of the terms remains consistent and well defined within each chapter, but changes slightly between them.

CHAPTER 2

THE DEEP SPIRE HERMES SURVEY: SPECTRAL ENERGY DISTRIBUTIONS AND THEIR ASTROPHYSICAL INDICATIONS AT HIGH REDSHIFT

2.1 Introduction

The Herschel Space Observatory[1] is a satellite mission launched by ESA in May 2009 [Pilbratt et al., 2010]. Herschel has three instruments: a far-infrared photometric camera and imaging grating spectrometer, PACS [Poglitsch et al., 2010], a far-infrared - sub-millimeter heterodyne receiver, HIFI [de Graauw et al., 2010], and a sub-millimeter photometric camera and imaging Fourier transform spectrometer, SPIRE [Griffin et al., 2010]. Herschel's primary aperture is 3.5 m and the instrumentation delivers near diffraction limited performance in all modes with very high sensitivity Herschel science observations began in September 2009 and the cryogenics lasted 3 years and 7 months, ending its mission on April 29 2013. To date more than 763 papers based on Herschel data have appeared [2].

Herschel has opened wide astronomical access to the far-infrared / submillimeter (FIR/SMM) spectral range. With the Spectral and Photometric Imaging Receiver (SPIRE), deep cosmological surveys are studying galaxies out to redshifts of order $z \sim 3$, reaching back to epochs when the Universe was only a few

*This chapter is an adapted version of the published article Brisbin et al. (2010).

[1]Herschel is an ESA space observatory with science instruments provided by European-led Principal Investigator consortia and with important participation from NASA.

[2]http://herschel.esac.esa.int/hpt/publicationlist.do

billion years old.

A primary motivation for these surveys, as well as those undertaken with the Photodetector Array Camera & Spectrometer (PACS) aboard Herschel, is to gain improved spectral energy distributions (SEDs) of astronomical sources. With an appropriate redshift, integration of the flux densities demarcated by the SEDs permits derivation of rest-frame luminosities, star-formation rates, and other physical properties of galaxies.

Among the first observations undertaken by SPIRE in the Herschel Multi-tiered Extragalactic Survey (HerMES[3]) project [Oliver et al., 2010] have been surveys of galaxies in GOODS-N and Northern portions of the Lockman Hole (LN) field [see Oliver et al. [2010] for a description of these early observations.] Source confusion, as defined and discussed in detail by Takeuchi and Ishii [2004], results in blending of far-infrared sources and complicates the analysis of survey data. In light of the large degree of source blending expected at SPIRE wavelengths, novel options for source extraction have been pursued [[Roseboom et al., 2010], [Béthermin et al., 2010]]. Rather than looking for sources based on SPIRE intensity maps alone or relying on traditional source detection and extraction techniques for the SPIRE data, which are heavily affected by confusion, Roseboom et al. [2010] measure the SPIRE flux at the position of known 24 μm sources using a linear inversion technique to account for source blending. The rationale for this is provided by the results of the Balloon-borne Large Aperture Submillimetre Telescope (BLAST) extragalactic survey [Marsden et al., 2009], which showed that the 24 μm and the FIR flux densities are at least statistically correlated.

[3]hermes.sussex.ac.uk

2.2 Primary Aims

The aims of this paper are twofold; our primary aim is to derive spectral energy distributions for distant galaxies observed by SPIRE. Before this can be achieved, however, a robust way of identifying sources least affected by confusion and blending must be devised.

The GOODS-N catalogue of Roseboom et al. [2010] provides a cross-identification (XID) of FIR/SMM flux density at 250, 350 and 500 μm with 1951 possible 24 μm counterparts having minimum flux densities of 20 μJy. Many of the identified 24 μm galaxies are further cross-identified with ultraviolet, optical, near-infrared (NIR) and radio counterparts. The survey covered a 12.3×18.6 arc minute strip, corresponding to $\sim$230 arcmin^2

The SPIRE beam diameters at full-width-half maximum (FWHM) respectively measure 18.1, 25.2 and 36.9 arcsec at 250, 350 and 500 μm. For present purposes, we take the beams to be close to circular; their ellipticity varies from pixel to pixel, but is approximately 1.08 ± 0.05, the longer direction lying in the spacecraft horizontal direction, parallel to the ecliptic plane (Bernhard Schulz, private communication.) The beam at 500 μm thus has an area $\sim$0.3 arcmin^2. With 1951 possible 24 μm sources, we can expect a typical 500 μm beam to contain 2.5 possible sources. At 250 μm the crowding is a factor of 4 less severe, but still appreciable. An example of the crowded source distribution is seen in Figure 2.1 where the SPIRE beam outlines are overlaid on a patch of the GOODS-N field centered on a 24 μm source.

In the Northern Lockman region, a 40.1′ $\times$ 36.2′ segment of the sky yielded 6316 possible 24 μm counterparts with minimum flux densities of 50 μJy in an

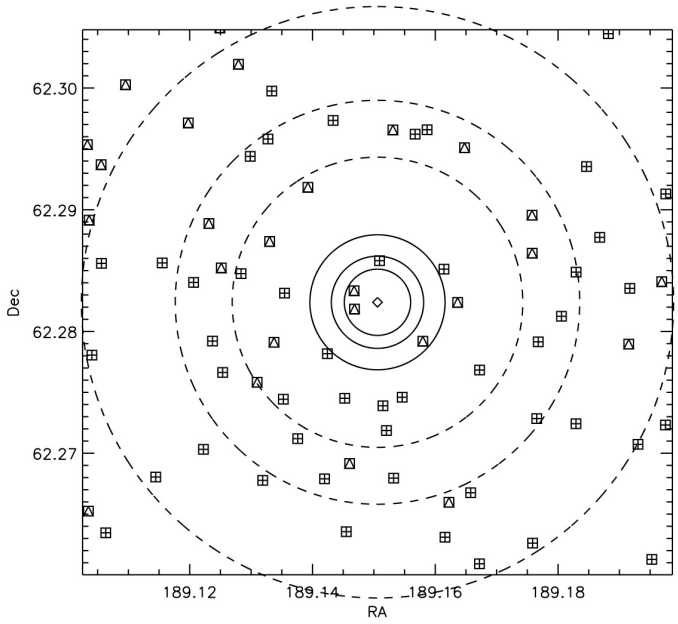

Figure 2.1 A GOODS-N SPIRE and 24 μm source with equatorial coordinates (J2000.0) 189.1506 / 62.2824 shown as a diamond with nearby 24 μm sources. Known ambient 24 μm sources are shown as squares with nested symbols. Plus signs indicate sources with known redshifts and triangles indicate sources with unknown redshift. The spatial distribution of 24 μm sources is based on the XID information in Roseboom et al. [2010]. Solid circles represent the full-width-half-maxima (FWHM) of the Airy profile PRF at the three SPIRE wavelengths and dashed circles represent the second Airy minimum. Coordinates are in J2000.

area subtending $\sim$1500 arcmin^2 — again corresponding to more than 1 potential 500 μm source per beam. Identification of sources least affected by confusion and blending is therefore important. These sources have also been cross-identified at multiple wavelengths and assigned photometric redshifts as detailed in Strazzullo et al. [2010].

2.3 Data

Using the existing high spatial resolution Spitzer 24 μm data and the known far-infrared instrumental point response function (PRF) as inputs, Roseboom et al. [2010] determined best-fit 250, 350, and 500 μm fluxes by a procedure they detail in their paper. In each SPIRE wavelength band, their tabulated cross-identifications provide both their best estimate of the flux density F_ν and the flux density PRF_ν in a PRF-convolved map centered on the position of an associated 24 μm source. They make no assumptions about a proportionality between 24 μm and FIR flux densities, but assume that SPIRE sources will only be detected at positions of 24 μm sources. For each source, ancillary data at other wavelengths are included, as well as several flags that can be used to identify degenerate cases. Of particular importance is the redshift of the associated 24 μm source, which enables derivation of rest-frame SEDs and thus source luminosities. Wherever we refer to F_ν and PRF_ν in the remainder of this paper these quantities are to be thought of as those defined by Roseboom et al. [2010].

The flux density in a PRF-convolved region centered on the position of the 24 μm galaxy associated with each far-infrared source represents the system response not only to the flux density attributed to this source (referred to as $F_\nu\big|_\lambda$) but also to contributions from nearby sources. It thus provides a measure of blending characterizing each source. We define a *purity index* Π_λ for each source as the ratio

$$\Pi_\lambda = F_\nu / PRF_\nu\big|_\lambda \,, \tag{2.1}$$

where λ specifies the wavelength band, 250, 350, or 500 μm, and $PRF_\nu\big|_\lambda$, as

[1]Herschel is an ESA space observatory with science instruments provided by European-led Principal Investigator consortia and with important participation from NASA.

[2]hermes.sussex.ac.uk

supplied in the XID catalogs by Roseboom et al. 2010 is the PRF-smoothed flux density at the position of the source.[3] A high value of Π_λ indicates low confusion and blending in wavelength band λ; a low value indicates high blending. The fractional contributions by ambient sources to the PRF-convolved flux density within a PRF is simply $(1 - \Pi_\lambda)$. In principle, the purity index must assume values $0 \lesssim \Pi_\lambda \lesssim 1$. In practice, however, the value F_ν has been calculated *on top of* a locally determined background, whereas the PRF_ν values do not take a local background variation into account. This can result in $\Pi_\lambda > 1$ when a negative local background or "baseline" has been used.

2.4 The Statistics of Purity Indices in GOODS-N and Lockman North

We have found it useful to identify sources whose purity indices respectively exceed Π_λ measures of 0.7, 0.5, and 0.3 at 250, 350, and 500 μm. We say that a source is *secure* at each wavelength if it meets this criterion. If the source is found to be secure in all three wavelength bands, we call it *triply secure*. High-purity sources are of special interest because their isolated nature makes them less susceptible to blending by neighbors. It is these sources which will be especially useful for follow up studies with other instruments and also may provide confirmation of the deblending approach used. It should be noted, however, that a flux density estimate from a highly pure source might still be inaccurate if there is significant contribution from an infrared source that is not observed

[3]Our $PRF_\nu \mid_\lambda$ corresponds to the quantity $\mathbf{d}$ in equation (2) of Roseboom et al. 2010, convolved with the point response function centered on the primary source whose flux is $F_\nu \mid_\lambda$. The entries in the XID tables list our $F_\nu \mid_\lambda$ as $F(\lambda)$, and our $PRF_\nu \mid_\lambda$ flux density as $PRF(\lambda)$.

at 24 μm. Furthermore, sources with low purity do have well-defined deblending solutions and hence well-characterized flux densities and uncertainties from Roseboom et al. [2010]. In crowded fields, the true flux density is very likely described by this characterization, although the margins of uncertainty tend to be large. Our choice of purity criteria is somewhat subjective but offers a reasonable compromise for extracting relatively reliable SEDs despite source blending. Understandably, these criteria may be expected to vary depending on the type of information an astronomer expects to extract from the survey data.

When a reliable redshift is available, the single most important quantity that can be determined from an SED is source luminosity. With this, one can begin discussing the luminosity distribution at specific redshifts, as well as luminosity evolution as a function of redshift, particularly among ultraluminous galaxies that emit the dominant fraction of their energy in the infrared. However, to obtain a reliable SED and thus a reliable luminosity, we require sources whose flux densities are well determined at all three SPIRE wavelengths in order to optimally constrain the flux density defining the broad wavelength region around peak emission.

To explain the consequences of our choice of purity criteria in this context, we may consider a toy model which, as pointed out in Section 2.1, will respectively exhibit an average number of sources $n_\lambda \sim 2.5$, 1.225, and 0.625 per GOODS-N beam, at 500, 350, and 250 μm. Let us inject an additional source into such a beam and call it the primary source. If all the sources involved are equally bright, on average, i.e., make equal contributions to the PRF-smoothed flux density, the purity of the primary source will be $\Pi_\lambda = (1 + n_\lambda)^{-1}$, i.e. 0.29, 0.45, and 0.62, respectively at 500, 350 and 250 μm. Half the sources in each

waveband will have purities higher than these purity cuts, and half lower.

Turning now to our preferred adoption of purity cuts of 0.3, 0.5 and 0.7 at 500, 350, and 250 μm, we see that they assure two properties: (i) that they yield sources whose purities are above average at all three wavelengths, and (ii) that the fraction of sources with purity above the cut is roughly comparable at all three wavelengths — a balance, which is important to assure a well-defined SED. Table 1, described below, confirms these traits for the GOODS-N sample. It shows that a fraction $f_\lambda = 0.23$ of the sources has purity exceeding 0.7 at 250 μm, a fraction 0.32 exceeding purity 0.5 at 350 μm, and a fraction 0.36 exceeding purity 0.3 at 500 μm. These fractions cluster around a value of 0.3, thus lending roughly equal weight to the flux density in each waveband in the determination of the SED.

In Table 1, we list the fraction of sources in GOODS-N and LN whose purity indices lie above certain cuts. We permit these indices to slightly exceed a value of one, with a cut-off of $\Pi = 1.1$ in GOODS-N and $\Pi = 1.2$ in LN. These relaxed upper limits are designed to allow the inclusion of detections with a significant local background which otherwise have all the earmarks of being secure.

In the GOODS-N region the XID catalog lists 183 sources observed at all three wavelengths and with known redshift, 16 of which are triply secure. If we remove the upper limit $\Pi = 1.1$, the number of triply secure sources rises to 59. In LN there are 633 sources with detections in all three SPIRE bands and the two selected PACS bands (100 and 160 μm) with known redshift, 165 of which are triply secure; this number increases to 287 if we remove the upper limits on purity. Although the numbers of these galaxies are quite modest, they nevertheless yield informative statistics on the luminosities and luminosity distributions

Table 2.1 Fraction of detected SPIRE sources in the GOODS-N and LN with a Π_λ value greater than the threshold indicated in the top row. For the GOODS-N and LN regions we place an upper limit cut-off on Π_λ of 1.1 and 1.2 respectively. The columns marked 'detections' denote the total number of SPIRE sources detected at a given wavelength in the present HerMES project.

GOODS-N					
$\Pi >$	0.9	0.7	0.5	0.3	detections
250 μm	0.106	0.231	0.348	0.493	1032
350 μm	0.069	0.199	0.316	0.451	697
500 μm	0.061	0.141	0.227	0.362	475
LN					
$\Pi >$	0.9	0.7	0.5	0.3	detections
250 μm	0.275	0.435	0.579	0.703	4646
350 μm	0.184	0.343	0.500	0.670	2968
500 μm	0.144	0.281	0.419	0.570	2127

of galaxies observed out to redshifts $z \sim 3$. These will be discussed in Section 2.6.

The larger aperture of the Herschel telescope and the higher spatial resolution this enables have permitted the SPIRE surveys to reach depths beyond those attained by BLAST. Nevertheless, Marsden et al. [2009] succeeded in acquiring reliable measurements of stacked source flux densities at comparable wavelengths. Their results indicate surface brightnesses of 8.60 $\pm$ 0.59, 4.93 $\pm$ 0.34, and 2.27 $\pm$ 0.20 nW m^{-2} sr^{-1} at 250, 350, and 500 μm respectively. These stacked source flux densities represent the major component of the cosmic infrared background (CIB) which was measured by the Cosmic Background Explorer's Far-Infrared Absolute Spectrometer (FIRAS) to be 10.4 $\pm$ 2.3, 5.4 $\pm$ 1.6, and 2.4 $\pm$ 0.6 nW m^{-2} sr^{-1} at 250, 350, and 500 μm respectively [Fixsen et al., 1998]. To investigate the extent to which this background is resolved with Herschel, we summed the estimated flux densities for our secure SPIRE sources in the deepest field (GOODS-N) and then attributed this flux density to the entire survey region of 230 arcmin^2. Using the flux densities for sources contained in

the XID catalog of Roseboom et al. [2010], our cumulative surface brightness for GOODS-N at 250, 350, and 500 μm is 1.49, 0.70, and 0.41 nW m^{-2} sr^{-1} or 14%, 13%, and 17% of the estimated CIB. At 250 and 350 μm these values are within 1σ of those corrected for blending and incompleteness by Oliver et al. [2010].

2.5 Spectral Energy Distribution of the Secure Sources

Figures 2.2 and 2.3 exhibit SEDs for triply secure sources in LN and GOODS-N. For LN sources, we have set an additional criterion for inclusion, namely that they have observed flux densities also at PACS wavelengths of 100 and 160 μm. Along with examining the observed SED, we show a fit using starburst models developed by Siebenmorgen and Krügel [2007] (S&K). These models are based on a nuclear concentration of massive young stars embedded in a matrix of gas and dust referred to as "hot spots". S&K use a five parameter SED fit which incorporates a variable nuclear bulge size with old and new stellar components as well as the effects of dust. They provide their models in the form of a library of 7000 SEDs available as text files online.[4] By using their models, we are able to not only find realistic intrinsic luminosities, but also star formation rates (SFR) for highly luminous sources at high redshift for which the Kennicut infrared - SFR relations apply [Kennicutt, 1998a].

The S&K model fits observations quite well, although some of our SEDs exhibit considerable deviations from the data at visible and near infrared wavelengths. This is largely due to variable shielding of starlight by dust, see Section 2.6 below.

[4]The S&K SED library of models is available at http://www.eso.org/$\sim$rsiebenm/sb_models/.

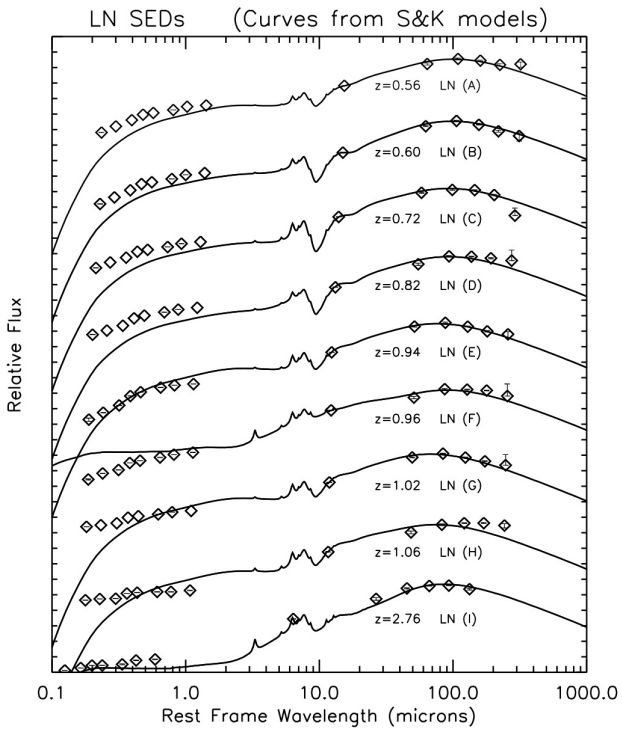

Figure 2.2 Lockman N galaxy SEDs plotted with arbitrary flux density offsets. These galaxies all met or exceeded our selection criteria of being securely identified at all three wavelengths, having a high purity index, (30%, 50%, and 70% pure at 500, 350, and 250 μm respectively), having known PACS detections at 100 and 170μm, and having known redshifts, $z > 0.5$. Each tick mark on the y-axis indicates a change by a factor of 10. Observed flux densities are indicated by diamonds. For most observations the error bars are smaller than the diamond; however for LN sources C, D, F, and G the 500 μm measurement is compatible with zero, so we have plotted only the upper error bar. The solid line is an S&K model fit to the 24 μm through 500 μm error-weighted observations. We weighted the 24 μm observations only a quarter as heavily as the longer wavelengths which play a dominant role in determining starburst luminosities. Observational data shortward of 24 μm is plotted for reference but not used in fitting. Source Πs are shown in Table 2.2. As with many of the examples quoted by S&K, the visual component of the SED often needs to be fitted by hand because it bears little relation to the starburst characteristics responsible for the mid- and far-infrared flux densities. The extent to which visible stars may or may not contribute to the SED is determined in part by the degree to which an older population of stars is obscured by dust without significantly contributing to its heating or by massive young stars whose shrouding by dust has gradually declined. Shrouding by dust may explain the significant drop in optical luminosities exhibited by some of the sources at the shortest wavelengths.

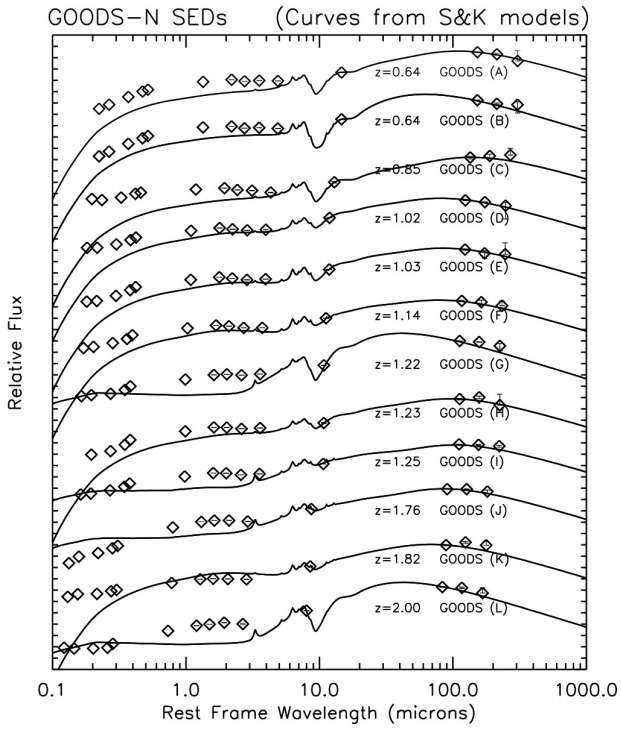

Figure 2.3 GOODS-N galaxy SEDs plotted as in Figure 2.2. The 500 μm measurements for GOODS sources A, C, E, F, H, K, and L are compatible with zero, so here we plot only the upper error bar, barely visible within the diamond symbol. As in Figure 2.2, we weighted the 24 μm data a quarter as heavily as the longer wavelengths. Observational data shortward of 24 μm is plotted for reference but not used in fitting.

In Figures 2.2 and 2.3, we have focused on high redshift (z$>$0.5) sources as these are of greatest interest to star formation history. Tables 2.2 and 2.3 show the luminosities and star-formation rates of galaxies whose SEDs are shown in Figures 2.2 and 2.3. The models appear capable of correctly representing the galaxies we observe, most of which are highly luminous and likely to be starbursts. Like most current models, however, vastly different dust masses and nuclear sizes are able to yield similar SEDs, as witnessed by the large differences in dust masses assigned to some galaxies listed in Tables 2.2 and 2.3 that have nearly identical redshifts and luminosities. This is not surprising because the models are only required to provide sufficient dust to convert most of the visible

Table 2.2 Data on LN Galaxies whose SEDs appear in Figure 2.2. We list the ID as established by Roseboom et al. [2010], right ascension and declination (J2000), photometric redshift $z > 0.5$, our purity indices Π_λ, total bolometric luminosity as estimated by an S&K model, star formation rate based on the infrared luminosity relation [Kennicutt, 1998a], and dust mass estimated by the S&K model. Along with these derived parameters, we list the model parameters: nuclear radius, visual extinction to center (A_v), and gas density within hotspots (n) in cm^{-3}.

ID	RA	Dec	z	L_{bolo} ($L_\odot$)	SFR ($\frac{M_\odot}{yr}$)	M_{dust} ($M_\odot$)	Π_{250}	Π_{350}	Π_{500}	Radius (kpc)	A_v	Log(n)
LN (A)	161.8365	59.1211	0.56	4.0×10^{11}	66	1.6×10^{8}	0.89	0.67	0.74	3.0	35.9	3
LN (B)	161.5001	58.8732	0.60	7.9×10^{11}	130	3.2×10^{8}	0.74	0.62	0.88	3.0	72.0	4
LN (C)	161.1277	59.1956	0.72	1.3×10^{12}	210	3.2×10^{8}	1.10	1.00	1.07	3.0	72.0	2
LN (D)	161.3232	59.2086	0.82	1.3×10^{12}	210	3.2×10^{8}	0.88	0.80	0.98	3.0	72.0	4
LN (E)	161.0530	59.0762	0.94	2.0×10^{12}	330	1.6×10^{8}	0.92	0.65	0.69	3.0	35.9	3
LN (F)	161.3680	59.2242	0.96	2.5×10^{12}	400	3.6×10^{8}	0.96	0.97	0.56	9.0	9.0	4
LN (G)	161.3429	59.2269	1.02	4.0×10^{12}	650	1.6×10^{8}	0.89	0.87	0.64	3.0	35.9	2
LN (H)	161.4871	58.8886	1.06	2.5×10^{12}	410	1.6×10^{8}	0.76	0.82	0.93	3.0	35.9	2
LN (I)	161.8669	58.8708	2.76	2.5×10^{13}	4300	4.9×10^{9}	0.91	0.96	0.77	9.0	120.0	4

and ultraviolet radiation produced in the starburst into infrared radiation at the observed temperature. If this criterion is satisfied, the models produce roughly correct SEDs.

While these figures and tables emphasize the relatively few triply-secure SEDs among high redshift objects, it is important to note that for many statistical trends, triple-security is not necessary. In Figure 2.4, we show the luminosities we have determined as a function of redshift, based on the S&K models for all sources in GOODS-N and LN that have detections of any kind (secure or not) at all three SPIRE bands. While some of the flux densities, especially at 500 μm, are quite uncertain (see Figures 2.2 and 2.3), this will not greatly affect the overall luminosity distribution. We estimate the source luminosity uncertainty to be $\sim$20%. The minimum detectable luminosities follow the expected trend of increasing with the square of luminosity distance (which we determined based on an $\Omega = 1$, $\Lambda = 0.7$, $H_0 = 70$ km s^{-1} Mpc^{-1} cosmology).

Table 2.3 Data on GOODS-N galaxies whose SEDs appear in Figure 2.3, listed as in Table 2.2. The redshifts here are spectroscopic.

ID	RA	Dec	z	L_{bolo} ($L_\odot$)	SFR ($\frac{M_\odot}{yr}$)	M_{dust} ($M_\odot$)	Π_{250}	Π_{350}	Π_{500}	Radius (kpc)	A_v	Log(n)
GOODS (A)	189.0274	62.1643	0.6380	5.0×10^{11}	84	3.2×10^{8}	0.83	0.84	0.44	3.0	72.0	4
GOODS (B)	189.3938	62.2898	0.6402	2.0×10^{12}	340	6.0×10^{7}	0.98	0.64	0.90	1.0	119.0	2
GOODS (C)	189.2979	62.1820	0.8549	1.3×10^{11}	21	3.2×10^{8}	1.00	0.81	0.74	3.0	72.0	4
GOODS (D)	189.1403	62.1683	1.0160	1.6×10^{12}	260	1.6×10^{8}	0.99	0.75	0.54	3.0	35.9	3
GOODS (E)	189.0633	62.1691	1.0270	1.3×10^{12}	210	1.6×10^{8}	0.92	0.52	0.45	3.0	35.9	2
GOODS (F)	189.3171	62.3541	1.1440	1.0×10^{12}	160	8.1×10^{7}	0.73	0.68	0.68	3.0	17.9	2
GOODS (G)	189.1438	62.2114	1.2242	2.5×10^{13}	4300	6.0×10^{7}	0.88	0.89	0.98	1.0	119.0	4
GOODS (H)	189.2137	62.1810	1.2258	6.3×10^{11}	100	1.6×10^{8}	0.71	0.83	0.31	3.0	35.9	4
GOODS (I)	189.2614	62.2338	1.2480	1.3×10^{12}	200	3.6×10^{8}	0.98	0.93	0.97	9.0	9.0	4
GOODS (J)	189.2566	62.1962	1.7600	6.3×10^{12}	1000	7.3×10^{8}	1.02	1.04	1.03	9.0	18.0	4
GOODS (K)	189.3036	62.1955	1.8150	2.0×10^{12}	310	8.1×10^{7}	1.08	0.86	0.50	3.0	17.9	3.4
GOODS (L)	189.0764	62.2640	2.0000	2.0×10^{13}	3400	6.0×10^{7}	0.82	0.71	0.33	1.0	119.0	2

Throughout this paper we refer to multiple luminosities, namely total bolometric luminosity and infrared luminosity integrated over 8 - 1000 μm [as used in star formation estimates by Kennicutt [1998a]]. For our purposes, the difference between the two is small as the majority of a luminous star-forming galaxy's energy is emitted in the infrared. In galaxies with $L_{IR} \gtrsim 10^{11.5} L_\odot$, Buat et al. [2010] find that ∼95% of the total star formation rate is accounted for by L_{IR}. Nonetheless, we explicitly differentiate between the two when the distinction is significant.

2.6 The Nature of the Ultraluminous Sources

As Figure 2.4 attests, our surveys reveal a number of highly luminous sources, mainly at redshifts between $z = 2.5$ and 3.2. Discussing all of these in detail is beyond the scope of the present paper, if for no other reason than that information on these sources is still quite modest. Nevertheless, we here discuss four of these sources to show that their luminosities appear to be intrinsic.

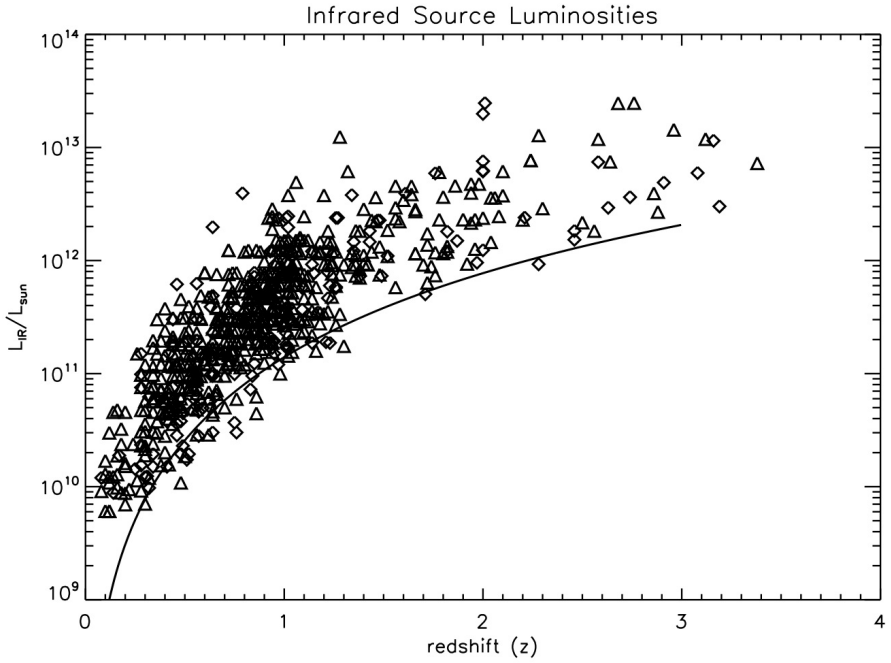

Figure 2.4 Infrared source luminosities (integrated over 8-1000 μm) in GOODS-N and LN plotted as a function of redshift for all sources detected at all three SPIRE wavelengths. Diamonds indicate GOODS-N luminosities obtained from SEDs fitted by S&K models, and triangles indicate similar luminosities for LN sources. The solid line shows the growth of luminosity distance squared with z. It serves as a rough lower bound to the luminosities in our selection of observed sources; the scatter of data points about the curve provides a visual impression of the uncertainties in those luminosities.

Neither gravitational lensing nor blending from neighboring sources appear to contribute significantly to the observed luminosities. This may not be true of all of the luminous SPIRE sources, but it appears to be so for at least those about which we have the most information right now. A number of other uncertainties also warrant comment.

(i) For most of the sources observed in LN only photometric redshifts are available. For the more luminous sources shown, estimated redshift errors range from ~ 6 to 17% in the catalogs of Roseboom et al. [2010]. Because calculated luminosities are proportional to $(1+z)^2$, a 17% error at $z = 2.5$ can lead

to a luminosity error in the range of $\sim 23 - 26\%$. For sources with established spectroscopic redshifts, the uncertainty is far smaller and can be neglected.

(ii) A second area of concern is discrimination between intrinsically luminous sources and sources that may be lensed by foreground galaxies to merely appear luminous. For some purposes, e.g. accounting for sources contributing to the diffuse background, this distinction may not be of primary importance; but for charting the luminosities of distant sources their intrinsic luminosities need to be determined.

(iii) Because our deep surveys are highly sensitive, they reveal a large number of faint sources. This leads to potential mis-identification of sources. It can also lead to blending. But seven of the eleven ultraluminous sources in Figure 2.5 and Table 2.4 are triply secure; the remaining four are doubly secure within observational uncertainties. Severe blending is thus unlikely.

(iv) For some of the sources, the available data points straddle but do not directly constrain the region where the SED reaches a maximum (see Figure 5), so that our SED-derived luminosities could be over-estimated.

We are not in a position to account for all these uncertainties. However, for the cited sources in GOODS-N and for a few of the sources in LN reliable spectroscopic redshifts are available. Among four of these we were able, below, to search for potential lensing, assess a degree of blending, and justify our confidence in their derived luminosities in some detail. These sources are referred to by letters corresponding to their designations in Table 2.4. Note that in Table 2.4 we give bolometric luminosities whereas below we quote infrared luminosities.

The LN source (j) at equatorial position (J2000.0) 161.554052 / 58.788592, is

characterized in the Sloan Digital Sky Survey (SDSS) as a well-isolated circular source identified as a quasi-stellar object (QSO). The visible spectrum leaves no doubt about the redshift $z = 3.037$ determined by the strong Ly-α line. The visible continuum flux in this spectrum is $\sim 5 \times 10^{-17}$ erg cm^{-2} s^{-1} Å^{-1}, equivalent to $\sim 4 \times 10^{-5}$ Jy, stretching down to $\sim 1,000$ Å, for a total flux of roughly 1.2×10^{-16} W m^{-2}, approximately a factor of seven fainter than the infrared flux observed from the source. The IPAC extragalactic data base lists the optical source as brighter, by more than a magnitude, than any other source within a radius of an arc minute. Trouille et al. [2008] list a 0.5-2 keV X-ray flux of 38.4×10^{-18} W m^{-2}, and a 2-8keV flux of 22.4×10^{-18}W m^{-2} for the source, jointly about half the visible flux. Owen and Morrison [2008] detected a 20-cm continuum radio flux density of 64 μJy from this source, within an apparent size < 1.5 arcsec FWHM, ruling out obvious ambient emission that might have indicated lensing. The XID catalogs of Roseboom et al. [2010] show a relatively weak neighboring SPIRE source at a distance of 26 arcsec, and a source comparable in infrared brightness to LN 4241 but at a separation of ~ 34 arcsec. Because of their relatively large displacement, these and other ambient galaxies are unlikely to contribute appreciably to the SPIRE flux densities assigned to LN (j) by Roseboom et al. [2010]. All this gives confidence that both the visible and the infrared flux come from the same source, that there is no lens magnification, and that we are indeed dealing with an un-lensed ultraluminous source with infrared luminosity $\sim 1.8 \times 10^{13} L_{\odot}$. The simplest explanation for these data is that we are viewing a QSO with a surrounding hot torus along a sightline coinciding with outflowing gas. Dust heated by the QSO may contribute to the total infrared emission, but star formation likely contributes the bulk of it.

The GOODS-N source (c), with equatorial coordinates (J2000.0) 188.990097

/ 62.17342, is cited by Barger et al. [2008] as having spectroscopic redshift $z = 3.075$. The 24 μm flux density listed in the Barger catalog is 109 μJy. The rest-frame 2-8keV luminosity assigned to this source by Trouille et al. [2008] is 3.464×10^{36}W $\sim 9.01 \times 10^{9} L_{\odot}$, but their paper provides no rest-frame 0.5-2keV luminosity. The nearest SPIRE source listed in the XID catalogs lies at a distance of 35 arcsec, where its contribution to our primary galaxy's flux listed in the XID catalog can at most be minor. Our primary source also displays weak X-ray fluxes, but Morrison et al. [2010] list no 20-cm source within 3.5 arcmin. Integrating the flux densities indicated by the fitted SED in Figure 2.5, leads to an infrared luminosity of $6.0 \times 10^{12} L_{\odot}$.

One of our ultraluminous sources [LN (f)] has previously been discussed by Polletta et al. [2006]. They observed the Lockman SWIRE source at (J2000.0) 161.041521 / 58.87355 with Chandra and detected a flux of $2.7 \pm 1.1 \times 10^{-15}$ erg cm^{-2} s^{-1} in the 0.3 - 8 keV range. The Spitzer 24 μm flux is 4.0 mJy, strong for a source at spectroscopic redshift 2.54, and much brighter than anything within an arcminute of its location. Because of its initial detection by Spitzer, the authors characterize the source as an infrared selected Compton-thick AGN on the basis of the rest-frame hydrogen column density, which they estimate to be $N_H \sim 3 \times 10^{24}$ cm^{-2} with an uncertainty envelope extending a factor of three times lower and arbitrarily higher. The infrared luminosity derived on the basis of our SPIRE and PACS observations (see Figure 2.5 and Table 2.4) is $2.0 \times 10^{13} L_{\odot}$. It appears to be fairly well isolated in the infrared, the nearest comparably bright 250 micron source being located half an arcminute away.

Some of these ultraluminous galaxies could be lensed but a first look has not yet revealed these in our sample. The GOODS-N source (d), with coordi-

nates (J2000.0) 189.309509 / 62.20232, is cited by Barger et al. [2008] as having a spectroscopic redshift $z = 3.157$. Again, ambient nearby sources have relatively weak SPIRE fluxes unlikely to appreciably affect the SPIRE flux attributed to our source of primary interest. Another source only ~ 10 arcsec away is also noted in the NASA/IPAC Extragalactic Database (NED). This appears not to have a measured 24 μm flux and is not listed by Barger et al. [2008]. However, Law et al. [2007] have included this source in their discussion of distant irregular galaxies. The object designated as BX 150 appears elongated roughly along a north/south direction, is ~ 0.5 arcsec long with an aspect ratio roughly 2:1, and has a redshift $z = 2.28$. At optical wavelengths, it is 1.3 magnitudes fainter than the ultraluminous infrared source and, at its rather high displacement of ~ 10 arcsec, it is unlikely to provide significant lensing. With this proviso, the intrinsic infrared luminosity of GOODS (d) appears to be $\sim 1.1 \times 10^{13} L_{\odot}$.

Figure 2.5 provides the SEDs of these ultraluminous sources with their details noted in Table 2.4. Our combined surveys of GOODS-N and LN cover ~ 0.47 square degrees, or one part in 85,000 of the sky. Given that we observe several high-luminosity sources in the small area covered, it suggests that approximately 10^6 sources in the infrared luminosity range $\sim 10^{13} L_{\odot}$ should be observable in the Universe, at redshifts $z = 2.5$ to 3 at the current epoch. The number of comparably luminous sources observable at lower redshifts appears to sharply decline.

Our conclusions are robust even in view of three selection effects inherent in our data set:

(i) The first is that Figure 2.4, on which the conclusion is based, only includes sources detected at all three SPIRE wavelengths. For highly redshifted sources,

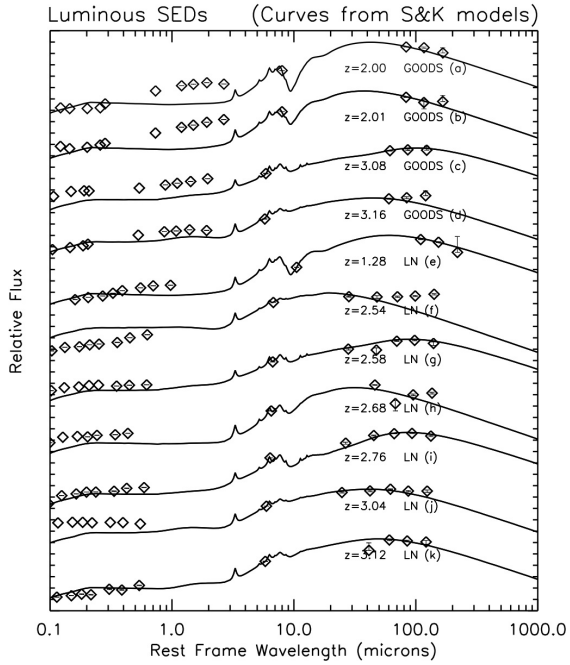

Figure 2.5 Spectral energy distributions of the most luminous sources in GOODS North (a) to (d) Lockman North (e) to (k). As in Figures 2.2 and 2.3, we solely plot the upper error bars at 500 μm for sources (a) to (e), whose lower error bars are compatible with zero. We similarly plot an upper error bar at 170 μm for LN (k). Luminosities and positions for these sources are presented in Table 2.4. Seven of these eleven sources are triply secure; two of these are also included in Figures 2.2 and 2.3. A brief description of sources (c), (d), (f) and (i) is provided in Section 2.6. Although some of the ultraluminous sources exhibit significant AGN activity, we have applied S&K model fits, as discussed in Section 2.7. As in Figures 2.2 and 2.3 we have weighted the 24 μm data only one quarter as heavily as the longer wavelengths. Observational data shortward of 24 μm is plotted for reference but not used in fitting.

the 100 μm infrared emission peak is redshifted into the 500 μm range, favoring the detection of galaxies at all three wavelengths, including 500 μm.

(ii) However, compensating for this effect, lower redshift sources are more readily detected by a factor inversely proportional to luminosity distance squared. Although these two effects partially cancel, high-luminosity sources should be more readily detected at low rather than high redshifts.

Table 2.4 Data on luminous galaxies whose SEDs appear in Figure 2.5, listed as in previous tables. The GOODS sources have spectroscopic redshifts, as do LN (f) and (j). The rest of the LN sources have photometric redshifts. The sources GOODS (a) and LN (i) correspond to the sources GOODS (L) and LN (I) shown in the previous figures and tables.

ID	RA	Dec	z	L_{bolo} ($L_\odot$)	SFR ($\frac{M_\odot}{yr}$)	M_{dust} ($M_\odot$)	Π_{250}	Π_{350}	Π_{500}	Radius (kpc)	A_v	Log(n)
GOODS (a)	189.0764	62.2640	2.0000	2.0×10^{13}	3400	6.0×10^{7}	0.82	0.71	0.33	1.0	119.0	2.0
GOODS (b)	189.1483	62.2400	2.0050	2.5×10^{13}	4200	3.6×10^{7}	0.69	0.24	0.38	1.0	71.0	2.0
GOODS (c)	188.9901	62.1734	3.0750	6.3×10^{12}	1000	2.0×10^{9}	1.61	1.22	0.84	15.0	18.0	4.0
GOODS (d)	189.3096	62.2024	3.1569	1.3×10^{13}	2000	4.0×10^{7}	0.57	0.55	0.84	3.0	9.0	2.0
LN (e)	161.7059	59.3247	1.28	1.3×10^{13}	2100	3.2×10^{8}	0.99	0.85	0.20	3.0	72.0	2.0
LN (f)	161.0415	58.8735	2.28	2.5×10^{13}	3400	4.1×10^{5}	0.98	1.10	1.71	0.3	6.7	2.0
LN (g)	161.5408	58.7950	2.58	1.3×10^{13}	2000	2.0×10^{9}	0.82	0.95	0.58	15.0	18.0	4.0
LN (h)	160.9635	58.9555	2.68	2.5×10^{13}	4300	8.8×10^{6}	0.18	0.95	0.96	0.3	144.0	2.0
LN (i)	161.8667	58.8704	2.76	2.5×10^{13}	4300	4.9×10^{9}	0.91	0.96	0.77	9.0	120.0	4.0
LN (j)	161.5541	58.7886	2.96	2.0×10^{13}	3100	4.0×10^{7}	0.76	0.61	0.60	3.0	9.0	3.0
LN (k)	161.8259	59.2771	3.12	1.3×10^{13}	2000	8.0×10^{7}	0.98	0.70	0.54	3.0	17.8	2.0

(iii) The XID catalogs search for SPIRE sources solely at locations where Spitzer 24 μm sources exhibit flux densities $\geq$ 20 μJy in the GOODS-N field and $\geq$ 50 μJy in LN. We may thus be missing sources at redshifts at which poorly emitting spectral regions are redshifted to 24μm. At redshifts $z \sim 1.4$, for example, the 9.7 μm silicate absorption dip shown by Spoon et al. [2007] to be prevalent in many ULIRGS is shifted to 24 μm. This may account for the striking absence of low-luminosity sources, at $z \sim 1.4$, i.e. the lack of sources hugging the luminosity distance curve at this redshift in Figure 2.4.

2.7 Discussion

Far-infrared surveys with Herschel need to take source confusion and source blending into account, particularly at the longest wavelengths, 350 and 500 μm. GOODS-N and LN are the two deepest surveys undertaken as part of the HerMES project as of September 2010. In these deep fields, crowding of sources

presents especially serious problems. In establishing a set of criteria that assess source blending, we have taken a preliminary step toward estimating the utility of the survey data for different purposes. This has proven itself useful in our analysis of the ultraluminous galaxies, some of which we described in Section 2.6 and whose characteristics are exhibited in Figure 2.5 and Table 2.4. In view of the high infrared luminosities we find, it is particularly satisfying that seven of the eleven sources cited turn out to be triply secure, i.e. with high purities in all three SPIRE wave-bands, and that five of the sources also are observed by PACS where blending is not severe, particularly in the 100 μm waveband. In this context, we have placed no upper limit on acceptable values of Π, which are especially high for GOODS(c) and LN(f), suggesting especially low ambient source contributions at their locations.

In compiling the SEDs for GOODS-N and LN, we have elected to work with the S&K models because they are based on a limited set of well-defined physical parameters. The models thus make predictions that our SEDs may be able to verify, refute, or extend. S&K do not specifically address the effects of adding an AGN component to a starburst model. However, they do provide a starburst fit for NGC 6240 and propose that addition of a small AGN component could provide an improved fit. Most starbursts generally also exhibit some AGN activity. Perhaps because of this, the S&K models appear to provide reasonable fits. The major weakness of the S&K models, as well as that of all others, tends to be the difficulty in accounting for the seemingly random relationship between the infrared and optical portions of the SEDs that is so apparent in Figures 2.2, 2.3, and 2.5.

We investigated the relationship between flux-density ratios at optical and

far-infrared wavelengths in high- and low-luminosity galaxies. Current theory suggests that starbursts involve stellar mass distributions obeying the Salpeter initial mass function [Zinnecker and Yorke, 2007].

The drop in luminosities from the most massive O type stars with mass $\sim 120 M_{\odot}$ to the early B type stars at 10 $M_{\odot}$, can then be shown to be roughly in a ratio of 500:1, i.e. with a contrast considerably higher than that of the mass ratio, roughly 12:1. The highest mass ranges will thus be depleted most rapidly, ending their lives in supernova explosions in which at least some of the dust will be destroyed or expelled from the galaxy. The most luminous galaxies found using our SEDs and their associated redshifts would thus be expected to be the very youngest as well as those most densely shrouded by dust, i.e. having the lowest fractional optical luminosities. To test this hypothesis we restricted ourselves to galaxies with total bolometric luminosities, $L > 10^{12} L_{\odot}$, as these have long been considered likely starburst mergers, albeit with potential contributions from AGNs [Sanders and Mirabel, 1996]. In Table 2.5, we compare the flux density ratios for the most and least luminous sources in three redshift bins. It is evident that larger ratios correspond to more luminous sources at all redshifts but that these differences greatly diminish at lower redshifts. This finding is both new and significant. It indicates evolutionary trends that may need to be incorporated into more advanced models of starbursts designed to yield SEDs which not only mirror observed ratios of optical to infrared emission, but also define a galaxy's place in its evolutionary history.

Figure 2.4 provides a capsule history of galaxy evolution over cosmological epochs for the sample included in our two deep surveys. The shapes of these distributions are nearly identical in LN and GOODS-N, which motivated us to

Table 2.5 Ratios ($R \equiv F_{FIR}/F_{optical}$) of SPIRE flux densities (consistently measured at 250 μm to minimize source blending) to optical flux densities at a rest wavelength ∼3000 Å, respectively measured at 4500 Å, 6100 Å, and 7600 Åfor successively larger redshifts. These three wavelengths were chosen to represent the visible spectra and avoid the Balmer jump at 3650 Å. For each redshift bin we compare the flux density ratio for the $N/2$ most luminous galaxies (R_{Bright}) to that of the $N/2$ least luminous galaxies (R_{Dim}) where N is the total number of $L > 10^{12} L_{\odot}$ sources.

z	N	R_{Bright}	R_{Dim}	R_{Bright}/R_{Dim}
$0.95 < z < 1.05$	18	64500	72000	0.90
$1.9 < z < 2.1$	18	62500	17600	3.6
$2.4 < z < 2.8$	10	62300	5920	11

plot both in the same figure. A glance confirms that sources having the highest luminosities are found at highest redshifts, i.e. earliest epochs. Luminosities higher than $10^{13} L_{\odot}$ are generally observed at redshifts $z \sim 2 - 3.2$, the highest redshifts reached in our surveys.

2.8 Conclusions

Confusion, which can be troubling at 250 μm, becomes increasingly severe at 350 and 500 μm. Yet the data at these longer wavelengths are particularly important given how important the longer wavelengths are for determining the total FIR luminosity. We believe that the triply-secure sources listed in Tables 2.2, 2.3, and 2.4 will be in demand for follow-on studies that X-ray astronomers, spectroscopists, and others may wish to undertake on sources known to be especially free of confusion.

With SPIRE photometry data in hand along with cross identifications at several shorter wavelengths, we have constructed SEDs for a handful of trustworthy sources in the GOODS-N and LN regions. Many of these can be fit by star-

burst SED models, such as those created by Siebenmorgen and Krügel [2007], which yield information on luminosity, dust mass, and size. Figures 2.2, 2.3, and 2.5 show a number of ultraluminous galaxies with $L_{IR} \sim 10^{13} L_{\odot}$. Although these are extreme systems, they do not appear to deviate from the general distribution at high redshift. A major strength of the deep HerMES surveys is their ability to obtain reliable source luminosities and star-formation rates based on flux densities in the infrared and at auxiliary wavelengths as well as redshifts compiled in the XID catalogues.

CHAPTER 3

GALAXY MASS, METALLICITY, RADIUS AND STAR FORMATION RATES

3.1 Introduction

The causes and conditions surrounding star formation are highly complex. The past few years, have witnessed many attempts to account for star formation laws, such as the Schmidt-Kennicutt law, or extensions of them [Madore, 2010, Shi et al., 2011]. Until recently, and even now, star formation rates have often been treated largely in terms of observable or inferred physical conditions within well-isolated galaxies [Calzetti and Kennicutt, 2009, Krumholz et al., 2012]. Within the past year or two, however, consideration of changing chemical abundances have begun to invoke infall and/or outflow of matter, some of which may have observable consequences on star formation only after considerable delay [Kobayashi et al., 2007, Brooks et al., 2007, Davé et al., 2011a].

Recently published observational evidence on correlations between star formation rates (SFRs) and gas metallicity as a function of galaxy stellar mass is certainly striking [Mannucci et al., 2010]. It suggests that star formation may need to be considered in entirely new ways that emphasize infall of matter from enveloping halos.

The Sloan Digital Sky Survey, SDSS, has made available star formation rates

*This chapter is an adapted version of the published article Brisbin et al. (2012).

and gas metallicities for more than a hundred thousand galaxies at red shifts $0.07 \lesssim z \lesssim 0.3$ [Tremonti et al., 2004, Gallazzi et al., 2005, Ellison et al., 2008, Kewley and Ellison, 2008, Mannucci et al., 2010, Peng et al., 2010, 2011, Aihara et al., 2011, Yates et al., 2012]. Although these data are largely statistical and may lack the more detailed correlations that observations on star formation in nearby galaxies make possible, the advantage of working with SDSS data is the ability to establish commonalities in the properties of tens of thousands of galaxies selected from a homogeneously acquired set. In particular, Ellison et al. [2008] noted a number of striking correlations between galaxy mass, radius, and metallicity, as well as between mass, star formation rate (SFR) or specific star formation rate (SSFR), and metallicity. This was complemented by a finding of Mannucci et al. [2010] who produced a three-dimensional Cartesian plot having galaxy mass, star formation rate, and metallicity as its orthogonal coordinates. This clearly shows the population of star-forming galaxies out to redshifts at least as high as $z \sim 0.3$ lying on a smoothly curved surface. The range of metallicities at each point on this surface is narrow, revealing the surface to be a thin curved sheet. Recent work by Yates et al. [2012] analyzes and confirms the findings of Mannucci et al. [2010] in greater detail.

The persuasive correlations these studies have revealed between high star formation rates and low metallicity, have made a compelling case for considering infall of pristine, low- or zero-metallicity gas as a primary factor governing massive star formation.

That infall of high-velocity clouds is prevalent at least in the Galaxy has recently been convincingly documented by Lehner and Howk [2011] through observations with the Hubble Space telescope. They identified the infalling gases

through their ionized oxygen, silicon and carbon absorption lines seen against stars at high Galactic latitudes, and estimated the rate of infalling mass to possibly be of the order of 0.5 $M_\odot$ yr^{-1}. This is potentially sufficient to maintain star formation at an expected rate for the Galaxy. Two questions, however, remain unanswered. The observed infall velocities are of order 100 km s^{-1}, which may be sufficiently low for the material to simply be gas that is falling back into the galaxy, having been previously ejected to some appreciable height. Further, the assumed metallicity of the infalling gas, estimated to be $Z \sim 0.2Z_\odot$, leaves unanswered the question of whether this could be the metallicity of infalling gas currently traversing the local halo, or again just reflect the metallicity of previously ejected material now falling back into the Galaxy.

These questions have been given impetus by the work of Davé et al. [2011a] and Davé et al. [2011b], who have emphasized the importance of supernova ejection of high-metallicity material, which then may fall back into a galaxy, depending on whether or not the ejection powers escape velocities.

Evidence for resolving these questions may soon accumulate through observations of outflows from star-bursting galaxies, as shown by recent observations on PG1206+459 by Tripp et al. [2011]. While uncertainties about the metallicity of the outflowing gas and the extent to which some of this gas may fall back into the observed galaxy still prevail, observations of the attempted kind may soon provide informative results.

Our motivation in pursuing the analyses provided in the present paper has been to unambiguously quantify the relationship between infall of gas and star formation rates. The data of Mannucci et al. [2010] strongly suggest that the correlation between SFR and low metallicity requires the infall of low-metallicity or

pristine extragalactic gas. But other explanations for this correlation, for example those of Cowie et al. [2011], have not be ruled out. In these circumstances, it appeared to us that the sheer wealth of data provided by the SDSS might serve as a guide, which would permit a more compelling analysis.

Obtaining an empirical relationship of the type we exhibit in the following sections, however, is not enough. Ideally one would like to have a physical model that accounts for an observed relation, is consistent with other observational data and, where possible with extant theory. For this purpose, we have developed a mean-field-theory toy model that indicates how the metallicity and velocity of infalling gas may be related to SFR and to the native gas content of a galaxy as discussed, for example, by Tremonti et al. [2004]; Dalcanton [2007]; or Peeples and Shankar [2011]. Such a model should also take into account recent calculations on infall of extragalactic gas into galaxy halos, to the extent that pristine or low-metallicity gases are most likely to have accumulated in a halo. Moreover, the velocity at which this matter traverses the halo and impacts on a galaxy should still reflect that history.

Although a toy model cannot be as comprehensive as dedicated computer simulations developed, e.g., by Brooks et al. [2007]; Kobayashi et al. [2007]; or Klypin et al. [2011], it provides ready insight on the physical relations between different parameters, and allows observers to check for potential confirmation or refutation of hypotheses on the basis of readily apparent scaling relations. Within these restrictions, the toy model we develop in the present paper appears at least in rough agreement with available data, and makes specific assertions that may be negated or verified by future observations.

A key feature of the present paper is a quantitative demonstration that

most, if not all star-forming galaxies with $M_* < 2.0 \times 10^{10} M_\odot$, and many with $M_* \geq 2.0 \times 10^{10} M_\odot$ and large radii appear to be fed by infall of pristine or low-metallicity gas. More massive galaxies, however, appear to form stars also by other means, possibly through consumption of gas injected into interstellar space by outflow from low-mass evolved stars, as suggested by Leitner and Kravtsov [2011]. The evidence we provide is chemical and based on a novel quantitative relationship we establish between SFR, metallicity and a galaxy's stellar mass.

The wealth of galaxies observed in the SDSS permits our toy model to examine not only the correlations between such properties as galaxy mass, radius, SFR, and metallicity, but, to a limited extent, also the evolution of these quantities with redshift. We restrict ourselves to galaxies observed in the redshift range $z = 0.07$ to 0.3, corresponding to an interval of about 2.5 Gyr spanning an epoch that began 3.4 and ended 0.9 Gyr ago. We assume standard flat ΛCDM cosmology, $\Omega_{CM} \sim 0.27,\ \Omega_{DE} \sim 0.73$, and a Hubble constant, $H_0 = 71$ km s^1 Mpc^{-1} [Wright, 2006].

We structure our paper as follows: Section 3.2 details our adopted data processing methods. Section 3.3 characterizes observational results. Section 3.4 introduces our main finding, namely that the relation between metallicity and SFRs in galaxies of fixed mass and radius is quantitatively consistent with dilution of native gas in these galaxies by infalling matter. Section 3.5 discusses our findings in terms of a mean-field-theory toy model that clarifies and quantitatively accounts for the observations. On the basis of the SDSS observations, section 3.6 derives mean values for the velocities $\langle V \rangle$ and densities $\langle \rho \rangle$ of infalling matter. In galactic halo models, these appear to be associated with mean

properties of clumps of gas traversing the halos. In Section 3.7, we briefly discuss the plausibly permitted range of differences between the mass infall rates that trigger star formation and the resulting star formation rates. A final section 3.8 discusses our findings in terms of other recently published studies.

3.2 Methods

Our selection of galaxies comes from the MPA-JHU catalog compiled from SDSS DR7 available online (http://www.mpa-garching.mpg.de/SDSS/DR7/).

To permit closer comparison of our data and those of Mannucci et al. [2010], we have used identical selections in redshift, (between z=0.07 and 0.3), Hα signal to noise ratio ($\geq$25), and we similarly excluded active galactic nuclei, AGNs, using the criteria put forward by Kauffmann et al. [2003a]. We have also followed identical procedures to find stellar mass, SFRs, and metallicities. Our stellar masses are taken directly from the MPA-JHU catalog as inspired by Kauffmann et al. [2003b], with a correction to convert from masses based on a Kroupa IMF [Kroupa, 2001] to a Chabrier IMF [Chabrier, 2003]. Star formation rates are determined using Hα and are based on the work of Kennicutt [1998a] with a correction for a Chabrier IMF.

While Hα is subject to foreground dust extinction, we correct for this using the Balmer decrement, along the same lines as Cardelli et al. [1989]. We excluded any sources with large extinction corrections corresponding to $A_V > 2.5$. Metallicities are determined from the strong line diagnostics $R_{23} = ([OII]3727 + [OIII]4958 + [OIII]5007)/H\beta$ and $[NII]6584/H\alpha$ as presented in Nagao et al. [2006] and Maiolino et al. [2008]. We note that other alternatives for obtaining

metallicities have recently been proposed by Lara-López et al. [2010]; but for ease of comparison we have opted to follow procedures adopted by Mannucci et al. [2010] and Ellison et al. [2008].

The bulk of our selected sources cover a galactic stellar mass range from $\sim 10^9$ to $2 \times 10^{11} M_\odot$, with star-formation rates ranging roughly from 0.035 to $6.4 M_\odot$ yr^{-1}, and oxygen abundances from $\sim 4 \times 10^{-4}$ to 1.4×10^{-3}, straddling a Solar System abundance of $\sim 8.5 \times 10^{-4}$. Because we concentrate on the additive properties of metallicity, rather than metallicity ratios, we express metallicities throughout in terms of actual oxygen abundances, as opposed to their logarithmic values more conventionally adopted.

The redshift range covered both by Mannucci et al. [2010] and us is set at a minimum value of $z = 0.07$ to ensure that the [OII]$\lambda 3727$ emission line is well within the useful spectral range and that the 3" aperture of the SDSS spectroscopic fiber will sample a significant fraction of a galaxy's surface area. At $z = 0.07$, an aperture of 3" corresponds to an angular diameter of 4 kpc implying that we probe only the central 2 kpc regions of a galaxy. At $z = 0.3$, our observations probe galaxies out to radial distances ~ 6.6 kpc, and thus sample the galaxies more fully [Wright, 2006].

In addition to these selection criteria imposed by Mannucci et al. [2010] and ourselves, we required our sample to have an observed Petrosian half-light radius in the r-color band, r_{50}. This is required, in the spirit of Ellison et al. [2008], to investigate the role galactic radius plays in star formation and metallicity. We have also taken pains to eliminate duplicate observations from our SDSS sample. Where an object was observed multiple times, we averaged its properties across the multiple entries.

Both Mannucci et al. [2010] and Ellison et al. [2008] treated galaxies in the redshift range we cover as though they were coeval. To examine whether or not further insight could be gained through study of the provenance of their galaxies, we have divided the SDSS galaxies into individual tables corresponding to three separate redshift ranges, $0.07 \leq z \leq 0.10,\ 0.10 \leq z \leq 0.15,\ \text{and}\ 0.15 \leq z \leq 0.30$; and three Petrosian half-light radii r_{50} ranges, small $r_{50} < 3.74$ kpc, medium $3.74 \leq r_{50} < 5.01$, or large $r_{50} \geq 5.01$. Each table divides galaxies according to logarithmic mass and logarithmic SFR. These tables all are available as part of our paper online.

Although many of the entries in our tables show galaxy populations that may be quite sparse in certain galaxy mass/SFR bins, we considered our findings significant only if based solely on bins that have ≥ 50 galaxies per bin.

We are aware that Chabrier [2005] has updated his initial mass function and that it is in better agreement with current data as indicated by Parravano et al. [2011]. However, in order to compare our observational data and analytic model with those of Mannucci et al. [2010] and Ellison et al. [2008], in section 3.6 below, we have chosen to adopt an initial mass function identical to theirs in order to maintain our respective data sets as homogeneous as possible, so that a more direct comparison of our findings and theirs may emerge. This procedure admittedly maintains inherent biases that all three data sets may propagate, but enables a more meaningful comparison of results.

While the SDSS provides a way of studying star formation statistically in a sample exceeding a hundred thousand galaxies, both our selection and those of Mannucci et al. [2010] and Ellison et al. [2008] restrict themselves to observations of the central portions of galaxies, in many of which spiral arms no longer

are well defined. Our sample thus is not adequate to addressing questions of spiral structure or its effects on star formation, and generally obstructs direct comparison to work studying star formation over larger portions of galaxies' disks. Nevertheless, given the importance of processes taking place in the nuclear portions of galaxies, our choice of regions has a compelling interest of its own.

3.3 The Observed Galaxy Sample

In Figure 3.1 we present our galaxy sample for the entire redshift and radial size range divided into logarithmic SFR and stellar mass bins. In each bin where $>$50 sources exist the metallicity is plotted on the vertical axis.

A full complement of nine sets of tabulations showing galaxy stellar mass, SFR, gas metallicity and metallicity scatter, separately for each of the three redshift intervals and each of the three ranges of Petrosian radii, is provided online. As an example, one of these table sets is given in Appendix A. The tables provide much of the statistical information of interest to our paper derivable from the SDSS.

To detect whether evolutionary effects might have had an impact on previously published findings we divided the available data into the three redshift ranges defined above. In mass/SFR bins where there were sufficient data in all three redshift epochs our tables provide data on the evolution of metallicity with time. There are ~ 40 overlapping mass/(SFR) bins in the three red-shift tables, in which each bin is populated by at least 50 galaxies. In all, this comprises several thousand galaxies in each redshift range. Strikingly, galaxies with iden-

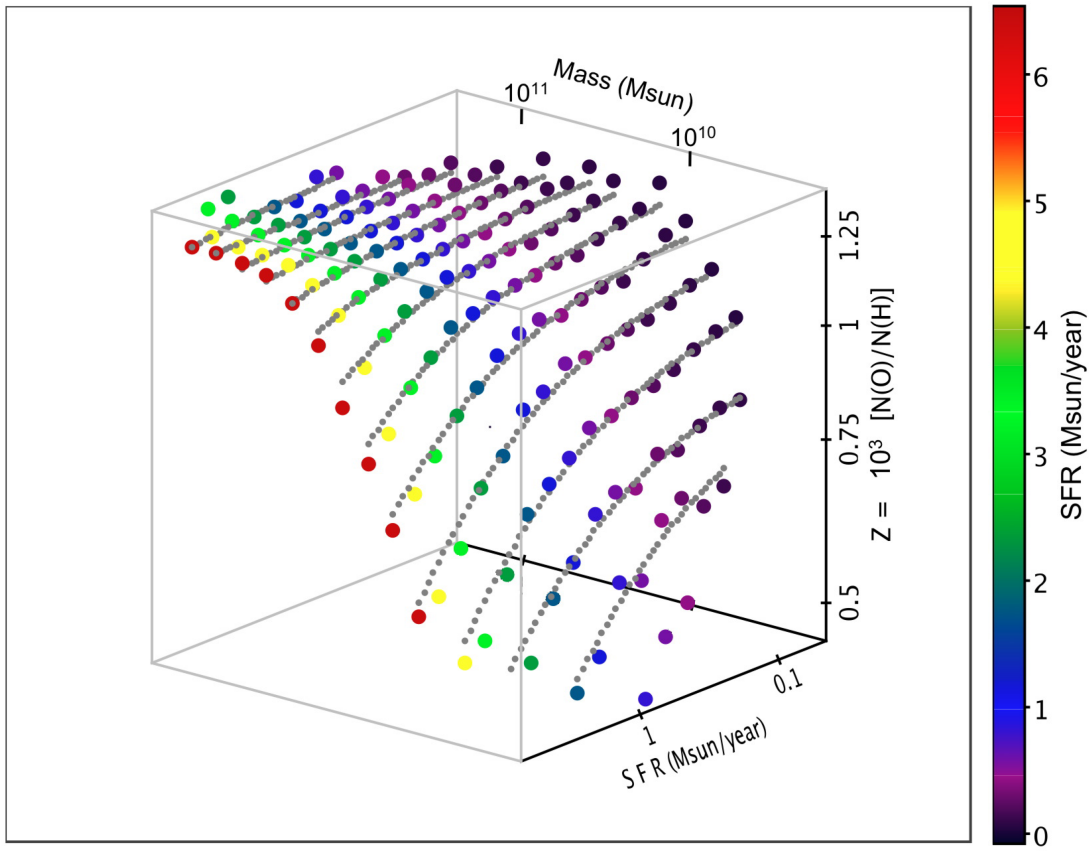

Figure 3.1 Median metallicity for samples across our range of mass and SFR. This includes samples across all redshift cuts and all radius cuts. Here we include only samples with at least 50 sources at a given mass and SFR. The small grey points indicate toy model fits to our data, as detailed in section 3.5. Complete numerical tables of these data as well as subsets in redshift and galactic radius are available online.

tical mass and SFR bins have median metallicities that vary across redshift by at most a few percent, somewhat randomly and well within standard deviations that generally are of order 15%. This is in satisfactory accord with the findings of Savaglio et al. [2005], who observed galaxies in the somewhat higher redshift range, $0.4 \lesssim z \lesssim 1.0$ and found no significant evolutionary trends in the galaxy mass-metallicity relation.

Evidently, galaxies with identical masses and star formation rates, in the

Table 3.1 Main Sequence Galaxies: Peak Populations in the Mass/SFR Tables

Redshift Coverage of Table	$0.3 \geq z \geq 0.15$	$0.15 \geq z \geq 0.10$	$0.10 \geq z \geq 0.07$
Metallicity Range Spanning all Masses (N(O)/N(H) $\times 10^3$)	0.61 - 1.37	0.51 - 1.39	0.473 - 1.34
Galaxy Mass, M_*, in Peak Population Bin in units of $10^{10} M_\odot$	5.62	2.82	1.41
Metallicity in Peak Population Bin (N(O)/N(H) $\times 10^3$)	1.26	1.23	1.17
SFR in Peak Population Bin (in units of $M_\odot$ yr^{-1})	2.239	1.122	0.398
$\tau_d \equiv M_*$/SFR at Peak Population (in units of 10^{10} yr)	2.5	2.5	3.5

mass range from $\sim\ 7 \times 10^9$ to $\sim\ 10^{11} M_\odot$, appear to also share other significant properties despite the $\sim\ 2.5$ Gyr epoch spanning the redshift range $0.07 \leq z \leq 0.30$. In this respect, the metallicities exhibited in the single table that Mannucci et al. [2010] provided appear to be robust even though they included data on galaxies over the entire $z = 0.07 - 0.30$ redshift range and thus galaxies observed at epochs that may differ by as much as 2.5 Gyr within individual bins.

We find that even at the highest SFRs, the galaxies in our sample could not have gained sufficient mass during the ~ 2.5 Gyr between epochs $z = 0.3$ and 0.07 to shift significant numbers of galaxies from one mass column into a neighboring column. As table 1 indicates, SFRs diminish toward lower galaxy mass but in such a way as to apparently enable all of the galaxies to accumulate mass at a rate proportional to their own masses. In effect, the specific star formation rate (SSFR), defined as the star formation rate per galaxy mass, remains constant for this peak population component. Peng et al. [2010] have also noted that the deviation from constancy of the SSFR is quite small across all masses in the SDSS. Here we are finding a related result, namely that their relation

holds even though a significant number of higher-mass galaxies are observed at an epoch 2.5 Gyr earlier than virtually all low-mass galaxies. The time τ_d galaxies at all masses would require to double their mass at their observed SFRs is practically constant. τ_d is the reciprocal of SSFR, and assumes values of $\tau_d \sim 2.5 - 3.5 \times 10^{10}$ yr, roughly 2 times the age of the Universe at each of the observed epochs [Wright, 2006].

These data should, however, not be interpreted as indicating low, steady infall rates that maintain a galaxy in a relatively stable state of mass accretion. We envisage an individual galaxy of given mass periodically moving down or up within its mass column in one of our tables, as infall from its surrounding halo increases or decreases both the infall and the star formation rate within the galaxy. As we begin to show, starting with the next section, mass infall rates into galaxies vary across a range spanning nearly two orders of magnitude, need not be constant in time, and appear to be consistent with episodic star formation in the SDSS sample we have studied.

3.4 Infall and Metallicity Dilution of Native Gas

We now examine the extent to which the amount of mass $\dot{M}_i \tau_i$, which has fallen into a galaxy before onset of star formation, dilutes the initial metallicity Z_0 of the mass of native gas, M_g, present before the onset of star formation.

If we assume that the infalling matter has metallicity Z_i, and mixes thoroughly with the galaxy's native gas, we expect that the observed metallicity Z_x should be given by the ratio of the aggregated mass in metals after infall,

divided by the total aggregated gas.

$$Z_x = \frac{(\dot{M}_i \tau Z_i + M_g Z_0)}{(\dot{M}_i \tau + M_g)} \tag{3.1}$$

From equation (3.1) we can see that in galaxies which have an amount of infalling gas equal to the native gas mass, $\dot{M}_i \tau = M_g$, the observed metallicity will be half the native metallicity, $Z_x = \frac{1}{2} Z_0$, if the infalling gas has zero metallicity, $Z_i = 0$.

To test equation (3.1) broadly, we adopt a trial function expressing mass infall rates, $\dot{M}_i$, for which we lack observations, in terms of SFRs for which we do have observations,

$$\dot{M}_i = \alpha (SFR)^{2/3}, \text{ equivalent to } (SFR) = \epsilon \dot{M}_i^{3/2} \, . \tag{3.2}$$

Here α and $\epsilon \equiv \alpha^{-3/2}$ are constants of proportionality having some as-yet-unknown value but units, respectively of $M_\odot^{1/3}$ yr$^{-1/3}$ and $M_\odot^{-1/2}$ yr$^{1/2}$.

We will justify the $\dot{M}_i$ - SFR relations of equation (3.2) in section 3.5. The second of these relationships is the more physical. The factor ϵ is a measure of star formation efficiency. But, for now, we will make use of the relationship based on α, because (SFR) is an observationally determined quantity, whereas $\dot{M}_i$ is derived. Using this relation the observed gas metallicity takes the form

$$Z_x = \frac{Z_0 \left[1 + \frac{Z_i}{Z_0} \left(\frac{\alpha (SFR)^{2/3} \tau_i}{M_g} \right) \right]}{\left(1 + \frac{\alpha (SFR)^{2/3} \tau_i}{M_g} \right)} \, . \tag{3.3}$$

Table 3.2 Star Formation Rates and Observed and Computed Metallicities for low redshift, small half light radius galaxies with $M_* = 0.5 \times 10^{10} M_\odot$ in Figure 3.2.

(SFR) $M_\odot$/yr	$(SFR)^{2/3}$	$10^3 \times Z_x$ Observed N(O)/N(H)	$10^3 \times Z_x$ Modeled (Eq 3.3)
0.10	0.22	1.00	0.99
0.14	0.27	0.97	0.97
0.20	0.34	0.94	0.95
0.29	0.43	0.90	0.92
0.40	0.55	0.88	0.89
0.57	0.69	0.86	0.86
0.81	0.87	0.82	0.82
1.14	1.09	0.79	0.77
1.61	1.37	0.72	0.72

As an example, we may use the entries for low redshift ($0.07 \leq z \leq 0.10$,) medium radius ($3.74 \leq r_{50} \leq 5.01$ kpc,) galaxies of mass $0.5 \times 10^{10} M_\odot$ from our tables. Adopting the observed metallicities in units of oxygen abundances ($10^3 \times$N(O)/N(H)), at the available SFRs ($M_\odot$ yr^{-1}), we can calculate best fit values of Z_0 and $(\tau_i \alpha)/M_g$. For these data we find a good fit with $Z_0 = 1.06 \times 10^{-3}$ N(O)/N(H) and $(\tau_i \alpha)/M_g = 0.414$ ($M_\odot$/year)$^{-2/3}$. Table 3.2 shows the results of this sample calculation and Figure 3.2 shows equation (3.3) fitted to the sample data. Regrettably, we cannot isolate M_g from $\alpha \tau_i$ with the data given, and can derive solely their ratio $(\alpha \tau_i)/M_g$.

Online we provide our metallicity fits like those of Figure 3.2 for all stellar masses, radii, and redshifts for which we have adequate statistics — by which we mean > 50 galaxies per mass/SFR bin and 5 of such bins per galaxy mass column. For each sample of galaxies we performed a χ^2 analysis, testing equation (3.2) with a range of $0.1 \leq Z_0 \times 10^3 \leq 1.5$ N(O)/N(H) and $0 \leq \frac{\alpha \tau_i}{M_g} \leq 5$ ($M_\odot$/year)$^{-2/3}$ and selecting the lowest reduced χ^2 fit. Observational uncertain-

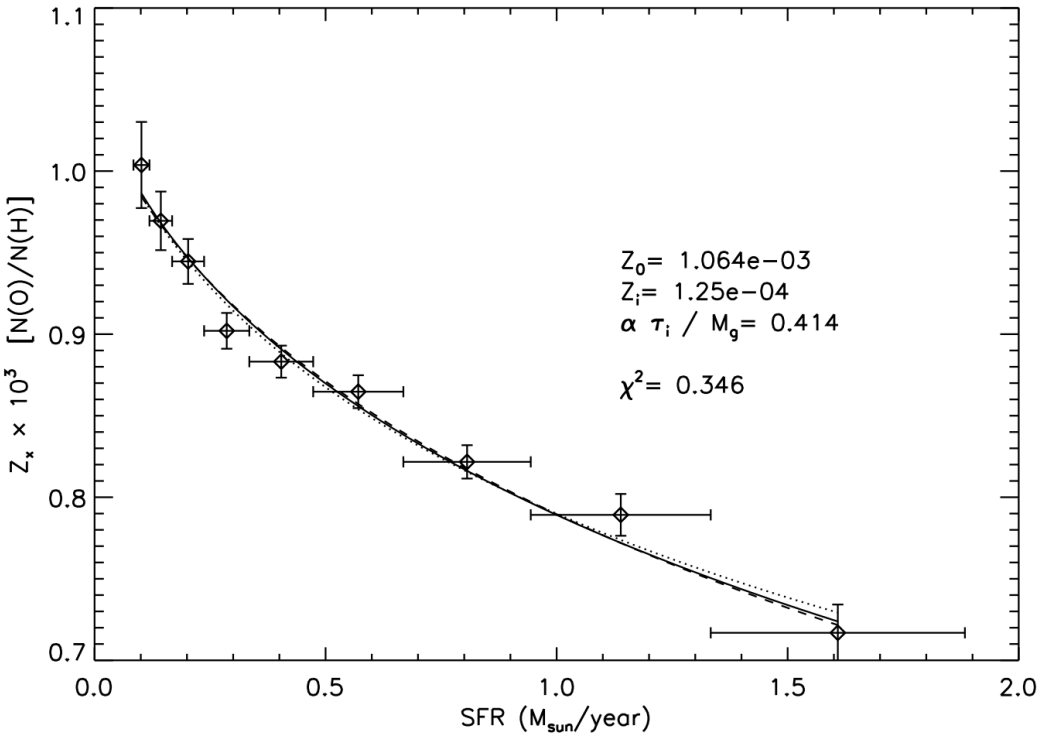

Figure 3.2 Observed gas metallicities at various SFRs for $M_* = 0.5 \times 10^{10} M_\odot$ galaxies with low redshifts and small half light radii. The fitted equation (3.3) with $Z_0 = 1.064 \times 10^{-3} N(O)/N(H)$, $(\tau_i \alpha)/M_g = 0.414$ ($M_\odot$/year)$^{-2/3}$, and $Z_i = 0.125 \times 10^{-3}$ is plotted as a solid line. The fit is acceptable with a χ^2 value of 0.35. Dashed and dotted lines indicate fits based on our lower and rough upper limits on Z_i, 0 and 0.25×10^{-3} respectively. Similar plots for galaxies with different stellar masses, radii and redshifts are available online.

ties in the emission lines used in our strong line diagnostics are propagated through to find the uncertainty in metallicity for each mass bin. Horizontal error bars represent the uncertainty in SFR due to the SFR bin width. To make use of the SFR uncertainties in our χ^2 analysis we found how much the model metallicity varies over the range of each SFR bin and took half this variance to add in quadrature with the metallicity uncertainty. This conversion of uncertainty in SFR to uncertainty in metallicity is performed for each SFR bin in each galaxy sample with every trial of model parameters.

While we expect Z_0 and $\frac{\alpha\tau_i}{M_g}$ to vary between galaxies of different mass, in our naive picture the infalling gas should not anticipate what kind of galaxy it is falling into and thus should not vary systematically between mass bins. As Davé et al. [2011a] and Davé et al. [2011b] have pointed out, however, feedback in the form of supernova ejection may pollute extragalactic gas, raising the possibility that infalling gas might already have significant metallicity. For that reason, in our χ^2 analysis we allow the infalling gas metallicity, Z_i, to be nonzero but fix it at the same value for each sample. Repeating the whole fitting procedure many times with different fixed values of Z_i we find that a value of $Z_i = 0.125 \times 10^{-3}$ minimizes the total χ^2 of our combined fits. A range of low metallicity solutions, spanning $0 \leq Z_i \leq 0.20 \times 10^{-3}$ provide nearly equally good fits, while for $Z_i \geq 0.30 \times 10^{-3}$ the fits become clearly worse and the total χ^2 value sharply increases. We therefore take 0.125×10^{-3} as our infalling gas metallicity with the caveat that our results are consistent with any very low metallicity infalling gas $Z_i \sim 0.125 \times 10^{-3} \pm 0.125 \times 10^{-3}$.

Our metallicity fits show that 72% of the SDSS galaxy samples obey the metallicity / star-formation relations and are well fit by equation (3.3). Given our small number of degrees of freedom (which ranges between 3 and 13) for each of our metal dilution samples, we used a reduced χ^2 value of 2 for our cutoff.

For the curves that provide good fits, we averaged both the Z_0 and M_g values obtained for each group of galaxies with a given stellar mass M_*. For the mass sequence from $M_* = 0.36$ to $11.2 \times 10^{10} M_\odot$ for which we have sufficient data, we find a monotonic increase in metallicity going from Z_0 = 0.90 to 1.37×10^{-3} N(O)/N(H). We normalize the other fitting parameter by multiplying it by stel-

lar mass, $\alpha\tau_i M_*/M_g$. This parameter stays relatively constant over the entire galaxy mass range, hovering around an average value of (2.3 $\pm$ 0.7) $\times 10^9$ (yr^2 M$_\odot$)$^{1/3}$. On the assumption that α and τ_i are constants across our sample bins, this parameter is indicative of the stellar to gas mass ratio. If the gas fraction in a typical galaxy were $M_g/M_* \sim x$, the corresponding fitted parameter would be $\alpha\tau_i \sim 2.3 \times 10^9 x$ (yr^2 M$_\odot$)$^{1/3}$.

Sets of galaxies not obeying equations (3.1) and (3.3), invariably exhibit high metallicities at high SFRs and masses $M_* \geq 2.0 \times 10^{10} M_\odot$, suggesting that for these galaxies star formation independent of pristine or low-metallicity mass infall plays a significant role.

The good quality of the fits we observe convince us that the dilution we have modeled actually takes place. Particularly interesting then is that the anticipated dilution must take place before star formation is initiated, so that the observed HII regions, which enable us to determine SFRs and metallicity values, reflect the conditions that triggered the formation of the stars.

Two points may still be noted. Tremonti et al. [2004], Dalcanton [2007], and Peeples and Shankar [2011] have evaluated a number of trends of gas mass and metallicity in galaxies with different stellar masses. However, as the detailed atlas of galaxies compiled by Leroy et al. [2008] makes clear, global ratios of gas-to-stellar mass vary enormously, depending on whether one is dealing with a narrowly defined central region of a galaxy, as defined by the SDSS spectroscopic aperture used throughout the present paper, or entire galaxies, as studied by Leroy et al. [2008]. Extended galaxies generally show the ratio of gas to stellar mass in a galaxy's central regions to be of the order of a few percent, even when that ratio, averaged over the entire galaxy is one or two magnitudes higher. But

even in these central regions, the ratio M_g/M_* can vary greatly.

For this reason, legitimate questions may be raised about our assumption that some well-defined metallicity and fractional amount of native gas can be defined for galaxies in a given stellar mass range, and that both parameters may be expected to vary systematically and continuously over galaxies having different stellar masses. In particular, one may ask what physical basis might account for such a relationship.

The response to these questions is that, in the present investigation, both the gas fractions and the metallicities involved are statistically determined. For each of the galaxy masses and SFRs considered we deal with groups no smaller than 50 galaxies. For galaxies in each stellar mass range, both the derived native gas metallicity and an assumed gas fraction derived from all the distinct SFR ranges are averaged over hundreds if not thousands of galaxies. To the extent that the SDSS galaxies fall into different classes, governed by distinct physical conditions, there may be no single physical reason for assuming that such average values actually exist, other than that the occurrence of each class of galaxy in the general distribution of galaxies follows some well-defined evolutionary history, and that the physical parameters governing these galaxies' gaseous components fall into a relatively restricted range.

Table 3.3 provides additional insight offered by an analysis of galaxies of different radii. In this table we show the fitted native gas metallicity values, Z_0, at all masses and radii where adequate statistics were available in a mass range spanning 0.25 - 4 $\times 10^{10}$ $M_\odot$. Note that satisfactory fits using equation (3.3) were found for all three radii, at low and medium redshifts at galaxy masses $0.7 \leq M_*/(10^{10}\ M_\odot) \leq 1.4$ and $1.0 \leq M_*/(10^{10}\ M_\odot) \leq 2.8$, respectively. Below this

Table 3.3 Native Gas Metallicities ($Z_0 \times 10^3$) as a Function of Stellar Mass and Galaxy Radius. (For details see text.)

M_*	$0.10 \geq z \geq 0.07$			$0.15 \geq z \geq 0.10$			$0.3 \geq z \geq 0.15$	
($10^{10}M_\odot$)	r_{50}: Small	Med.	Large	Small	Med.	Large	Med.	Large
0.36	0.90							
0.50	1.06	1.06		1.36				
0.71	1.18	1.13	1.06	1.32				
1.00	1.25	1.17	1.18	1.30	1.20	1.14		
1.41	1.30	1.24	1.24	1.39	1.28	1.22		
2.00				1.39	1.33	1.24		
2.82				1.37	1.33	1.30		1.30
3.98			1.31	1.35	1.34		1.41	1.29
5.62			1.27	1.34			1.31	1.31
7.94					1.37	1.30	1.36	1.31
11.2								1.37

range there were not enough data for a significant fit; above this mass range, at the radii indicated, the data were not well fitted by equation (3.3) and are indicated by blanks in Table 4. All the galaxy bins displayed show a trend of increasing metallicity with mass and generally decreasing metallicity with radial size.

The significance of the parameter α remains to be determined. This becomes apparent if equation (3.2) is recast in the equivalent form $(SFR) = \epsilon \dot{M}_i^{3/2}$, where ϵ is a constant whose units are $(M_\odot/yr)^{-1/2}$and $\alpha = \epsilon^{-2/3}$. Seen in this form, ϵ is readily interpreted as a factor determining star formation efficiency and inversely proportional to the cube root of the mass infall rate. In section 3.5, immediately below, we will show how this efficiency relates to pressure regulated star formation in triggered molecular cloud collapse.

Before leaving this section, we should still address the question of mass balance. Gas falling into a galaxy should either add to the galaxy's gaseous or

stellar mass, or add mass to a central black hole, unless an equal amount of mass is ejected from the galaxy explosively or by means of a variety of potential winds. Equation (3.2) thus should not be interpreted as meaning that the duration of infall is identical to the duration of star formation. As discussed in the next several sections, we deduce that the two processes are sequential, and that their respective durations are generally not identical.

3.5 A Mean-Field-Theory Toy Model

To account for the findings reported thus far within the larger framework of astrophysics, we next adopt a toy model based on a mean-field-theoretic approach.

Consider a distant, highly tenuous, cold clump of gas of mean mass density $\langle\rho\rangle$ indirectly approaching a galaxy of mass M. Let the relative velocity of the clump at large separations be V. This clump may have been previously captured into a massive halo surrounding the galaxy. We may follow the motion of a volume element of the clump displaced by an impact parameter s from the point on the clump that will eventually impact on the galaxy's center. At large distances from the galaxy, the angular momentum of a unit-mass increment of gas about the galaxy's center is sV. Because gas pressures within a cold tenuous clump may be largely neglected, angular momentum conservation tells us that the velocity v of the mass increment impacting on the galaxy at radius r is given by

$$Vs = vr \ , \tag{3.4}$$

and the infall energy of the increment is

$$\frac{v^2}{2} = \frac{V^2}{2} + \frac{MG}{r} \, . \tag{3.5}$$

Here G is the gravitational constant and, as usual, the two equations deal solely with the dominant azimuthal velocity components while neglecting minor helical velocity twists.

Within some radial distance r_m from the galaxy's center, infalling matter will be captured through collision with native gas gravitationally anchored to the galaxy. Beyond r_m the galaxy's gaseous component may be too tenuous and/or M may be too low, and capture will cease. Solving the two equations for s and V we obtain a capture cross section for matter falling into the galaxy within radius r_m.

$$\pi s^2 = \pi \left[r_m^2 + \frac{2 r_m MG}{V^2} \right] \, . \tag{3.6}$$

Within a radial distance r_m from a galaxy's center, the mean infall rate depends on the mean intergalactic gas density $\langle \rho \rangle$ as

$$\langle \dot{M}_i \rangle = \pi \langle \rho \rangle s^2 V = \pi \langle \rho \rangle \left[r_m^2 + \frac{2 r_m MG}{V^2} \right] V \, . \tag{3.7}$$

Every indication given by the low metallicity of SDSS star-forming galaxies is that star formation at least in these galaxies is initiated by infall of low-metallicity gas. Triggered star formation is generally thought to commence when the pressure on a molecular cloud is sufficiently high [Krumholz et al., 2009]. The pressure P exerted on the galaxy due to infalling gas will vary as a

function of radial distance r, and will also depend on infall angle, i.e., whether impact of the infalling gas is at a glancing angle or perpendicular to the gas layer it impacts. But because our data provide only a single star formation rate per galaxy, the parameter of immediate relevance may be some representative pressure $\langle P \rangle$ suitably averaged over radial distances r and angles of incidence θ. Taking v now to be the infall velocity at radial distance r, and $v\langle f(\theta)g(r)\rangle$ a representative perpendicular-impact-velocity component averaged over all radial distances r and directions θ, we can write the pressure for infall onto an area A within radial distance r_m from a galaxy's center as

$$\langle P \rangle \sim \frac{\dot{M}_i v \langle f(\theta)g(r)\rangle}{A} = \langle \rho \rangle \frac{\pi r_m^2}{A} \left[1 + \frac{2MG}{r_m V^2}\right]^{3/2} V^2 \langle f(\theta)g(r)\rangle$$
$$\sim \frac{\dot{M}_i^{3/2} V^{1/2}}{A r_m (\pi \langle \rho \rangle)^{1/2}} \langle f(\theta)g(r)\rangle \ , \quad (3.8)$$

where we have made use of equations (3.4), (3.5) and (3.6) to eliminate v.

An important feature of equation (3.8) is that $\langle P \rangle$ is solely a function of the infall rate $\dot{M}_i$, galaxy mass M, and radius r_m, as well as two universal parameters characterizing the infalling matter, a representative velocity for clumps traversing the halo, V, and a representative clump mass density, $\langle \rho \rangle$. Although we have not yet derived estimates for V and $\langle \rho \rangle$ on the basis of available data, we will do so in section 3.6, below.

Massive star formation is known to occur principally, if not solely, in giant molecular clouds. Two recent findings regarding these clouds now enter consideration:

Krumholz et al. [2012] have shown convincingly that star formation rates are

directly proportional $\rho_{c\ell}^{3/2}$,where $\rho_{c\ell}$ is the molecular cloud density, in the Galaxy, local disk galaxies and star bursts, and high redshift disks and starbursts. The universality of this relationship is documented by their Figure 3, which establishes a single observationally derived ratio of SFR-per-unit-area $\dot{\Sigma}_*$ to areal-density-divided-by-free-fall-time, Σ/t_{ff}. Within factors of order ± 3, this ratio remains constant at $\dot{\Sigma}_* \sim 10^{-2}\Sigma/t_{ff}$ over a SFR density range of six orders of magnitude. Here, Σ is the areal density, $t_{ff} = \sqrt{3\pi/32G\rho_{c\ell}^3}$, and G is the gravitational constant. Two relevant factors to take away from this is that, both on dynamic and observational grounds, $(SFR) \propto \rho_{c\ell}^{3/2}$, and that the observed star forming efficiency is of order 1%.

A second consideration is that calculations originally by Glassgold and Langer [1973] and Goldsmith and Langer [1978] and extended by Juvela and Ysard [2011] show theoretical considerations imply that molecular cloud core temperatures should be remarkably constant. Equilibrium temperatures, at which cosmic ray heating is balanced by spectral line cooling and cooling by dust to which the gas is coupled, are expected to cluster around $T \sim 10$ K for clouds in the density range $n(H_2) = 3 \times 10^2$ to 10^5 cm^{-3}. These considerations are in general accord with early temperature measurements by Solomon et al. [1987]. Gas clouds evidently undergo rapid cooling down to temperatures of order 10K, below which the cooling becomes less efficient. The temperature constancy across such a wide density range suggests that, over sufficiently long periods to permit heat to be radiated away, molecular clouds thus may be isothermally compressed through application of an external pressure.

We now examine whether gas falling into a galaxy can produce the required pressure to significantly increase the density of a molecular cloud. Using a virial

coefficient defined as $\alpha_{vir} \equiv 5\sigma_{tot}^2 R/M_g G$, where R is the molecular cloud radius, M_g is its mass, and σ_{tot} is the one-dimensional thermal plus turbulent velocity dispersion within the cloud. Krumholz et al. [2009] give the mean pressure in a cloud as $P_{c\ell} = 0.7 \times 10^5 \alpha_{vir} \Sigma_{c\ell}^{'\,2}\ k_B$ dyn cm^{-2}. Here $\Sigma'_{c\ell}$ is the areal density of a cloud in units of $\Sigma_{c\ell} \sim 85 M_\odot$ pc^{-2} $\sim 2 \times 10^{-2}$ g cm^2, k_B is the Boltzmann constant, and $\alpha_{vir} \sim 2$ independent of galaxy environment, as found by Bolatto et al. [2008] and revised by Krumholz et al. [2009]. A value of $\alpha_{vir} = 1$ implies that the cloud is in self-gravitating virial equilibrium, so that the internal turbulent plus thermal pressures approximately balance gravity. When $\alpha_{vir} \ll 1$, a cloud undergoes free-fall collapse unless magnetic fields support it.

To exceed a cloud virial coefficient $\alpha_{vir} \sim 1$ an external pressure needs to typically exceed $P \sim 10^{-11}$ dyn cm^{-2}. We can use equation (3.8) to determine the conditions under which pressures of this magnitude may be expected. Setting the factor $\langle f(\theta) g(r) \rangle \sim 1$, we then obtain

$$P = 10^{-11} \left(\frac{\dot{M}_i}{0.5 M_\odot/\mathrm{yr}} \right)^{3/2} \left(\frac{V}{170\ \mathrm{km/s}} \right)^{1/2} \left(\frac{13\ \mathrm{kpc}^2}{A} \right) \times \left(\frac{3.3\ \mathrm{kpc}}{r_m} \right) \left(\frac{5 \times 10^{-28}\ \mathrm{g/cm}^3}{\rho} \right)^{1/2} \mathrm{dyne/cm}^2\ , \quad (3.9)$$

where we have anticipated physical parameters we will justify in section 3.6 below. The point to recognize, however, is that an infall rate of $\sim 0.5 M_\odot$ per year converging on a galactic area smaller than ~ 13 kpc^2 will generate a sufficiently high pressure to compress typical galactic clouds and thus trigger star formation.

The triggering process no doubt is complex. Early calculations of supersonic infall by Harwit et al. [1987] showed that, despite a succession of layers of highly or partially ionized gases, and neutral components separating the tenu-

ous, high-velocity impacting gas from a cold, relatively dense neutral layer in a galaxy's plane, the pressure P remains constant throughout such a layered stack. Thus the pressure exerted on a galaxy's impact area, if large compared to the scale height of the gaseous component, is also the compressive pressure on a cold cloud in the galaxy's plane. Recent studies devoted to infall into massive cluster haloes rather than single galaxies are based on similar hydrodynamic considerations [Birnboim and Dekel, 2011]. Roughly similar approaches have been undertaken by Faucher-Giguère et al. [2011]. While highly interesting, these studies still await observational confirmation, which may take some years to obtain. The connection to the infall of clumps into haloes, and their ultimate impact onto the individual galaxies observed in the SDSS survey, will be discussed below, in sections 3.7 and 3.8.

Supersonic infall creates turbulence that intersperses infalling gas with cold neutral components and leads both to compression and eventual diffusive mixing. The rapid cooling of molecular gases, implied by the uniformly low 10 K temperatures pointed out earlier, ultimately also dissipates turbulent structures, leaving the cold gas compressed, at the same temperature $T \sim 10$ K it had before infall, and with a sufficiently low virial coefficient to collapse. The compression ratio Ψ in this adiabatic sequence is $\gtrsim 4$; its value will depend in part on the ratio of heat capacities $\gamma = c_p/c_v$ in the various turbulent gaseous strata, and in part on the rate of conversion of atomic into molecular hydrogen. Even a value of $\Psi = 4$, however, will diminish the free-fall collapse time by a factor of $\sqrt{8}$, and thereby greatly accelerate, even if it does not initiate, collapse and star formation. An acceleration by a factor of 3 in a pre-stellar free-fall collapse, which otherwise might require $\gtrsim 10^7$ yr is significant. Galactic rotational periods are of order 10^8 yr, so that impact of extragalactic matter on a particular area of a

galaxy, will generally produce pressure on this area for no more than $\sim 10^7$ yr. Over longer periods, the galaxy's rotation gradually moves an impacted area out of the infalling stream that subsequently may fall on neighboring areas.

In summary, clumps of intergalactic matter in haloes, in the density range and with a mass-infall rate indicated by equation (3.9), appear able to both shock-compress and turbulently mix with native cold gases in a galaxy, in times that suffice for the gas to cool to ~ 10 K, dissipate the turbulence, and collapse in free-fall over times of order 10^7 yr.

Relevant to the discussion also is work by Elmegreen [1993], which lays the theoretical foundation linking the pressure of the ISM, and the ambient UV radiation field to the resulting fraction of hydrogen in its molecular form, predicting a nearly linear relationship, $R_{mol} \propto P^{1.2}$ where R_{mol} represents the fraction of hydrogen in molecular form. Recent work by other authors have refined this prediction based on empirical observations and simulations, lowering the power law index to $\sim$0.9 [Wong and Blitz, 2002, Blitz and Rosolowsky, 2006, Robertson and Kravtsov, 2008, Leroy et al., 2008].

None of this is meant to deny that supernovae trigger star formation as well. The observational evidence for their *propagation* of star formation is clear. But the strong correlation of low metallicity with star formation in SDSS galaxies suggests that star formation is initiated by infall; once initiated, star formation is then propagated further by supernova action. Hydrodynamic instabilities have a role as well, but the additional pressures exerted by infall and/or explosive ejecta can compress and accelerate the collapse of unstable neighboring regions to give rise to observed O and B star associations. In addition, although it is by now well established that regions of star formation line spiral arms, the

limited spectroscopic aperture of the present study focuses attention on the central portions of galaxies, where spiral arms become less distinct. Our data thus lack observations that could meaningfully add to a discussion of star formation in spiral arms.

Finally, we note that Ellison et al. [2008] originally demonstrated a correlation of higher metallicity with lower radii in galaxies of identical mass, and a similar correlation of higher metallicity with lower star formation rates. Equation (3.7) provides a physical explanation of why infall rates should diminish with diminishing radius; and equation (3.1) shows why lower infall rates diminish dilution of the intrinsic metallicities of native gas clouds and thus lead to the observed higher metallicities. Equation (3.2) further shows that diminishing infall rates result in diminishing star formation.

It may be useful, at this point, to still mention that the relation between $(\mathrm{SFR}) \propto \dot{M}_i^{3/2}$ in equation (3.2) has a superficial resemblance to the Schmidt-Kennicutt (SK) law, $\Sigma_{(SFR)} \propto \Sigma_{gas}^{1.4}$ [Kennicutt, 1998b]. Roughly equally good fits to the metallicity dilution could be found with $(\mathrm{SFR}) \propto \dot{M}_i^{1.4}$. The SK law, however, deals with the areal density of the native gas in a galaxy, whereas $\dot{M}_i^{3/2}$ refers to the pressure infalling gas may exert.

We next turn to a justification of the physical parameters given in equation (3.9).

3.6 Representative Values of s and V

The wealth of available SDSS data permits us to derive representative values of s, V and $\langle\rho\rangle$ by means of relations (3.6), (3.7), and (3.2). We obtain these values for a sampling of galaxies on the galaxy main sequence, i.e., for the most populous and typical galaxy sample available in our data. We define our observed main sequence as the straight line in log-log space: Log(SFR)=1.12$\times$Log(M_*)-11.74. Along this straight line we have picked five sets of values of galaxy mass and SFR more or less equidistant along the most populated portion of our main sequence. At each SFR/M_* position we extract a set of sources within a small Log(SFR) / Log(M_*) range of $\pm$0.02 and take the median Petrosian half-light radius to be representative of the entire set. The five sets are summarized in Table 3.4.

We do not know precisely where the infalling material is stopped through interaction with gas in the galaxy, or exactly what fraction of the mass within that radius is stellar, as contrasted to dark matter. We assume in the equations below that infalling mass is stopped at around two Petrosian radii, and that the enclosed mass within that radius is composed largely of stellar and dark matter with a total mass of $\sim 2\times M_*$. This is roughly consistent with data published by Leier et al. [2011], who plotted the distribution of stellar mass and total gravitational mass in lensing galaxies (see Leier et al. [2011] Figure 5). Their total enclosed mass, which they term *lensing mass*, plotted as a function of effective, i.e., half-light radius, varies with galaxy stellar mass, but for the range of masses we consider, their ratio of total mass to stellar mass, enclosed within two half-light radii, is roughly 2 to $3M_*$, with sizable error bars.

Table 3.4 SFRs, Masses, and Radii for Typical Main Sequence Galaxies

Galaxy Set	(SFR) $M_\odot$/yr	$(SFR)^{2/3}$ $(M_\odot/yr)^{2/3}$	M_* $M_\odot$	r_{50} kpc	# sources	$\langle\rho\rangle/\alpha$ at V=170 km/s (g cm^{-3})×(s g^{-1})$^{1/3}$
1	0.209	0.352	0.71×10^{10}	4.2	62	1.0×10^{-36}
2	0.417	0.558	1.3×10^{10}	4.1	141	1.3×10^{-36}
3	0.813	0.871	2.4×10^{10}	4.4	167	1.3×10^{-36}
4	1.51	1.32	4.0×10^{10}	4.9	127	1.3×10^{-36}
5	3.16	2.15	7.9×10^{10}	5.6	64	1.0×10^{-36}

We next solve for ρ and α using equations (3.6), (3.7), and (3.2), finding

$$\langle\rho\rangle/\alpha = \frac{1}{\pi V}\frac{SFR^{2/3}}{r^2}\left(1+\frac{2MG}{rV^2}\right)^{-1} . \tag{3.10}$$

Based on the assumptions that V has some common characteristic value and $\langle\rho\rangle$ is also more or less constant when averaged over infall rates on main sequence galaxies, we consider a range of V values and examine the resulting $\langle\rho\rangle/\alpha$ values for each of our five sets of sources. Due to scatter in the data, some difference in the resulting $\langle\rho\rangle/\alpha$ values for our five sets is inevitable. In figure 3.3, however, we show that there is a distinct minimum in this scatter at a V value of 170 km/s. Specifically, this is where the standard deviation of $\langle\rho\rangle/\alpha$ among the five source sets normalized by the mean value, reaches a minimum. The corresponding mean $\langle\rho\rangle/\alpha$ value is 1.2×10^{-36} (g cm^{-3})(s g^{-1})$^{1/3}$.

That the infall velocity at large distances, V is as high as ~ 170 km s^{-1} may be an indication that gas flowing into a halo containing a group of galaxies acquires this high velocity on falling into the halo, and then impinges on the galaxies without significant further acceleration. For a halo with radius ~ 300 kpc and mass $\sim 10^{12} M_\odot$, infall velocities of this order would be expected; a more precise

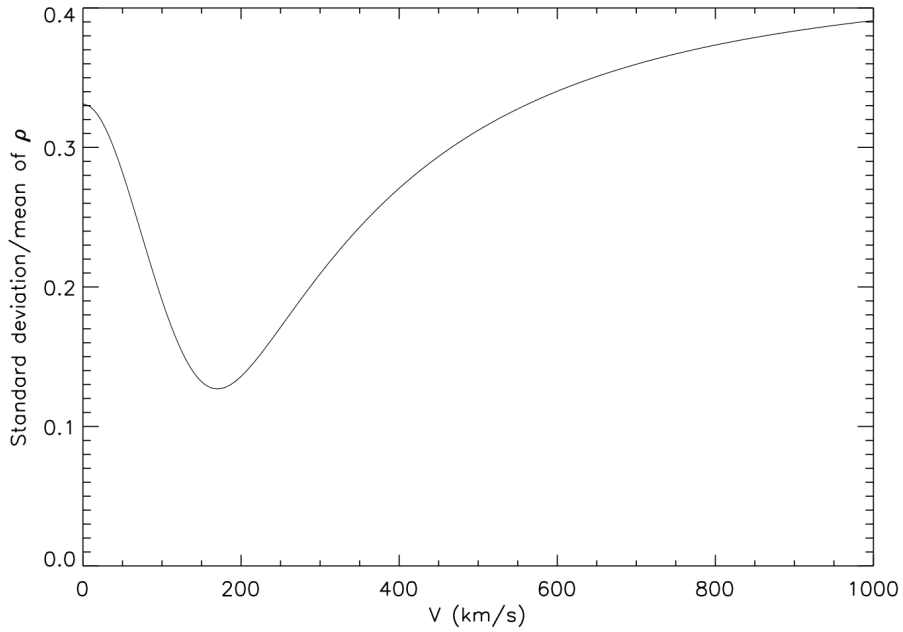

Figure 3.3 Scatter of ρ/α as a function of V

value would require knowing the radial distribution of the dark matter within the halo. Velocities of this order may thus be compared to those obtained from simulations of infall into haloes such as those recently calculated by Klypin et al. [2011].

Our estimate of an approach velocity of 170 km s^{-1} is in rough agreement with estimates of V based on the dispersion of line of sight velocities of galaxies in groups and poor clusters, with a range of radial (line-of-sight) velocity dispersion of 100-500 km s^{-1} and a median radial velocity dispersion of ~ 250 km s^{-1} [Allen and Cox, 1999].

Adopting a representative mutual approach velocity $V \sim 170$ km s^{-1} for present purposes and setting $\alpha(SFR)^{2/3}$ equal to the mass infall rate $\dot{M}_i$, we solve for $\langle\rho\rangle$ with the help of equations (3.7) and (3.2), by writing

$$\langle\rho\rangle = \frac{\dot{M}_i}{\pi s^2 V} = \frac{\alpha(SFR)^{2/3}}{\pi s^2 V} \, . \tag{3.11}$$

With the parameters given for the five galaxies in Table 3.4, we obtain a mean mass density $\langle\rho\rangle = (\frac{\alpha}{(M_\odot/yr)^{1/3}})4.8 \times 10^{-28}$ g cm^{-3}.

In section 3.6, below, we seek a value of α consistent with available observations in order to obtain an actual estimate of mean clump density $\langle\rho\rangle$.

3.7 Difference Between Infall and Star Formation Rates, α

In section 3.4, we found that $\alpha\tau_i M_*/M_g$ has a median value of $\sim 2.3 \times 10^9$ (yr^2 M$_\odot$)$^{1/3}$. For a typical galaxy with $M_g/M_* = 5\%$, this yields $\alpha\tau_i \sim 1.15 \times 10^8$ (yr^2 M$_\odot$)$^{1/3}$. We now return to our example of Figure 3.2, where we dealt with galaxies of mass $0.5 \times 10^{10} M_\odot$. It is useful to recast equation (3.1) in the form

$$\dot{M}_i\tau_i = \alpha SFR^{2/3}\tau_i = \frac{Z_0 - Z_x}{Z_x - Z_i} M_g. \tag{3.12}$$

Looking at the metallicities of the most vigorously star forming samples in Figure 3.2, we find that the infalling mass of gas corresponds roughly to 57% of M_g. For $M_g/M_* = 0.05$ we then obtain an infall time of $\tau_i \sim 1.4 \times 10^8 M_\odot/(\alpha(SFR)^{2/3}) \sim 1 \times 10^8 / \left(\frac{\alpha}{M_\odot^{1/3} yr^{-1/3}}\right)$ yr. A value of $\alpha = 10$, would reduce the required infall time to $\sim 10^7$ yr, comparable to the time that gas falling onto a limited portion of a galaxy would impinge there before the galaxy's rotation moved neighboring regions in the galaxy into the infalling stream.

An alternative estimate of α is obtained from parameters derived in section 3.5 that would produce a pressure sufficiently high to trigger or accelerate free-fall collapse. For $P \sim (\dot{M}_i v/A) \sim \alpha(SFR)^{2/3} v/A$ and an infall velocity, as given by equation (3.5), $v = (s/r)V \sim \sqrt{3}V \sim 294$ km s^{-1}, the infall pressure

$P(1M_\odot\ \mathrm{yr}^{-1}\ \mathrm{kpc}^{-1}) \sim 1.3 \times 10^{-10}$ dyn cm^{-2}, where we have taken $V = 170$ km s^{-1}. Exceeding the internal molecular cloud pressure then would require $\alpha \geq 1$.

Another estimate of α may be suggestive: Spectra have by now been obtained for approximately 6×10^5 SDSS galaxies in our redshift range. Roughly 17% of these have indications of star formation and are included in our tables. If 17% of the galaxies have measurable star formation rates, 17% of a typical halo volume should be filled with clumps of density $\langle\rho\rangle = 4.8 \times 10^{-28} \left(\frac{\alpha}{M_\odot^{1/3} yr^{-1/3}}\right)$ g cm^{-3}, and the gaseous mass density of the haloes should be $8.2 \times 10^{-29} \left(\frac{\alpha}{M_\odot^{1/3} yr^{-1/3}}\right)$ g cm^{-3}. For the above-cited halo of radius 300 kpc, the total clump mass would then be $\sim\ 2.7 \times 10^{44} \left(\frac{\alpha}{M_\odot^{1/3} yr^{-1/3}}\right)$ g, or $13.7 \times 10^{10} (\frac{\alpha}{M_\odot yr^{-1}}) M_\odot$. This suggests that α should not greatly exceed $\alpha \sim 1$ to 3; otherwise the fraction of clump mass in the halo would begin to approach that of the total halo mass estimated above as $10^{12} M_\odot$.

In summary, it is possible to defend α values in the range of 1-10 $(M_\odot\ \mathrm{yr}^{-1})^{1/3}$, representing the difference between values of $(SFR)^{2/3}$ and $\dot{M}_i$. This also appears roughly compatible with respective durations of Hα emission from HII regions around massive stars formed in the collapse of a giant molecular cloud and the duration of gas infall onto a particular spot of a rotating galaxy.

Ultimately, however, the value of α will have to be established through observations. Extragalactic clumps of gas with mass densities of $\sim 3 \times 10^{-27}$ g cm^{-3} and α values in the range of 1 to 10 $(M_\odot\ \mathrm{yr}^{-1})^{1/3}$, can probably not be detected with currently available instrumentation, but should be searched for, once those capabilities become available.

Values of $\alpha \gtrsim 1$ to 10 in the indicated units also make sense when we recall that $\alpha = \epsilon^{-2/3}$, as discussed in section 3.4. As a coefficient for star formation efficiency $\epsilon \dot{M}_i^{1/2}$, one can only expect ϵ to exhibit values $\epsilon \leq 1$. If α is as high as 10, ϵ would have to be of order 0.03. Krumholz et al. [2012] estimate star formation rates of $SFR = f(H_2)\epsilon_{ff}[32G\rho^3/3\pi]^{1/2}$, where $f(H_2)$ is the fraction of gas in the form of molecular hydrogen. They estimate the free-fall efficiency $f(H_2)\epsilon_{ff}$ to be of order 1%. Within reasonable uncertainties, this suggests that an estimate of $\epsilon \sim 0.03$, and thus $\alpha \sim 10$ also lies within an acceptable range.

3.8 Summary and Discussion

We have shown that for a large fraction of the galaxies whose central regions were observed in the Sloan Digital Sky Survey, the observed gas metallicities, Z_x, are consistent with (i) a quantitative physical relation for star formation through episodic infall of gas devoid of heavy elements; (ii) thorough mixing of infalling and native gas before onset of star formation; (iii) a star formation rate proportional to the 3/2 power of the infalling mass rate, $\dot{M}_i$; and (iv) intermittent quiescent phases devoid of star formation during which the native gas in a galaxy exhibits a characteristic elevated gas metallicity, Z_0, dependent on galaxy mass, M_*, and a characteristic mean ratio of stellar mass to native mass of gas, M_g. Most if not all our SDSS star-forming galaxies with $M_* < 2.0 \times 10^{10} M_\odot$, and many with $M_* \geq 2.0 \times 10^{10} M_\odot$ and large radii appear fed by infall. Sets of galaxies not obeying these relations invariably have masses $M_* \geq 2.0 \times 10^{10} M_\odot$ and exhibit high metallicities at high star formation rates, suggesting that for these galaxies star formation independent of mass infall plays a significant role.

These features are largely reproduced by a mean-field-theory toy model for the physics of infall, which accounts for the $(SFR) \propto \dot{M}_i^{3/2}$ relation in terms of the pressure infalling gas exerts on native gas in a galaxy to trigger, or at least accelerate, star formation. The model also permits us to estimate the mean densities and velocities of clumps of baryonic matter traversing the dark matter halos in which the SDSS galaxies may be embedded.

This is as much conformance to our data as can be expected from a mean-field-theory toy model, which of necessity disregards variations in velocity V, variations in clump densities ρ, and selection effects that favor detection of larger, more massive galaxies at higher redshifts, and smaller, less massive and less luminous galaxies at lower redshifts. But it suggests that the basic features of the model capture the essence of population distributions and metallicities found in SDSS star forming galaxies.

A number of papers published in recent years have discussed the absolute value of chemical enrichment in galaxies [Brooks et al., 2007, Kobayashi et al., 2007, Finlator and Davé, 2008]; modeling the processes involved requires consideration of the chemical constituents of supernova ejecta, their ejection velocities, the gravitational potentials of the parent galaxies, and thus calculations on the rate of retention of metals in galaxies of different types and masses. As pointed out by Genel et al. [2009], past merger history can also be an important factor. A number of authors, most recently Leitner and Kravtsov [2011] have also considered the extent to which winds from evolved stars may generate sufficient gas to keep up star formation within quiescent galaxies at a low level on a continual basis, particularly in massive galaxies. While of great interest, a detailed understanding of these effects will require calculations and

detailed modeling beyond the scope of the present paper, as do recent attempts by Bouché et al. [2010] and Shi et al. [2011] to model SFRs through new star-formation laws. Much of this theoretical work is still tentative and will need to be tested by accumulating observational evidence. Some theoretical predictions could potentially be tested against the quantitative metallicity relations brought out in the present paper.

Of particular interest to such studies may be the upper limits to the metallicity of infalling material that our study indicates, $\sim 0.125 \times 10^{-3} \pm 0.125 \times 10^{-3}$ N(O)/N(H). This appears to be a useful constraint on the metallicity of material transiting galaxy halos and falling into the galaxies.

CHAPTER 4

STRONG C^+ EMISSION IN GALAXIES AT Z$\sim$1-2: EVIDENCE FOR COLD FLOW ACCRETION POWERED STAR FORMATION IN THE EARLY UNIVERSE

4.1 Introduction

With recent developments in submillimeter spectroscopy including the conclusion of extensive observations with the Herschel Space Observatory[1] [Pilbratt et al., 2010], the inauguration of ALMA, and the ongoing developments with other ground-based interferometers and large single disk telescopes, the study of the redshifted Universe in the far infrared (FIR) has come into its prime.

Emission from ionized carbon is one important tool for FIR studies of early galaxies. Carbon is the fourth most abundant element in the Universe, and it takes 11.3 eV photons to form C+, so the low-lying (91 K above ground) 158 μm [CII] fine-structure line was long ago predicted to be the dominant coolant of the neutral ISM [Dalgarno and McCray, 1972]. The [CII] line is also usually optically thin and suffers very little extinction, so it is an excellent probe of the properties of the atomic gas heated by the far-UV (6 - 13.6 eV) flux in galaxies. Indeed, the first [CII] detections from local galaxies revealed that the [CII] line can be the brightest single emission line from star forming galaxies, amounting

*This chapter is an adapted version of the submitted article, Brisbin et al. (2014).

[1]Herschel is an ESA space observatory with science instruments provided by European-led Principal Investigator consortia and with important participation from NASA.

to between 0.1 and 1% of the total FIR luminosity[2] [Crawford et al., 1985, Stacey et al., 1991].

The [CII] line luminosity is closely correlated with CO emission. Thus, while some [CII] does arise in ionized gas, a picture has emerged where most ($\sim$70%) arises from the warm, dense, neutral gas of photo-dissociation regions (PDRs) [Stacey et al., 1991, Oberst et al., 2006]. The PDR heating is dominated by far UV (FUV) radiation from nearby early type stars. Nearly all of the UV intercepted by dust is absorbed and converted to long wavelength thermal emission, giving rise to the FIR continuum. A small fraction ($\sim$1%) of the UV photons eject hot electrons from dust and PAH grains heating the gas which, in turn, collisionally excites the [CII] line [Tielens and Hollenbach, 1985].

For moderate gas densities (n$<10^4$ cm^{-3}) and far-UV field strengths (G$_0$ $<10^3$)[3] that are typical in star forming galaxies averaged over large scales, the [CII] line will be the primary coolant for gas in PDRs. The ratio of this line to the FIR luminosity represents the gas heating as a fraction of the total UV power. It is a first measure of the 'gas heating efficiency'. A more complete measure includes the [OI] 63 μm line, which, due to its higher critical density for thermalization (n$_{crit}\sim4.7\times10^5$ cm^{-3}, vs. 2.8×10^3 cm^{-3} for [CII]) and greater energy above ground for the emitting level (228 K), becomes the dominant PDR coolant at higher densities and G$_0$ [cf. Pound and Wolfire, 2008, Kaufman et al., 2006]. Together, the two fine structure lines constrain n and G$_0$ for PDRs. However, since the gas densities for most galaxies are between 100 and 10^4 cm^{-3}, the [CII]/FIR luminosity ratio is in and of itself is a good tracer of the heating effi-

[2]In this paper FIR refers to 42.5-122.5μm. This is one of the two most common conventions in the literature, the other corresponding to $\sim$40-500μm. For most galactic spectral energy distributions (SEDs,) the integrated luminosity in these two ranges differs by a factor of $\sim$1.5.

[3]G$_0$, the Habing flux, parameterizes the far-UV flux in terms of a typical ISM far-UV flux, G$_0$=F$_{FUV}$/1.6×10^{-6} W m^{-2}

ciency [Stacey et al., 2010b]. In PDR models with moderate densities, [CII]/FIR is inversely proportional to G_0. ISO-based studies showed that [CII]/FIR tends to be an order of magnitude smaller in local Ultra Luminous Infrared Galaxies (ULIRGs; $L_{FIR}>10^{12} L_{\odot}$) relative to normal star forming galaxies - a characteristic sometimes referred to as the '[CII] deficit' [Luhman et al., 2003]. This relationship is surprising as it links an intrinsic galaxy trait, [CII]/FIR, with an extrinsic trait, the total FIR luminosity.

Stacey et al. [2010b] demonstrated that in fact the [CII]/FIR ratio is not intrinsically anti-correlated with L_{FIR}, and the observed [CII] deficit is only indicative of the underlying star formation conditions in local ULIRGs. PDR models demonstrate that low [CII]/FIR on a galactic scale are actually correlated with very intense UV fields ($G_0 \gtrsim 10^4$) in star forming media. In local galaxies the star bursting episodes that give rise to such intense UV fields are largely in the domain of ULIRGs. Recent major mergers leading to localized and very intense star formation are the source of extreme luminosity in these local systems. During the epoch of peak star formation, ULIRGs make up a larger fraction of the total star formation activity, and thus we might expect a continuation of the locally observed [CII] deficit. Stacey et al. [2010b] showed, however, that at z=1-2 systems with extreme (ULIRG and HyLIRG) luminosities do not have suppressed [CII]/FIR ratios or extreme UV fields in general. Stacey et al. [2010b] instead finds that the high luminosity star formation dominated systems in this epoch have very extended star formation regions with more moderate FUV fields. This has contributed to a paradigm shift in the accepted nature of star formation in the early Universe. Rather than being powered solely by major mergers, a significant population of ULIRGs in the early Universe are forming stars in a mode similar to normal local galaxies. The observational data could be explained by

star formation proceeding by cold accretion of gas from the cosmic web which builds to surface densities ∼10-100 times that of the Milky Way. This is often seen in sub-galactic star formation regions nearby and is adequately described by the Schmidt-Kennicutt star formation law [Schmidt, 1959, Kennicutt, 1998a]. We postulate that in these galaxies at high redshift, similar star formation is occurring on a near galaxy-wide scale leading to moderate UV field intensities (G_0 ∼100-1000,) but very large luminosities due to their very large size. This is consistent with several recent findings by Tacconi et al. [2010], Daddi et al. [2010], Ivison et al. [2011], and Riechers et al. [2011], which all show widespread CO emission ∼several kpc in extent and indicate high molecular gas fractions in normal star forming galaxies at a similar epoch. Although they are certainly present in the early Universe [c.f. Ferkinhoff et al., 2014], major mergers are not required to explain the very large intrinsic luminosities ($L>10^{12}L_{\odot}$) in this epoch.

Motivated by the results of our previous work, we have undertaken an expanded [CII] survey of z=1-2 sources with the redshift (z) Early Universe Spectrometer (ZEUS) on CSO; a survey which we have augmented with [OI] 63 μm observations from the Herschel PACS instrument [Poglitsch et al., 2010]. This survey represents the continuation of the original work by Stacey et al. [2010b] in which an equal emphasis was placed on sources determined to be AGN dominant (AGN-D), star formation dominant (SF-D), or of mixed nature. In this follow up survey we have focused on SF-D systems. In this work we confirm that the [CII] deficit is not a ubiquitous trait in star formation powered ULIRGs in the redshift 1-2 epoch. We also find moderately intense (G_0 $\sim 10^{2-3}$) UV fields distributed over very large (several kpc) scales within galaxies. A similar analysis of [OI] 63 μm in the sources from the original Stacey et al. [2010b] sample

can be found in Hailey-Dunsheath et al. [2014].

The characterization of our sources as SF-D is based on evidence from the literature without consideration of our [CII] observations. It can generally be interpreted as a characterization of the dominant power source for the total infrared (TIR) (8-1000 μm). AGN dominant sources have TIR SEDs dominated by the mid-IR (MIR), while SF-D sources have TIR SEDs dominated by the FIR band. Due to the inhomogeneous nature of background data on our varied source set, however, the precise criteria for characterization is not uniform.

In addition to [CII] and [OI], many of our sources have been observed photometrically with PACS [Poglitsch et al., 2010] or SPIRE [Griffin et al., 2010], either as part of our own OT2 program, the Herschel Multi-tiered Extragalactic Survey (HerMES) [Oliver et al., 2012], or the PACS Evolutionary Probe (PEP) survey [Lutz et al., 2011]. We have used these data along with photometry collected from the literature to provide uniformly processed SEDs. In choosing our survey sample we emphasized sources with PAH emission detected in the MIR observed with the Spitzer Infrared Spectrograph (IRS)[4] spectrometer [Houck et al., 2004]. This selection criteria strongly biases our sample towards SF-D systems. We have obtained IRS spectra on seven of our sources to analyze the presence and nature of PAHs.

The structure of the paper is as follows: in section 4.2 we present our observations, including the overall survey methodology; in section 4.3 we discuss notes on individual sources; in section 4.4 we present our data analysis and results for our global sample and individual sources; in section 4.5 we discuss the physical interpretation of our results and their implications for the z>1 Uni-

[4]The IRS was a collaborative venture between Cornell University and Ball Aerospace Corporation funded by NASA through the Jet Propulsion Laboratory and the Ames Research Center.

verse; and finally in section 4.6 we make concluding remarks.

4.2 Instrumentation and Observations

We conducted [CII] observations using ZEUS at the 10.4m Caltech Submillimeter Observatory (CSO) on Mauna Kea. ZEUS is well described in the literature [Stacey et al., 2007, Hailey-Dunsheath, 2009] so we only briefly describe it here. ZEUS is an echelle grating spectrometer designed to operate over the 350 and 450 μm telluric transmission windows. It has a 1$\times$32 pixel thermistor sensed bolometer detector array that yields a 32 element spectrum split into the 350 and 450 μm bands for a single beam. The detector array and optics are designed to maximize sensitivity to broad lines of width $\sim$a few hundred km s^{-1} - well matched for detecting emission lines from distant galaxies. The resolving power varies by wavelength but is $\sim$1000, (velocity resolution $\sim$300km s^{-1},) and each pixel samples one spectral resolution element.

Observations took place over three observing runs in January 2010, January 2011, and March 2011. We used a standard chop-nod observing mode with a chopper frequency of 2 Hz, and a chopper throw of 30". Calibration, including beam size, point-source coupling, and flux calibration, was determined by observations of Uranus, which is assumed to emit like a blackbody with temperature from 61 to 73 K within our wavelength band [Hildebrand et al., 1985]. We spectrally flat-fielded our observations based on observations of a cold chopped source. Source and system parameters relevant for each observation are given in Table 4.1. The ZEUS/CSO beam size is 10.5" at 350 μm and 11.5" at 450 μm, and we estimate that typical pointing errors are less than 3" and systematic cal-

ibration errors are less than 30%. The wavelength calibration is good to about half a pixel, or 100-160 km s^{-1}.

Our [OI] 63 μm observations for six sources were taken using the PACS spectrometer onboard the Herschel Space Observatory. We observed using line scans in chop-nod mode with a small chopper throw. Each [OI] observation had a full integration time (including on and off source integration but not including instrumental overheads) of just under an hour (57.3 minutes,) except for SWIRE 3-14 which is our faintest [CII] source, on which we integrated three times longer (172 minutes.) We reduced the data using the standard pipeline in the Herschel Interactive Processing Environment (HIPE v10.3.0) [Ott, 2010], with minimal post-pipeline processing described in section 4.4.1. Observations were carried out between May and October 2012. The [OI] line was observed in SDSS J12 using the PACS chop-nod mapping mode as part of a cycle 2 open time program by Sangeeta Malhotra.

All sources except for SMM J03 lie in regions surveyed by the HerMES or PEP projects (PIs Oliver and Lutz, respectively) from which we obtained photometric measurements. We conducted photometric observations of SMM J03 using the PACS blue and green cameras (which provide simultaneous red coverage resulting in observations at all three PACS wavebands - 70, 100, and 160 μm). We took two scan maps with each camera, one at an orientation of 110 and one at 70 degrees with respect to the camera array for optimal spatial coverage and minimal CCD latency effects after cross stitching. Scans were performed at medium speed, with 3 arcminute scan legs, a cross scan step of 4 arcseconds and a total of 10 scan legs. Total integration time including all four scan maps (without instrumental overhead,) was six minutes.

Table 4.1 ZEUS Observing log. Average line of sight transmission is indicated by t_{los}. In the text we refer to sources by their names in parentheses.

Source	RA	Dec.	$z_{[CII]}$	Obs. Dates	t_{los}
MIPS 22530	17h23m03.3s	59d16m00.2s	1.9501	3/15/2011	15.4%
SWIRE3 J104343.93+571322.5 (SWIRE 3-9)	10h43m43.9s	57d13m22.5s	1.7348	3/18/11	23.9%
SWIRE3 J104514.38+575708.8 (SWIRE 3-14)	10h45m14.4s	57d57m08.8s	1.7795	1/07/10, 3/17/11	31%
SWIRE3 J104632.93+563530.2 (SWIRE 3-18)	10h46m32.9s	56d35m30s	1.771	12/31/10	22.5%
SMM J030227.73 +000653.5 (SMM J03)	03h02m27.7s	00d06m52.0s	1.4076	1/4/11	16%
SWIRE4 J104427.52+584309.6 (SWIRE 4-5)	10h44m27.52s	58d43m09.6s	1.7560	1/24/11	36%
SWIRE4 J104656.46+590235.5 (SWIRE 4-15)	10h46m56.46s	59d02m35.5s	1.8544	3/16/11	30%
SDSS J120602.09+514229.5 (SDSS J12)	12h06m01.71s	51d42m27.6s	1.9985	3/17/11	21.5%

4.3 Notes on observations of individual systems

Several of our sources were initially discovered as part of the Spitzer Wide-area InfraRed Extragalactic (SWIRE) survey [Lonsdale et al., 2003], which undertook deep photometric observations of several different fields. High-z candidates showed bumps in the 4.5, or 5.8 μm IRAC bands or the MIPS 24 μm band, indicating a redshifted stellar photospheric 1.6 μm feature or PAH emission at z$\sim$2. Both types of features strongly suggest star formation. The 1.6 μm feature particularly selects for late type evolved stars, but it can be overwhelmed by a strong AGN contribution, so its presence in a FIR bright galaxy suggests star formation as the dominant power source [Farrah et al., 2006, 2008, Lonsdale et al., 2009, Huang et al., 2009, Desai et al., 2009]. As presented in Fiolet et al. [2009] and Farrah et al. [2008], these sources were followed up with MIR IRS spectra to look for PAH features.

SWIRE 4-15 IRS observations in Fiolet et al. [2010] (source L15) showed strong PAH features and indicated a (PAH determined) redshift, z=1.85 $\pm$ 0.01. This, in conjunction with further photometry from Spitzer and SCUBA showing no significant presence of hot dust, strongly indicates a SF-D system with little to no contribution from AGN.

SWIRE 4-5 IRS follow up of this source revealed strong PAH features and a redshift z=1.750$\pm$0.007 [source L5, Fiolet et al., 2010].

SWIRE 3-14 Farrah et al. [2008] find a PAH determined redshift of z=1.78.

SWIRE 3-9 Another SWIRE source suspected of being at z$\sim$2, PAH spectrum acquired by Farrah et al. [2008], showed this to have a MIR spectrum with continuum and PAHs characteristic of a SF-D system, with no contribution from an AGN. Their PAH derived redshift is z=1.71.

SWIRE 3-18 This source was selected for MIR spectral follow up by Farrah et al. [2008]. It's MIR spectrum shows strong PAH features indicative of SF dominance. Prior to our [CII] detection, only a PAH determined redshift of z=1.76 had been established. Our [CII] detection refines this to 1.771. Although it has been observed with IRS, little other data is known for this source. Our interest in it arose too late to include it in our [OI] Herschel survey.

SMM J03 Based on optical and UV lines probing the ionized gas, SMM J03 is thought to have an AGN component [Swinbank et al., 2004, Takata et al., 2006]. Looking at the UV spectral diagnostics along with the bolometric luminosity, however, Chapman et al. [2005] found that the AGN contributes insignificantly to the overall luminous energy. We therefore consider it to be SF-D. This is a well studied submillimeter galaxy (SMG) with extensive photometry available

in the literature, in the optical, NIR and the radio regime. Rest frame optical spectroscopy reveals a redshift of z=1.4076 [Swinbank et al., 2004].

SDSS J12 ('The Clone') This is a UV bright lensed source with a magnification ~ 27 [Lin et al., 2009]. It was discovered as the counterpart to the lensing galaxy at z=0.4 in the Sloan Digital Sky Survey (SDSS). An analysis of rest frame optical lines, [OIII], Hβ, [NII], and Hα by Hainline et al. [2009a] found SDSS J12 to share characteristics of local star forming systems, but with stronger ionized emission, indicating particularly vigorous star formation. MIR follow up by Fadely et al. [2010] confirms the nature of this source, showing strong PAH features and a lack of a hot dust component. Several spectral lines observed in emission from SDSS J12 have indicated redshifts in the range z=1.9967-2.0026 [Lin et al., 2009, Hainline et al., 2009a].

MIPS 22530 This source was selected as a potential z$\sim$2 galaxy from the Spitzer Extragalactic First Look Survey (XFLS) based on its 24 / 8 μm flux ratio, which indicated strong redshifted PAH emission [Yan et al., 2007]. Multiwavelength analysis by Sajina et al. [2008] finds a borderline indication of AGN powered radio emission, but shows a lack of AGN presence in optical lines. This, along with strong PAH emission, leads them to conclude it is a SF-D system. Keck spectroscopy by Yan et al. [2007] reveal an optical redshift of z=1.9511.

4.4 Results and analysis

Here we give an overview of the results that define several aspects of our sample as a whole, followed by analysis of the individual systems.

4.4.1 Line spectra

We have detected eight 1<z<2 sources in [CII] with ZEUS, representing a significant increase in the population of sources detected in this line during the epoch of peak star formation. In Figure 4.1 we show the [CII] spectra from these eight sources. Although several of our sources are likely to be lensed, the apparent [CII] luminosities span a range of 1.3 - 6.7 $\times 10^{10} L_{\odot}$.

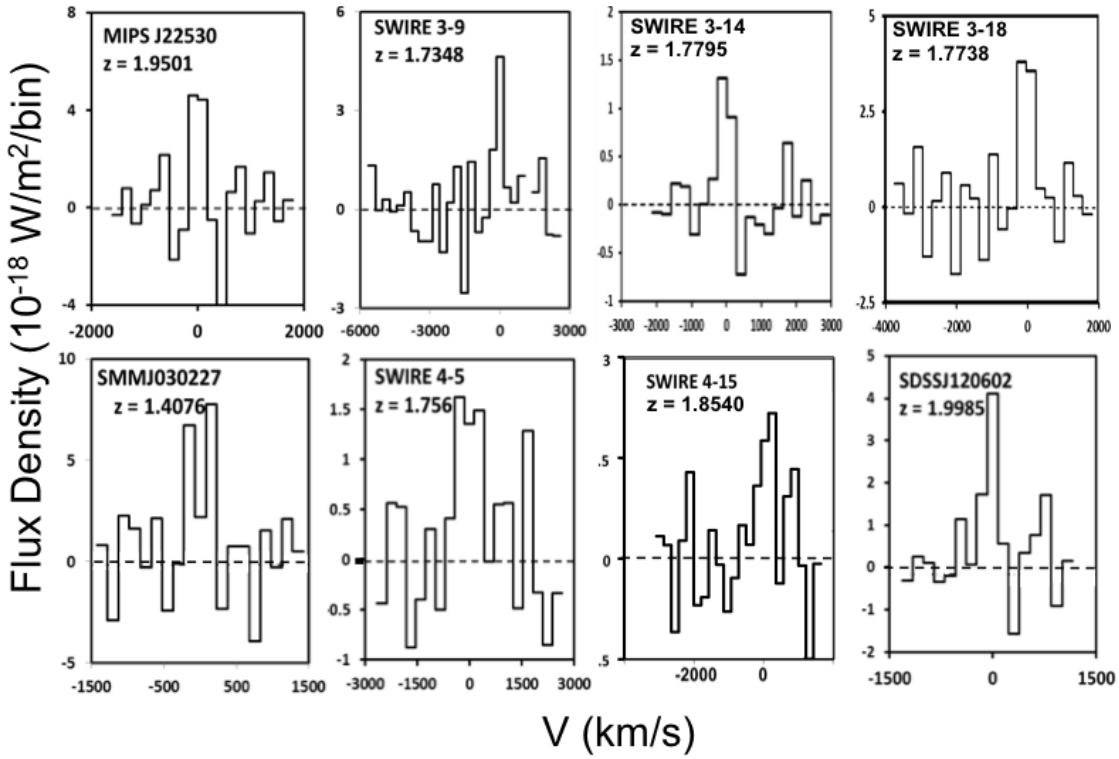

Figure 4.1 ZEUS/CSO [CII] spectra of the eight galaxies reported here. Each spectral bin is one resolution element of the spectrometer and is statistically independent from its neighbors. The velocity scale is centered on the [CII] line center.

The [OI] spectra for the six sources we observed in our Herschel PACS [OI] survey plus one observed by Sangeeta Malhotra (reduced here from archival data,) are plotted in Figure 4.2. The [OI] spectra were reduced through standard methods using HIPE. In post-processing we rebinned them to resolutions ∼120

to 350 km s^{-1} and removed a linear baseline where no line emission was evident. Line fluxes are tabulated in Table 4.2.

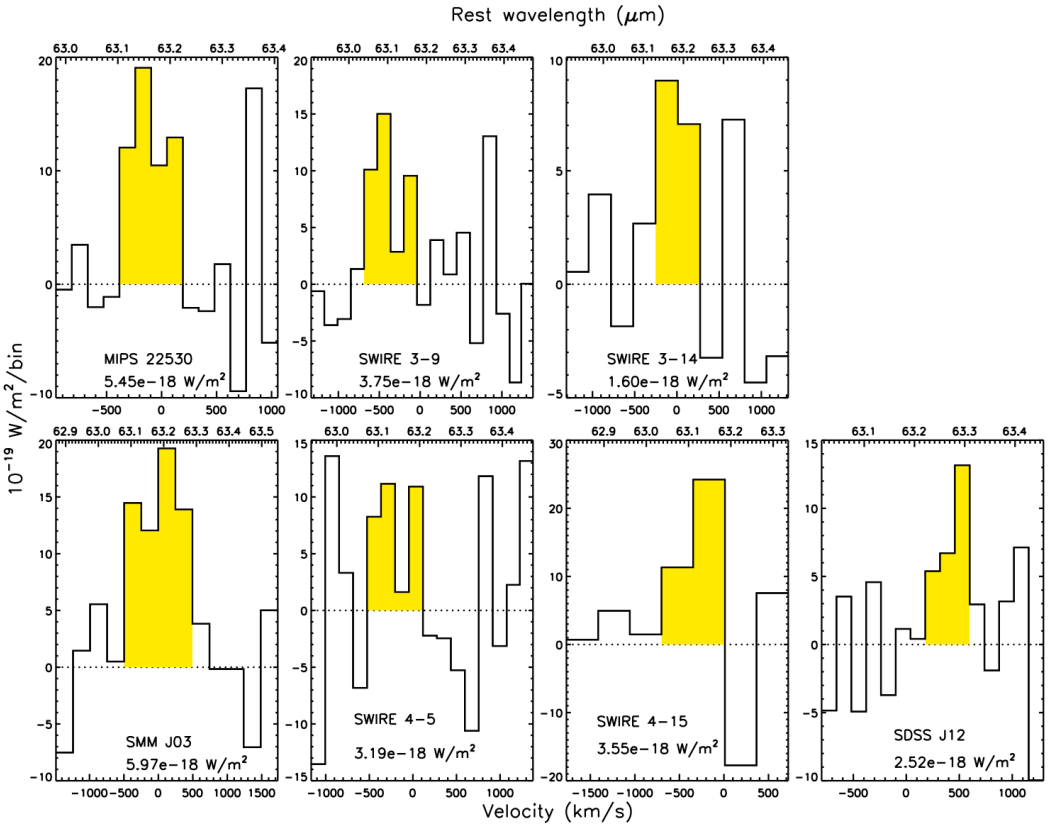

Figure 4.2 The PACS [OI] spectra from the six sources observed in our Herschel program and SDSS J12, observed by PI Sangeeta Malhotra. Velocities are with respect to our [CII] line center. Region shaded in yellow indicates the area integrated to determine line flux.

The [OI] line is clearly detected in six of the seven sources, and marginally detected in SWIRE 4-5 (discussed in section 4.4.6.) In a few sources we observe offsets from the [CII] line velocity by ∼250 km s^{-1}. The velocity resolution in our [CII] spectrum is low, however, and a slight calibration error could introduce a velocity error of ∼200km s^{-1}, so the offset between [OI] and [CII] is acceptable and does not require a physical explanation.

Table 4.2 Fine structure lines and FIR photometry.

Source	L_{FIR} ($10^{12} L_{\odot}$)	$F_{[CII]}$ (10^{-18} W m^{-2})	$F_{[OI]}$ (10^{-18} W m^{-2})	$\frac{F_{[OI]}}{F_{[CII]}}$	$\frac{S_{70}}{S_{100}}$	R≡[CII]/FIR
MIPS 22530	5.56 ±0.60	9.3±2.1	5.45±1.07	0.59	1.09±0.13	1.21E-2
SWIRE 3-9	2.97 ±1.46	6.4±1.4	3.75±0.78	0.59	0.85±0.2	1.16E-2
SWIRE 3-14	1.99 ±0.98	2.32±0.42	1.60±0.48	0.69	0.80±0.16	6.74E-3
SWIRE 3-18	3.3±1.2	7.3±1.3	-	-	0.78±0.22	1.25E-2
SMM J03	3.74±0.40	16.9 ±3.5	5.97±0.86	0.35	1.16±0.11	1.46E-2
SWIRE 4-5	1.34 ±0.90	4.5±1.1	3.19±1.0 1	0.71	0.65±0.41	1.86E-2
SWIRE 4-15	1.78±0.33	5.0±1.3	3.55±0.90	0.71	0.73±0.12	1.79E-2
SDSS J12	3.33 ±0.40	5.6±1.4	2.52 ±0.47	0.45	1.35±0.26	1.30E-2

4.4.2 Photometry and SEDs

The photometry from our PACS program and the literature is compiled in Table B.1 in the appendix. To estimate FIR properties such as L_{FIR} and the 70 to 100 μm flux ratio in a uniform manner (Table 4.2) we fit star formation SED models from Siebenmorgen and Krügel [2007] to available photometry. The SED library consists of a set of ∼7000 SED templates constructed by radiative transfer modeling of a nuclear concentration of massive young stars embedded in a matrix of gas and dust referred to as "hot spots". The templates vary in their stellar input spectrum (fraction of stellar luminosity coming from O and B stars), total luminosity, the size of active star formation, visual extinction from nucleus to galactic edge, and dust density within star formation hot spots.

The SED models have generally performed well at modeling local star forming galaxies. We compared each template against available photometry weighted by error[5] and formed likelihood functions to determine L_{FIR} and

[5]In our sources, SPIRE photometry is affected by confusion. We apply a 30% uncertainty to these measurements to account for this. At these redshifts the MIPS 24 μm measurement is affected by PAH emission. Although the SED models do include PAH features, the template grid is too coarse to allow fine distinction between PAH feature fluxes. A strong constraint on fluxes in the affected part of the MIR spectrum can inappropriately narrow the SED template

70/100 μm flux ratios along with their corresponding 68 percentile likelihood range.

Initial fits showed that several of our sources demonstrated a sub-mm excess observed in the SPIRE bands above the template model fluxes. This was most apparent in our two sources with the highest [CII]/FIR and lowest 70 to 100 μm flux ratios, SWIRE 4-5 and SWIRE 4-15. There are other templates within the SED library which adequately capture the sub-mm excess, however, they all correspond to models with lower absolute luminosities (i.e. the SED profile shape is correct but offset to lower luminosities.) Based on this finding we introduced a variable scaling parameter allowing the entire SED model to shift up or down by a multiplicative constant. As seen in Figure 4.3, the fits were much improved with scaling factors $\sim$50-350, and accurately captured the long wavelength peak in these high [CII]/FIR sources. We tested the improvement in the fit with a likelihood ratio test and found that even with the additional statistical burden of an extra degree of freedom, the fits with the scaling factor were better. For both of these sources, there is a $>$99% likelihood that the scaled model fit better represents the data over an unscaled model.

The physical explanation of this has to do with limitations on the star forming regions in our models. The bulk of the SED models represent local systems with active star formation region spatial scales $\sim$0.35-3 kpc containing young O and B stars. The higher luminosity SEDs contain more O and B stars, but still in small spatial regions, resulting in hotter dust and an SED peak shifting to shorter wavelengths. There is a clear trend in the templates of increasing 70 to 100 μm flux ratios with increasing luminosity. Most of our sources lie just be-

selection, and adversely affect the fit to the FIR dust peak. We weight the 24 μm measurements as if their errors were a factor of ten larger to prevent them from dominating the SED fit.

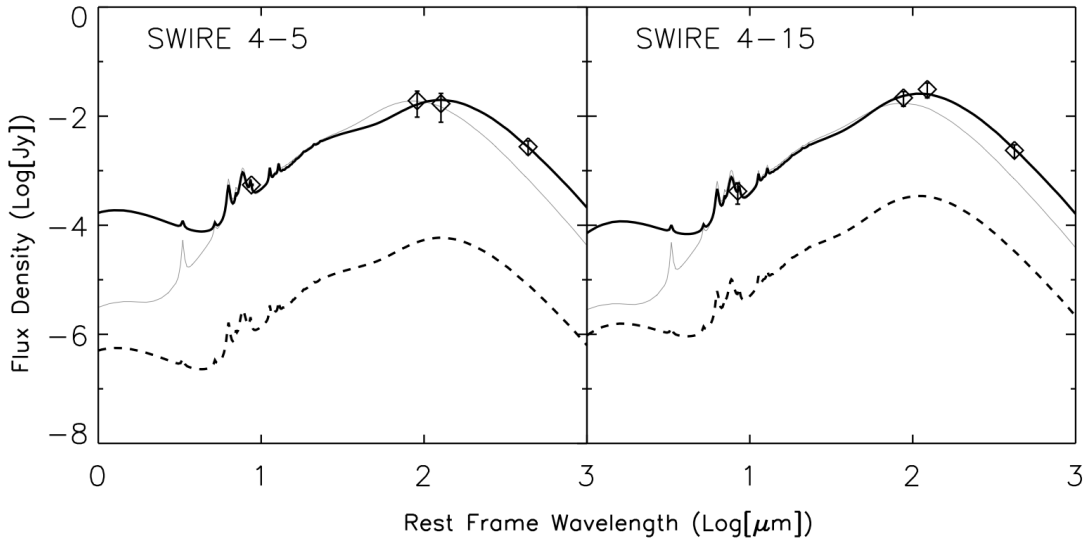

Figure 4.3 SWIRE 4-5 (left) and SWIRE 4-15 (right) photometry shown with SED fit overlaid. The thin solid line demonstrates the best fit model from the library of Siebenmorgen and Krügel [2007], and underestimates the sub-mm flux received in SPIRE bands. The thick solid line gives the best fit allowing for an arbitrary scaling factor. The dashed line represents the unscaled template.

yond the boundary of L_{FIR} and 70 to 100 μm flux ratio covered by the standard SEDs: they must be made up of what is essentially a superposition of many lower luminosity, lower dust temperature star formation regions.

The occurrence of highly luminous systems with cooler dust peaks at high-z is well established [Elbaz et al., 2011, Symeonidis et al., 2013], and further confirms our general findings that SF-D systems at high-z can be represented as scaled up local star forming systems. The conditions of star formation in our z=1-2 sources give rise to cool dust peaks similar to those of local normal or LIRG class galaxies, but scaled up spatially to account for ULIRG class luminosities. Although not explicitly demanded by all of our sources, we used the scaling-factor-augmented SEDs for all the systems and found improved fits. The compiled photometry and SED fits are displayed in Table B.1 in the appendix and Figure 4.4.

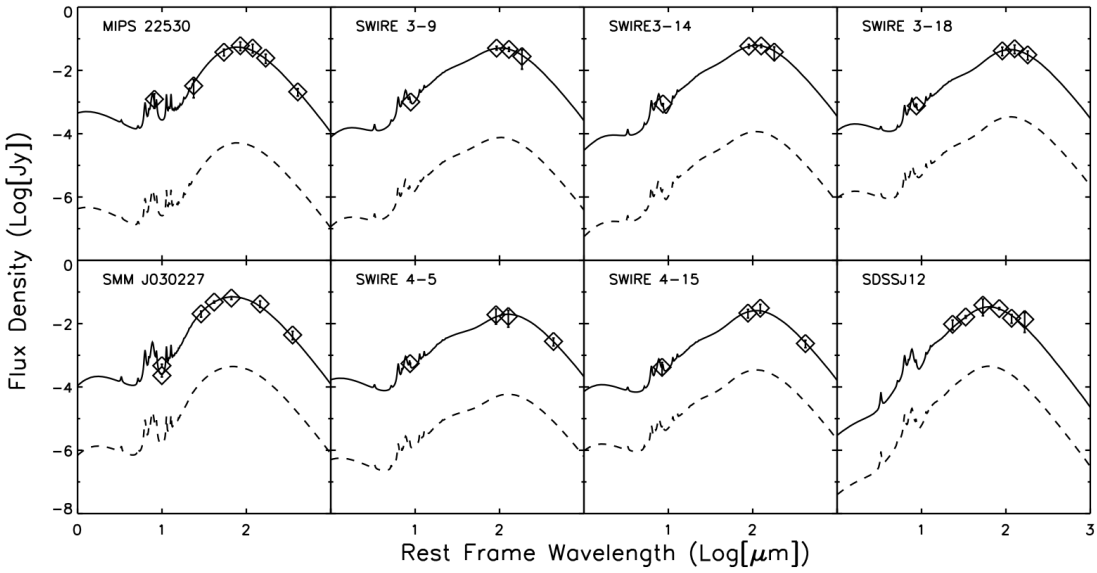

Figure 4.4 The best fit SED model from the library of Siebenmorgen and Krügel [2007] for each of our sources. The initial SEDs (noted by dashed lines) have been scaled up to provide better fits, consistent with our assertion that star formation proceeds on larger spatial scales at redshifts 1-2. Photometry (diamonds) is listed in Table B.1. Note that the PACS and SPIRE observations have been color corrected in these SEDs, resulting in <10% changes in any photometric data point and negligible change in overall L_{FIR}.

To place these sources in context with the larger population of galaxies at these redshifts, we consider their bulk star formation rates (SFRs) and stellar masses. The TIR (8-1000 μm) luminosity, powered largely by dust heated by young stars, is a convenient star formation tracer with a long history of use. We use the TIR - SFR relationship established by Kennicutt [1998a] and adapted by Nordon et al. [2010] to adjust for a Chabrier [2003] IMF:

$$\frac{SFR}{M_{\odot}yr^{-1}} = \frac{L_{TIR}}{L_{\odot}} 1.015 \times 10^{-10}. \tag{4.1}$$

Several methods of estimating galaxy stellar mass based on various photometric recipes have been used in local galaxies. These methods are generally

based on galaxy SED modeling and rely on multiple optical/NIR measurements to break degeneracies in star formation history. A crude but effective estimation can be arrived at based solely on the rest frame galaxy luminosity at $\sim$2 μm, a wavelength which yields surprisingly constant mass to luminosity ratios which are less dependent on star formation histories [de Jong, 1996, Bell et al., 2003]. The effectiveness of the 2 μm luminosity for the purpose of estimating stellar masses has already been demonstrated at z$\sim$3 using IRAC 8 μm measurements [Magdis et al., 2010], and here we extend the approach to z$\sim$1.8 where the appropriate rest wavelength coincides with the IRAC 5.8 μm band. We take this IRAC band to represent the rest frame 2 μm flux and directly use the relationship established by Magdis et al. [2010]:

$$Log(M_*/M_\odot) = 2.01(\pm 0.65) - 0.35(\pm 0.03) \times M_{2\mu m}, \tag{4.2}$$

where $M_{2\mu m}$ represents the rest frame 2 μm absolute magnitude. As is clear from the uncertainty in the coefficients to Equation 4.2, the resulting stellar mass estimate should only be taken as an order of magnitude approximation. Nonetheless, we are reassured that it is an appropriate order of magnitude estimate by the examples of SWIRE 4-5 and SWIRE 4-15. Both of these sources were examined in Fiolet et al. [2009] where careful multi-band photometric stellar estimates yielded 1.36 and 3.21 $\times 10^{11}$ $M_\odot$ respectively. Our simple stellar mass estimates of 1.35 and 2.05 $\times 10^{11}$ $M_\odot$ (noted in Table 4.3 along with SFRs,) are in satisfactory agreement.

In Figure 4.5 we overplot our sources' SFRs and stellar masses on the sample presented by Fiolet et al. [2009]. Although our sample consists of massive, highly star forming sources, it's clear that their relative mass and SFRs (or alter-

Table 4.3 Stellar mass and SFR estimates for sources with IRAC measurements.

Source	L_{TIR} $10^{12}L_{\odot}$	SFR $M_{\odot}$ yr^{-1}	$F_{IRAC5.8}$ mJy	M_{*} $10^{11}M_{\odot}$
MIPS 22530	7.4±1.9	750±190	(4.3±1.0)×10^{-2}	1.4
SWIRE 3-9	8.8±2.9	900±300	(1.12±0.06)×10^{-1}	2.5
SWIRE 3-14	7.9±2.0	800±210	(7.00±0.35)×10^{-2}	1.8
SWIRE 3-18	5.9±2.4	600±250	(6.80±0.34)×10^{-2}	1.7
SMM J03	6.6±0.4	670±40	(8.16±0.83)×10^{-2}	1.2
SWIRE 4-5	3.2±2.1	320±220	(5.36±0.46)×10^{-2}	1.3
SWIRE 4-15	3.7±1.8	380±190	(7.63±0.35)×10^{-2}	2.1

natively their specific star formation rates) fall in line with the trends exhibited by most galaxies, very close to the stacked results of the Fiolet sample. In other words, our sample is part of the galaxy 'main sequence' [Noeske et al., 2007].

4.4.3 [CII] and the FIR continuum

In Figure 4.6 we plot [CII]/FIR vs. L_{FIR}. While the absolute [CII] line luminosity and L_{FIR} may be amplified by gravitational lensing, the FIR continuum and [CII] emitting regions will generally be cospatial in SF-D galaxies, so that the [CII]/FIR ratio is not very susceptible to preferential magnification [Serjeant, 2012]. Quiescent local sources (blue circles) and local ULIRGS (black stars) clearly illustrate the historically reported [CII] deficit [Malhotra et al., 2001, Luhman et al., 2003].

Many of our SF-D sources from this work show [CII] emission with [CII]/FIR ratios in excess of 1%. Although such high [CII]/FIR is unusual, it is not unheard of, and as we show in section 4.4.6 these push models for PDR origins of the [CII] emission to their limits. There are previous examples of

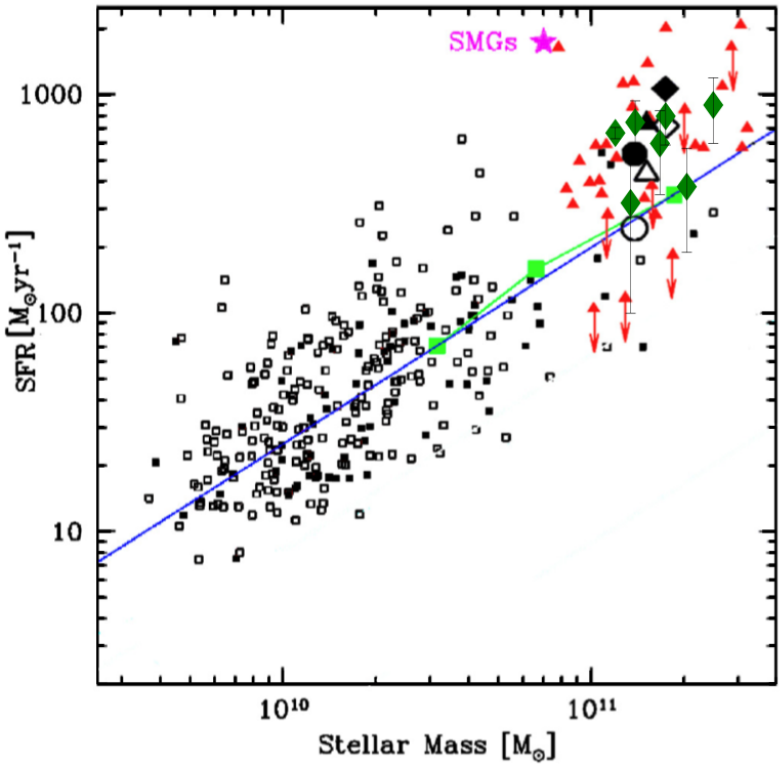

Figure 4.5 adapted from Figure 6 of Fiolet et al. [2009]. Our sample is represented by filled green diamonds. Their x error bars have been suppressed for clarity as we only have order of magnitude stellar mass estimates. Red triangles represent the z∼2 sources presented by Fiolet et al. [2009], Large black symbols represent stacked subsets of the Fiolet sample, small black symbols represent z∼2 sources from Daddi et al. [2007], and the magenta star shows a representative high z submillimeter galaxy. Green squares trace the average trend in GOODS-N.

sources with high [CII]/FIR ratios. For example, H-ATLAS SDP 81 [Valtchanov et al., 2011], at z∼2.3 and the nearby spiral galaxy M51 [Nikola et al., 2001], both show [CII]/FIR∼0.01. Spatially resolved studies of star forming regions in M33 show [CII]/FIR luminosity ratios ranging from 0.01 up to 0.034 as well [Mookerjea et al., 2011]. Assuming the [CII] and FIR arise in PDRs, [CII]/FIR∼1% indicates G∼100 so that the star formation regions in our sources must be very extended [Stacey et al., 2010b]. There are, however, hints that other mechanisms may sometimes contribute to [CII] emission. Several resolved regions of Stefan's

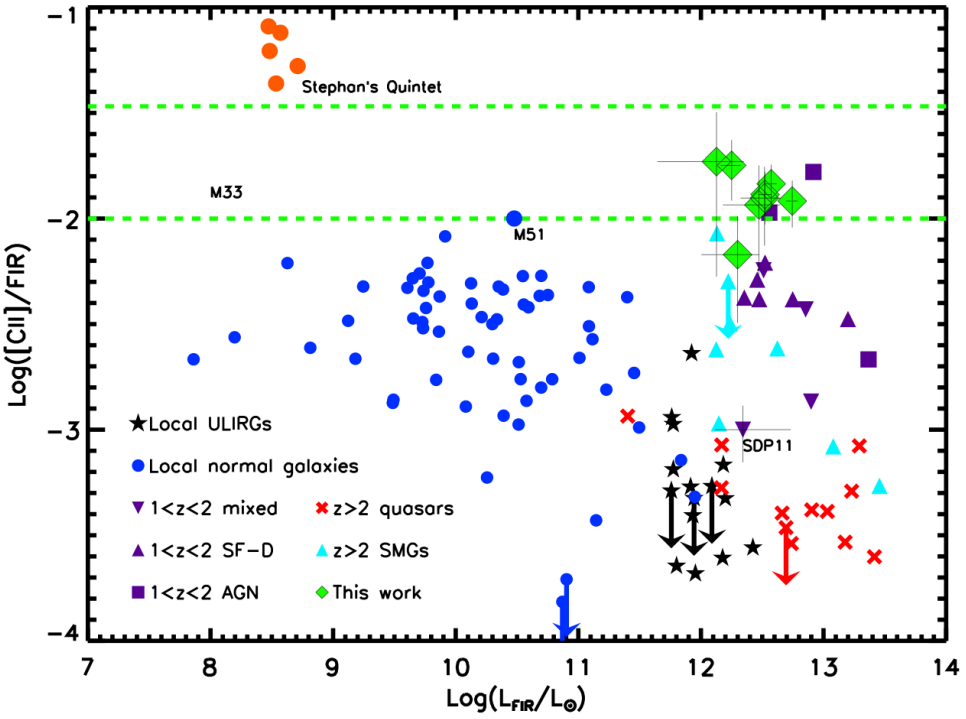

Figure 4.6 [CII]/FIR vs. L_{FIR}. Our SF-D sources are shown as green diamonds with error bars. For comparison we have also included local normal sources [Malhotra et al., 2001], local ULIRGs [Luhman et al., 2003], shock affected regions from Stephan's Quintet [Appleton et al., 2013], 1<z<2 sources from Stacey et al. [2010b] (updated by Hailey-Dunsheath et al. [2014],) and several high redshift SMGs and QSOs [Pety et al., 2004, Marsden et al., 2005, Maiolino et al., 2005, 2009, Ivison et al., 2010, Valtchanov et al., 2011, De Breuck et al., 2011, Swinbank et al., 2012, Wagg et al., 2012, Gallerani et al., 2012, Venemans et al., 2012, Willott et al., 2013, Wang et al., 2013, Riechers et al., 2013]. We also note the local source M51 [Nikola et al., 2001], the z=1.786 source SDP11 [Ferkinhoff et al., 2014], and the ratios spanned by star forming regions within M33 [Mookerjea et al., 2011].

Quintet, for instance, have extremely high [CII]/FIR ratios as a result of shocked PDRs [Appleton et al., 2013].

Another useful diagnostic is the 60/100 μm FIR flux ratio: greater line deficits as well as higher [OI]/[CII] ratios correlate with warmer FIR colors [Malhotra et al., 2001, Díaz-Santos et al., 2013]. From Figure 4.7 we see that our high-z sample spans essentially the full range in FIR color that star form-

ing HII galaxies do, with modest [OI]/[CII] ratios similar to cool star forming galaxies. Although our sources show enhanced [CII] emission relative to L_{FIR}, they have proportionally enhanced [OI] 63 μm emission as well. The exception is SMM J03 which lies to the right, with a hotter FIR temperature and decreased [OI] relative to [CII]. The [OI]/FIR ratios for our sample, plotted in Figure 4.8, are similar to those seen in the SMG sample by Coppin et al. [2012].

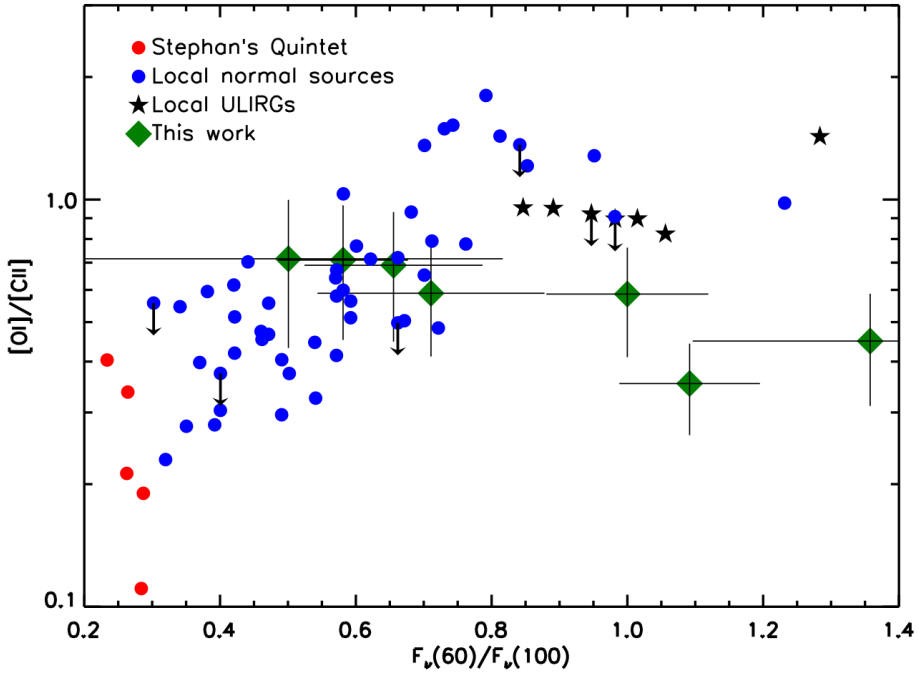

Figure 4.7 [OI] 63 μm/[CII] line flux ratio as a function of the 60 to 100 μm color for a sample of nearby galaxies [blue circles, Malhotra et al., 2001], local ULIRGs [stars Luhman et al., 2003], and our sources (green diamonds). Local ULIRGs tend to have high [OI]/[CII] ratios and warmer dust temperatures. Most of our sources are similar to local normal sources, three of them (MIPS 22530, SMM J03, and SDSS J12,) however, have [OI]/[CII] ratios characteristic of normal galaxies, but warm dust temperatures like local ULIRGs.

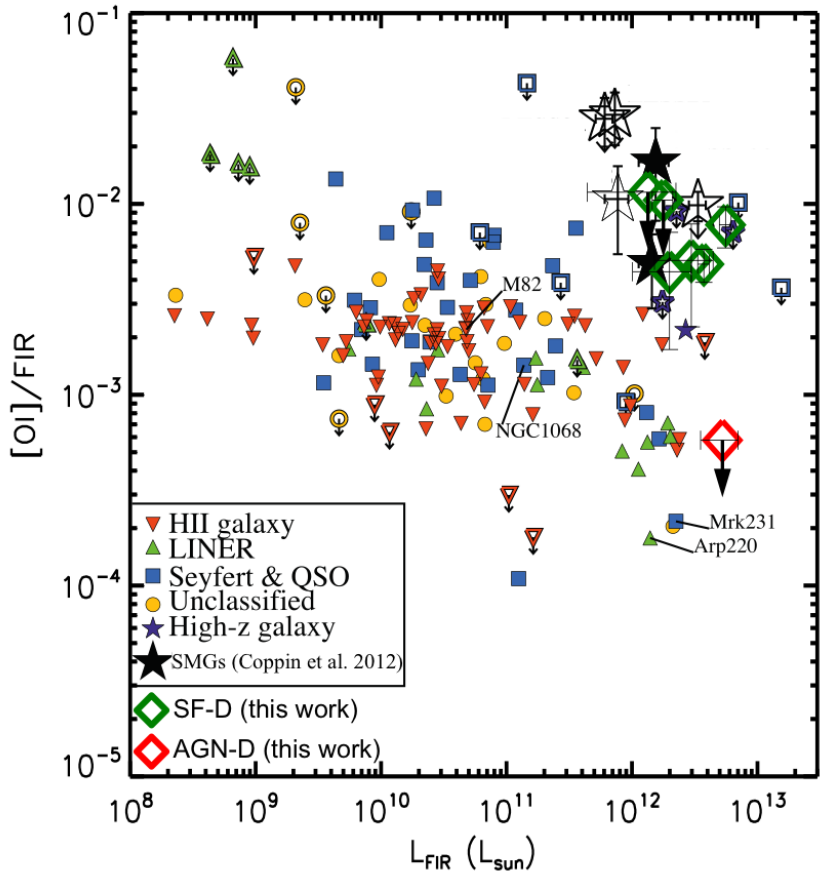

Figure 4.8 Figure adapted from Figure 3 of *Herschel-PACS observations of [OI]63 μm towards submillimetre galaxies at z$\sim$1* Coppin et al. [2012]. Diamonds indicate sources from this work, other symbols from Coppin et al. [2012] and references therein [Graciá-Carpio et al., 2011, Colbert et al., 1999, Malhotra et al., 2001, Negishi et al., 2001, Luhman et al., 2003, Dale et al., 2004, Brauher et al., 2008, Valtchanov et al., 2011, Sturm et al., 2010, Fischer et al., 2010]. Note that Coppin et al. [2012] define L_{FIR} to correspond to 40-500 μm, so we have divided their source luminosities by 1.5 to adjust to our definition of L_{FIR}

4.4.4 PAHs

PAHs are the main source of photo-ejected electrons for neutral PDR gas heating [Weingartner and Draine, 2001]. As a simple diagnostic of heating (traced by PAHs) vs. cooling (traced by [CII]), the ratio of [CII] to PAH emission is of interest much in the same way as the [CII]/FIR ratio. The PAH features in several of

our sources have been examined in other works, however, PAH fluxes are sensitive to the fitting method used. Therefore, in order to obtain a uniform data set in sources for which MIR IRS spectra are available, we fit the spectra ourselves using PAHFIT [Smith et al., 2007]. The fitted spectra are shown in Figure 4.9 and the fluxes are listed in Table 4.4. Most of the PAH spectra were acquired through the Cornell AtlaS of Spitzer/IRS Sources (CASSIS)[6] version 4 using the optimal extraction for point sources. Since MIR spectra contain overlapping PAH and silicate features, it is difficult to independently estimate uncertainties. To do so, we fit each spectrum repeatedly, adding a Gaussian distributed random error to each spectral data point in proportion to each point's error bar. We fit each spectrum over a hundred times and report the mean PAH fluxes and their standard deviations.

To capture the entire PAH spectrum and directly calculate total PAH emission would require observing the full 5-38 μm spectrum covered by the short-low (SL) and long-low (LL) IRS modules. Our sources are all covered only by the LL module, which at z$\sim$1.8 samples wavelengths 5-14 μm. Although this range misses several PAH features, based on Figure 6d in Croxall et al. [2012], we can estimate the total PAH emission based on the 11.2 and 7.7 μm features:

$$PAH_{tot} \approx \frac{8.47(PAH_{11.2})^2}{1.73PAH_{11.2} - 0.197PAH_{7.7}}. \tag{4.3}$$

This PAH estimator relies on the fact that the 7.7 μm feature is representative of the ionized PAH species, and 11.2 μm of neutral PAH species. The strength of ionized vs. neutral PAHs can vary depending on the ambient radiation field.

[6]The Cornell Atlas of Spitzer/IRS Sources (CASSIS) is a product of the Infrared Science Center at Cornell University, supported by NASA and JPL.

The flux ratio of ionized to neutral PAH species is correlated with the intensity of radiation fields, and presence of AGN on a galactic scale. Smith et al. [2007] found that star forming galaxies tend to have 7.7/11.2$\gtrsim$4 while AGN can have much smaller ratios. By this metric all of our sources with reliable PAH estimates would qualify as star forming with the possible exception of SDSS J12 (which is by no means discrepant from a star forming PAH ratio.) Equation 4.3 has only been calibrated over a modest range in the 7.7/11.2 PAH flux ratio, roughly 2.5 to 5. Beyond these bounds, it is unlikely to provide a good estimate. Therefore for SWIRE 3-14 which has a very high 7.7/11.2 PAH ratio, we only consider a lower limit to the total PAH flux by adding up the flux contained in PAH features between 6.2 and 11.2 μm. In Figure 4.10 we plot the [CII]/PAH$_{tot}$ ratio with respect to the FIR color and compare to the sub-galactic sample of star forming regions from Croxall et al. [2012]. Our sources demonstrate a [CII] excess with respect to PAH emission compared to the sub-galactic local star forming regions. We have also revisited the SF-D sources with available PAH spectra from Stacey et al. [2010b] and included their [CII]/PAH$_{tot}$ values, all of which span a similar range. It is worth noting that the AGN-D and mixed systems from Stacey et al. [2010b] for which we have IRS spectra, including IRAS F10026, PG 1206, and 3C 368 (reclassified as AGN-D by Hailey-Dunsheath et al. [2014]) show no evidence of PAH emission despite having detectable [CII] emission.

Table 4.4 PAH features.

	PAH Flux (10^{-18} W m^{-2})				(Eq. 4.3)			
Source	6.2 μm	7.7 μm	8.6 μm	11.2 μm	PAH$_{tot}$	7.7/11.2	[CII]/PAH$_{tot}$	Ref. / AORkey
MIPS 22530	8.6±1.7	23.8±2.3	4.8±1.9	6.0±2.7	53.6±6.1	4.0±1.9	0.17±0.04	AOR:11865856, 23632896
SWIRE 3-9	6.1±1.3	40.6±4.8	3.9±2.4	8.0±2.4	92±17	5.1±1.6	0.07±0.02	AOR:17414656
SWIRE 3-14	6.5±1.1	34.7±2.8	7.9±1.2	4.61±0.90	>53.6[1]	7.5±1.6	<0.044	AOR:17415424
SWIRE 3-18	6.9±3.2	22.4±5.4	4.5±2.2	6.0±2.7	51±11	3.7±1.9	0.14±0.04	AOR:17416960
SWIRE 4-5	4.15±0.28	13.240±0.076	3.59±0.47	2.39±0.47	31.6±4.0	5.5±1.1	0.14±0.04	[Fiolet et al., 2010]
SWIRE 4-15	5.48±0.46	15.9±1.4	3.26±0.63	4.53±0.67	36.8±2.8	3.52±0.60	0.14±0.04	[Fiolet et al., 2010]
SDSS J12	8.54±0.47	17.33±0.63	4.90±0.37	6.14±0.67	44.2±2.6	2.83±0.32	0.13±0.03	[Rujopakarn et al., 2012]
(Stacey et al. 2010) sources:								
SMM J22471	12.9±1.8	44.6±3.8	9.7±2.7	13.6±4.7	106±15	3.3±1.2	0.09±0.02	AOR:16175616
SMM J12	12.0±1.8	54.1±2.7	7.8±2.6	9.0±2.6	139±49	6.0±1.8	0.05±0.02	[Pope et al., 2008]
MIPS J142824	25.1±3.3	111±11	25.4±6.9	23.2±5.6	249±32	4.8±1.3	0.08±0.02	AOR:12513536
SWIRE L25	5.0±1.1	13.3±2.0	3.6±2.0	4.2±2.1	32.1±7.4	3.2±1.6	0.05±0.02	[Fiolet et al., 2010]
SWIRE L17	2.95±0.37	14.9±1.8	3.62±0.64	2.84±0.79	34.2±7.1	5.2±1.6	0.08±0.02	[Fiolet et al., 2010]

Note. — AOR refers to AORkey codes used to acquire spectra from CASSIS [Lebouteiller et al., 2011]. References refer to publications of PAH spectra. For these published spectra electronic copies of the data were acquired through private communication with publication authors. [1] lower limit set by total of 6.2, 7.7, 8.6, and 11.2 μm features.

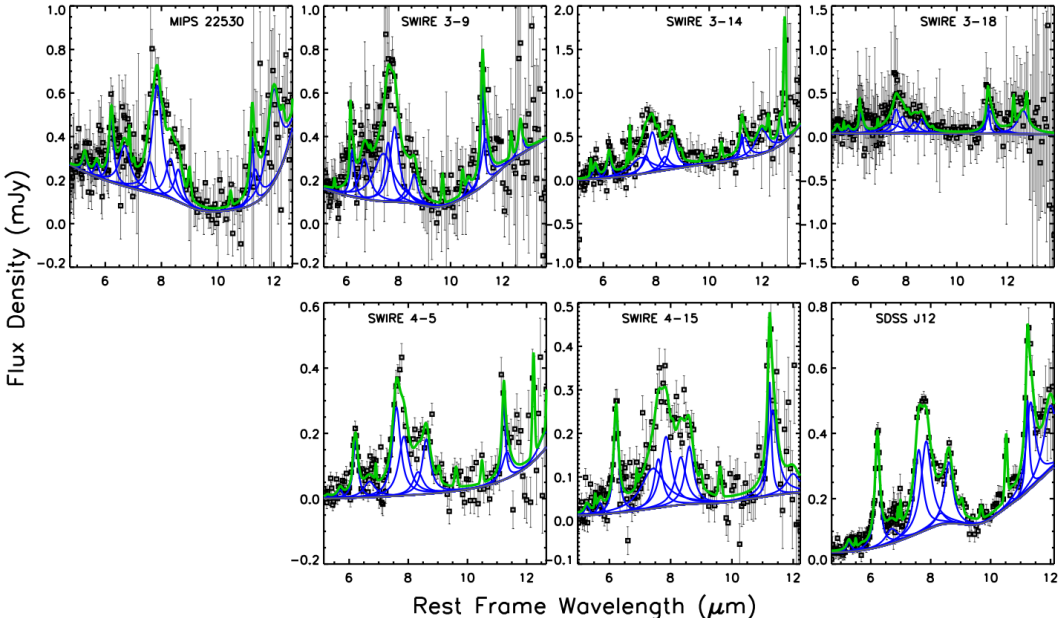

Figure 4.9 MIR IRS spectra fitted with PAHFIT [Smith et al., 2007]. The green curve is the overall fit, blue curves are PAH contributions, and the underlying gray curve is the continuum fit by stellar and dust contributions. Sources of PAH spectra are noted in Table 4.4.

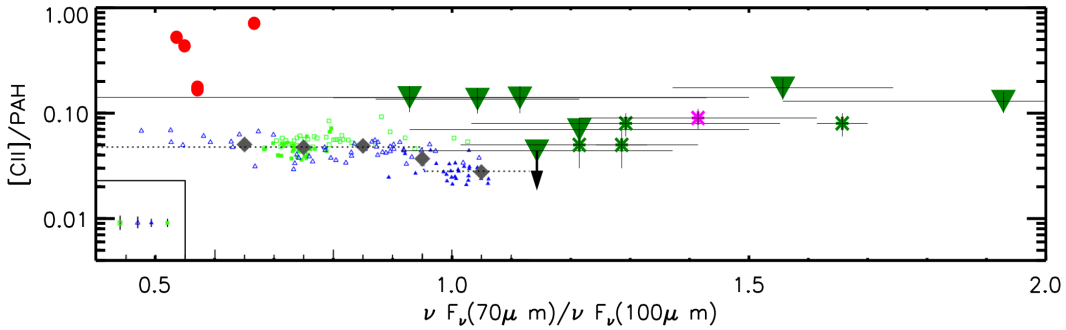

Figure 4.10 Figure adapted from Figure 8 of Croxall et al. [2012]. [CII]/PAH$_{tot}$ vs. FIR color. Our sources (large green upside down filled triangles) are plotted against sub-galactic star forming regions in NGC 1097 (light blue triangles) and NGC 4559 (light green squares). Filled blue triangles and green squares are those regions for which full SL+LL IRS spectra were used to directly determine PAH$_{tot}$ and empty triangles are regions for which only the SL or LL module was available and the total PAH emission was estimated by another method (see Croxall et al. [2012].) The inset shows typical error bars for these regions. Asterisks denote sources from Stacey et al. [2010b], green are star formation dominant, magenta represents the poorly characterized system SMM J22471. We have also plotted the regions from Stephan's Quintet reported by Appleton et al. [2013] as red filled circles.

4.4.5 PDRs

We use the PDR toolkit [Pound and Wolfire, 2008, Kaufman et al., 2006] to analyze our source properties within a PDR paradigm. The PDR models provide estimates of several neutral and molecular gas cooling lines over a large phase space of density and FUV irradiation. For the majority of our sources the useful constraints on PDR characteristics are based on the [OI]/[CII] ratio, which rises with increasing density and G_0, and either [CII]/FIR or ([CII]+[OI])/FIR which characterizes the gas heating efficiency. The output of the PDR models is the intrinsic line emission from the PDR. Before we can interpret the model outputs in terms of physical conditions we need to translate between the observed and intrinsic line emission. As a simple model, we assume a dual-slab molecular cloud geometry in which both faces of externally irradiated molecular clouds harbor PDRs. Cloud-to-cloud velocity variation generally allows us to observe emission from multiple clumps without optical depth effects. The [OI] line, however, is often optically thick on the surfaces of individual molecular clouds [cf. Stacey et al., 1983], so we will only detect [OI] emission from the front surfaces of clouds. To account for this, we multiply the observed [OI] flux by two to match the plane parallel models in the PDR toolkit. Geometry and velocity dispersion may vary, but results from this simple approximation have generally been consistent with observations on a galactic scale [Malhotra et al., 2001, Vasta et al., 2010]. [CII], as previously mentioned, arises in both neutral and ionized gas. The fraction arising from PDRs can vary, but in general it is $\sim$70%, and we take that as our intrinsic PDR fraction. Table 4.5 gives the PDR parameters required by fitted models discussed below.

4.4.6 Individual sources

Many of our sources demonstrate strong [CII] emission. Most have [CII]/FIR in excess of 1%, and of those for which we have an IRS spectrum, most have [CII]/PAH ratios exceeding the highest sub-galactic regions in normal local galaxies. While the [CII] emission in normal galaxies is generally explained in a PDR paradigm, the unusual nature of these diagnostics in our sample may hint at additional sources of [CII] in a few cases. Below we discuss the nature of our sample on a source by source basis.

MIPS 22530 Our [CII] and [OI] detections of this source are both somewhat blueward of the optical redshift: [CII] by $\sim$100 km s^{-1} and [OI] by $\sim$200 km s^{-1}. MIPS 22530 is detected in all 3 MIPS bands and all three SPIRE bands, providing a well determined FIR SED. Its SED-derived luminosity is L_{FIR}=(5.6$\pm$0.6)$\times10^{12}L_{\odot}$. The ratio of the two fine structure lines along with the 60/100 μm flux ratio puts this source generally in the same league as normal local galaxies shown in Figure 4.7, except with a slightly bluer infrared SED, possibly indicating especially strong or recent star formation. The fine structure lines in this source can be well described with a PDR model. Figure 4.11 shows the overlapping constraints placed on our PDR model from the [OI]/[CII] ratio and ([OI]+[CII])/FIR. As is generally the case, the PDR model for MIPS 22530 shows two regions of allowed phase space in density and G_0, one with modest density and modest G_0 and one with high density and low G_0. We favor the former solution as the density is more representative of a mixed phase galaxy average, and as we show in Section 4.5, a very low G_0 value is difficult to reconcile with the large luminosities of our systems. The favored model phase space constrains density, n$\sim10^{3.5}$ and UV flux $G_0\sim10^{2.25}$.

SWIRE 3-9 Both [CII] and [OI] are strongly detected in this source, although there appears to be a slight offset between the line centers, likely due to calibration error in the [CII] observation. Given the greater velocity resolution in the PACS [OI] spectrum, we adopt its indicated redshift of z=1.732±0.003 with error bars encompassing our [CII] detection. Both of the lines are significantly redward (∼2500km s^{-1}) of the PAH-derived redshift, however uncertainties of this magnitude are not unexpected in redshifts determined from PAH spectra with low signal to noise. The PAH features are also well fit using our adopted redshift and the fitting quality is nearly equivalent to fits using the indicated PAH redshift. The fine structure lines are again consistent with a star formation powered PDR source. Shown in Figure 4.11, [CII], [OI], and the FIR continuum constrain the PDR density, n∼$10^{3.5}$ and UV flux G_0∼$10^{2.5}$.

SWIRE 3-14 Our [CII] line, detected at z=1.7795, is consistent with PAH observations. Our PACS observations of this source tentatively detect (∼3σ) the [OI] line at the [CII] velocity. The FIR luminosity in this source is again based only on a few photometric observations including SPIRE measurements with considerable noise giving L_{FIR}=(2±1)×$10^{12} L_{\odot}$. The fine structure lines and continuum are consistent with a star formation powered PDR source. As shown in Figure 4.11, [CII], [OI], and the FIR continuum constrain the PDR density, n∼$10^{3.25}$ and UV flux G_0∼$10^{2.75}$.

SWIRE 3-18 is a strong [CII] emitter with [CII]/FIR=0.012±0.005. We have compiled SPIRE photometry from HerMES to determine L_{FIR}=(3.3 ± 1.2)×$10^{12} L_{\odot}$, and it has a cool dust temperature with (S_{70}/S_{100})=0.78±0.22, similar to SWIRE 4-5 and 4-15. This is consistent with previous claims that it is a SF-D source. Without an [OI] observation we cannot fully disentangle density

and G_0 degeneracies in PDR parameters, but assuming a density n$\sim 10^{3-4}$ cm^{-3} we find $G_0 \sim 10^{1.9-2.9}$. (Figure 4.11.)

SMM J03 has warm dust colors as well as very strong [CII]/FIR ratio. Our PACS observations strongly detect [OI] 63 μm with a flux of $(5.6 \pm 0.8) \times 10^{-18}$ W m^{-2}. In addition, CO 3$\rightarrow$2 has been detected in this source, $F_{CO(3\rightarrow 2)}$=1.55×10^{-20} W m^{-2} (Steve Hailey-Dunsheath, private communication.) Figure 4.11 shows our PDR model for the fine structure lines ([CII], [OI]63), FIR continuum, and CO emission. Our PACS photometry along with SCUBA data [Kovács et al., 2006] provide a well constrained SED with L_{FIR}=$(3.74 \pm 0.4) \times 10^{12} L_{\odot}$. Our observations are nearly consistent with a standard PDR model accounting for 70% of the observed [CII]. However, the fraction of [CII] from PDRs varies significantly on at least sub-galactic scales, and Croxall et al. [2012] show that it is anti-correlated with the FIR 70/100 μm flux ratio: hotter dust sources tend to have smaller fractions of [CII] arising in PDRs. Attributing a slightly smaller fraction of [CII] to PDRs ($\sim$50%) allows a PDR solution truly consistent within the 1σ error bounds of our many line ratios, and is justified given the high 60/100 μm flux ratio and the somewhat low [OI]/[CII] ratio of this source.

A full analysis uniting the neutral and ionized gas emission is beyond the scope of this paper, however SMM J03 does show some signs of AGN presence and large ionized gas reserves. The rest frame optical lines and their ratios, Hα, Hβ, NII, and OIII 5007Å, indicate this is a Seyfert-2 type galaxy [Swinbank et al., 2004, Takata et al., 2006] (though Takata et al. [2006] ultimately suggest star formation super-wind induced shocks as the source of ionized gas.) We conclude $\sim$50% of the [CII] in this source comes from star formation powered PDRs with a modest UV intensity, $G_0 \sim 10^{2.75}$, and density n$\sim 10^{3.5}$cm^{-3}.

SWIRE 4-5 The [CII] line is detected at z=1.756, consistent with the previous PAH determined redshift. Available IR photometry for this source is limited to four data points including 24μm, 1200μm, and the 250 and 350μm SPIRE measurements. The source is in the HerMES fields, but not detected in the default catalogs. We independently extracted fluxes from the SPIRE images using the [CII] position as a prior. Moderate source blending is evident near this source in the SPIRE images, and this limits the precision of our fluxes. We estimate the FIR luminosity to be (1.3$\pm$0.9)$\times$ $10^{12} L_{\odot}$. With [CII]/FIR=0.019$\pm$0.013, this is potentially one of the most exceptional [CII] emitters known. The confused SPIRE photometry on this source dominates the uncertainty on the [CII]/FIR ratio. The 60/100 μm flux ratio of this source, on the other hand, is completely consistent with local sources, and is in fact the lowest 60/100 μm flux ratio in our sample. The [OI] spectrum shows a marginal detection. The line is consistent with the [CII] velocity and a normal local [CII]/[OI] ratio, however the spectrum is taken from an off center PACS pixel corresponding to 9.3 arc seconds off the nominal position. We present it here as a tentative detection.

It is reasonable to conclude that the [CII] and [OI] are coming from the same region in this source, but their particularly high fluxes relative to the FIR make it difficult to rectify with a classic PDR model in which UV photons dominate the gas heating. In table 4.5 and Figure 4.11 we show that assuming a classic PDR model implies especially low FUV fields, $G_0 \sim 10^{1.75}$ and high densities, n$\sim 10^{4.25}$. If the marginal [OI] detection is treated only as an upper limit, a larger phase space could explain the observations.

SWIRE 4-15 Our [CII] detection at z=1.8484 is well within the PAH determined redshift range. Herschel SPIRE photometry from HerMES show an

SED dominated by a cool dust component peaking at $\sim$120 μm, further confirming the SF-D nature of the source. Based on HerMES SPIRE data and 1.2 mm MAMBO data [Fiolet et al., 2009] we find L_{FIR}=1.78$\pm$0.33)$\times$ $10^{12} L_{\odot}$. This source is similar to SWIRE 4-5 in both [CII] emission ([CII]/FIR=1.79$\times 10^{-2}$) and FIR color (S_{60}/S_{100}=0.73.) We have a broad line detection in [OI], ($F_{[OI]}$=4.4$\pm$1.1$\times 10^{-18}$ W m^{-2}.) Once again, the [CII]/[OI] ratio is similar to normal galaxies, but a standard PDR paradigm requires low FUV fields and high densities to explain the lines and continuum ($G_0 \sim 10^{1.5}$, n$\sim 10^{4.25}$.)

SDSS J12 This source was observed and detected in [OI] by Sangeeta Malhotra and we add to the discussion our [CII], well constrained FIR photometry from the PEP public data release, and the fitted MIR spectrum. PEP data yields an apparent L_{FIR}=$(3.3 \pm 0.4) \times 10^{12} L_{\odot}$. Accounting for the system magnification, the intrinsic luminosity suggests that SDSS J12 is a relatively modest star forming source in terms of overall luminosity. SDSS J12 has a modestly warm FIR color, S_{60}/S_{100}=1.35, consistent with the suggestion that this source is undergoing particularly intense star formation which would cause increased abundance of hot dust along with ionized gas reserves [Hainline et al., 2009a]. In Figure 4.11 we show that a PDR model with Log(n)$\sim$3.5 and Log(G_0)$\sim$2.5 can explain the [CII] and [OI] emission along with the continuum.

4.5 Discussion

Our source sample is dominated by galaxies powered by star formation which lie along the galaxy main sequence. This is a reflection of our selection bias towards star forming sources with PAH emission. The sample bears out the find-

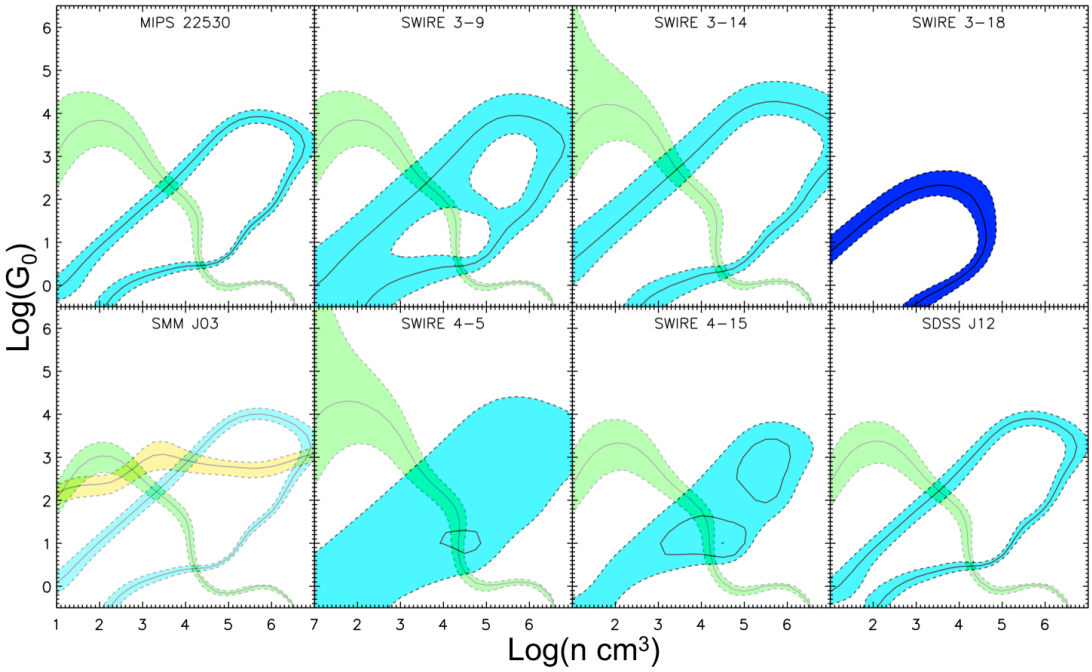

Figure 4.11 PDR diagnostic plots. Colored contours show constraints on n and G_0 based on the following ratios: green [OI]/[CII], cyan ([OI]+[CII])/FIR, blue [CII]/FIR, yellow [OI]/CO(3→2). Solid lines note ratio values and shaded areas represent $\pm 1\sigma$ regions. For consistency in these plots we attribute 70% of observed [CII] to the classic PDR model, although for the bottom row of sources we have reason to believe the true fraction is slightly lower due to enhanced ionized gas emission or additional shocked PDRs (see text.)

ing established by Stacey et al. [2010b] that ultra luminous star forming galaxies at redshifts from 1 to 2 can have efficient [CII] emission unlike local ULIRGs.

Within the PDR paradigm, the relative strengths of fine structure lines such as [CII], [OI], and the FIR continuum characterize the intensity of the local FUV field. Essentially all of the FUV that impinges on neutral gas clouds is absorbed by dust and reradiated in the FIR continuum. Therefore, the observed FIR intensity measures the average FUV field intensity within our telescope beam. The PDR-derived FUV field intensity, (G_0,) and our beam-averaged field intensity are thus related by the source beam filling factor.

Table 4.5 PDR model parameters.

Source	PDR parameters		
	Log(n cm^3)	Log(G_0)	size (kpc)
MIPS 22530	$3.5\pm^{0.3}_{0.4}$	$2.25\pm^{0.3}_{0.4}$	3.0-9.7
SWIRE 3-9	$3.5\pm^{0.4}_{2.5}$	$2.5\pm^{0.8}_{1.1}$	2.0-5.3
SWIRE 3-14	$3.25\pm^{0.2}_{2.25}$	$2.75\pm^{1.2}_{1.1}$	1.5-3.3
SWIRE 3-18	3-4	$2.25\pm^{0.7}_{0.4}$	2.5-7.5
SMM J03	$3.5\pm^{0.1}_{0.4}$	$2.5\pm^{0.2}_{0.2}$	2.2-6.0
SWIRE 4-5	$4.25\pm^{0}_{3.25}$	$1.75\pm^{2.1}_{0.8}$	2.7-8.5
SWIRE 4-15	$4.25\pm^{0.1}_{0.8}$	$1.5\pm^{0.4}_{0.5}$	3.7-13
SDSS J12	$3.5\pm^{0.4}_{0.5}$	$2.25\pm^{0.2}_{0.5}$	2.5-7.5

Note. — The size scale represents the summed areal extent of star formation powered PDRs. It is a representative value only and its range is based on the G_0 value under the separate assumptions of small and large mean free photon paths relative to cloud size as outlined in section 4.5 (and does not account for the uncertainty on G_0). Representative n and G_0 values give the best PDR solution assuming 70% of observed [CII] is due to PDRs except in the case of SMM J03 where we assume 50%. Error ranges are such that 68.27% of the power in the marginalized probability distribution function of each parameter is contained within. We have assumed G_0 >10 as a prior to ignore the low G_0 high density solution which, as discussed in the text, is unrealistic for galaxy averaged properties. In SWIRE 3-18 we lack a useful [OI]/[CII] ratio to constrain density so we have assumed n$\sim10^3$-10^4 cm^{-3}, consistent with other star forming sources at high redshift [Stacey et al., 2010b]. Finally, note that in SWIRE 3-9, 3-14, and 4-5, the large error bars on [OI]/[CII] and the relative insensitivity of that line ratio at low density leads to a lower error bar that encompasses the full low density range of the PDR model.

Wolfire et al. [1990] found that a cloud of size D, and luminosity, L_{IR}, should have an average FUV field given by $G_0 \propto \lambda L_{IR}/D^3$ where λ, the mean free path of a photon, is much smaller than the cloud extent, D; or $G_0 \propto L_{IR}/D^2$ if $\lambda \gtrsim D$. If we use M82 as a model, D$\sim$300 pc [Joy et al., 1987], $G_0\sim$1000 [Lord et al., 1996], $L_{FIR}\sim2.8\times10^{10}L_\odot$ we find that (D/pc)^3 $\sim$0.96 ($L_{FIR}/L_\odot$)/G_0 or (D/pc)^2 $\sim$3.2e-3 ($L_{FIR}/L_\odot$)/G_0. As noted in Table 4.5, we find the spatial extent of star formation in all of our sources is $\gtrsim$2 kpc, implying that star formation is occurring over a large fraction of the galactic disk. Note that a lower G_0 $\sim10^{0.25}$, which often appears as a secondary solution in our PDR models comparing [CII] and [OI]

(see Figure 4.11), would imply spatial scales an order of magnitude larger which is not reasonable, so we take the higher field solution. Our finding of kpc scale star formation is consistent with the recent observations of spatially resolved CO in high redshift sources [Tacconi et al., 2010, Daddi et al., 2010, Ivison et al., 2011, Riechers et al., 2011]. As Tacconi et al. [2010] point out, the large spatial distribution of molecular gas does not necessarily imply a single coherent disk of star formation, but instead is very likely the observation of widely distributed clumps which are not individually resolved, but are all likely undergoing star formation obeying a Schmidt-Kennicutt law.

We have confirmed our previous result that the [CII] deficit is not a ubiquitous phenomenon in star formation powered ULIRGs at redshift 1-2. The combined high [CII] and FIR luminosities can only be fit within the PDR paradigm if the source size is at least several kpc in extent and potentially much larger. This is in sharp contrast with local ULIRGs with their intense, and localized collision induced bursts of star formation. Figure 4.12 presents a cartoon schematic of these different modes of star formation. The [OI] and PAH observations we present here further confirm the PDR interpretation of the [CII] and FIR continuum emission, also confirming the large star formation spatial extent (which was postulated for similar sources in Hailey-Dunsheath et al. [2010] and Stacey et al. [2010b].)

The large spatial scales of star formation are best understood as the expected star formation that results from large and abundant molecular reserves under a Schmidt-Kennicutt law. The large molecular gas aggregation likely results from cold accretion from the cosmic web, not concentration from major mergers, which would produce very intense, but localized star formation sites resulting

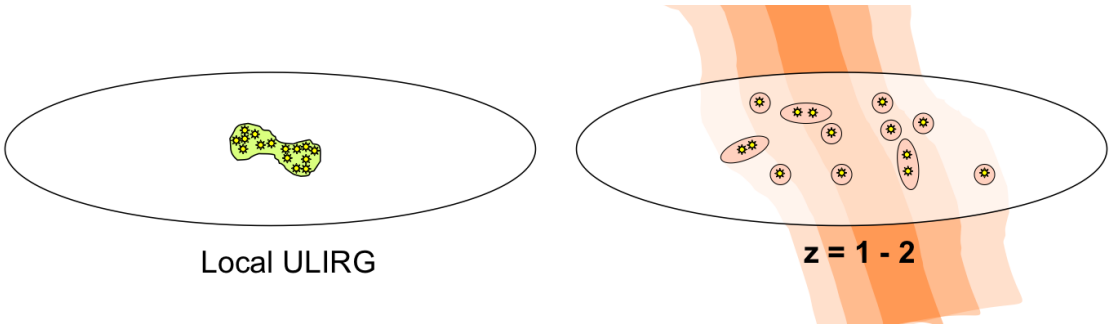

Figure 4.12 A schematic representation of star formation in local ULIRGs (left) vs. star formation powered ULIRGs at z=1-2 (right.) Local ULIRGs may show one or more compact regions of intense star formation activity with strong UV fields and high dust temperatures, often powered by recent galaxy merging. At redshifts 1-2 the modest UV fields discussed here and large observed molecular gas distribution s [Tacconi et al., 2010, Daddi et al., 2010, Ivison et al., 2011, Riechers et al., 2011] indicate more spread out star formation occurring over a significant fraction of the galaxy's area. We suggest that intergalactic gas accretion from the cosmic web (indicated by shaded region) fuels such widespread star formation.

in low [CII]/FIR ratios as seen in local ULIRGs. *Much of the star formation in the epoch of peak star formation, when most of the stars in the Universe formed, resulted from gas accretion from the cosmic web, not merger activity as had previously been supposed.*

The [OI] 63 μm line was detected in the seven sources that were observed with the PACS spectrometer on Herschel. Another set of seven sources also have useful IRS spectra available which we have collected and made use of here to consider their PAH emission. In our sample the PAH features are strong, but [CII] to PAH ratios exceed those of local star formation regions.

This accumulated wealth of data has allowed us an unprecedented look at the nature of these galaxies, and in particular their dominant power sources in the infrared. The standard approach, using classic PDRs to explain the observed emission, can adequately produce the line and continuum emission we

see. In several cases, however, the amount of fine structure line emission we see relative to the FIR continuum is brushing up against the limits of what classic PDRs are capable of. This is most notable in our two sources with the highest [CII]/FIR ratios, SWIRE 4-5 and 4-15, which both demand low UV fields and very extended spatial extent.

In addition to the difficulty in modeling these systems, our sources clearly demonstrate excessive fine structure line emission relative to both FIR continuum and PAH emission compared to most local sources. Our enhanced [CII] ratios are particularly reminiscent of the work by Guillard et al. [2012] and Appleton et al. [2013] on Stephan's Quintet. Their work shows enhanced CO and [CII] emission as a direct result of shock heated gas. In particular, Appleton et al. [2013] finds [CII]/FIR and [CII]/PAH ratios a factor of $\sim$5 higher than we see (as shown in Figures 4.6 and 4.10.) Our sources are not as extreme in these characteristics, but they do stand out from the general population of galaxies, and may represent hybrid systems involving significant contributions from both classic PDRs and shock powered regions.

We have already seen cases where microturbulence contributes significantly to the overall heating budget of various lines on a galaxy-wide scale. In earlier work on NGC 253 and NGC 891 we found that microturbulence was needed in addition to classic PDRs to explain neutral and molecular gas emission [Hailey-Dunsheath et al., 2008, Stacey et al., 2010a, Nikola et al., 2011]. Implicating microturbulence to explain [CII] emission, requires a source of radiation to ionize the carbon. Lesaffre et al. [2013] showed that diffuse, lightly irradiated gas undergoing low velocity shocks can produce significant turbulence which dissipates by heating the gas and powering emission in the primary coolant lines

including [CII]. Furthermore, this turbulent heating does not necessarily imply violent galaxy mergers. Indeed, the low velocity shock models ($\sim$8 km s^{-1}) could contribute significantly and might easily result from star formation feedback processes such as stellar outflow, supernovae, or simple impacting clumps accreting from the intergalactic medium. To characterize the shock properties and the relative contributions from shocked diffuse gas and PDRs would require observation of more emission lines, however, the very high cooling line ratios with respect to FIR and PAHs are good indications that additional sources of heating, such as microturbulence, are contributing to [CII] emission in high redshift star formation powered galaxies.

4.6 Conclusions

We have detected eight new z=1-2 sources in the [CII] 157.7 μm line. Seven of them were also observed in the [OI] 63 μm line. Far infrared photometry, made available through our Herschel program, HerMES, and PEP, has allowed us to establish SEDs and reliable FIR luminosity estimates.

In general we have found that the relative [CII] and [OI] emission is comparable to local star forming systems and can largely be explained with classic PDR models. There is, however, very strong [CII] relative to both FIR continuum and PAH emission. Seven of our eight sources exhibit [CII]/FIR$>10^{-2}$, and five exhibit [CII]/PAH$_{tot}$ $>$0.1.

We have used [CII]/FIR to determine G_0 based on a PDR paradigm, and with L_{FIR} we determine the PDR filling factor in our beam. The extent of our star forming regions are very large, unlike local ULIRGs. Extended, moderate

intensity, star formation dominates their energetics, likely stimulated by large molecular gas reservoirs, accreted from the cosmic web. This picture leads us to a paradigm shift: much of the star formation at z$\sim$1-2 is not driven by major mergers, but instead by cold flow accretion. Although there are several examples of major mergers in the early Universe, cold flow accretion fueled galaxies abound as well. Our [OI] and PAH detections further confirm this interpretation of [CII].

While the [CII] and [OI] largely arise from classic PDRs, we must qualify the standard PDR paradigm with the caveat that a portion of the exceptional fine structure line emission we observe here may be powered by other heating mechanisms in addition to classic PDRs. In SMM J03 there is probably enhanced contribution to [CII] from ionized gas ($\sim$50%). In SWIRE 4-5 and SWIRE 4-15, the high [CII] ratios are approaching the limit of what PDRs can provide, and their FIR dust temperatures are low suggesting a heating mechanism which bypasses the UV dust absorption mechanism. This is consistent with a low velocity shocked diffuse gas component as modeled by Lesaffre et al. [2013] and invoked by Appleton et al. [2013] to explain high [CII] ratios in Stephan's Quintet.

The [CII] line remains a useful probe in the z$>$1 Universe. It had been presumed that large-scale mergers dominated the star formation in this epoch which would lead to compact and intense star formation regions with relatively weak [CII] emission like local ULIRG galaxies. The discovery of very extended [CII] emission is a key element of the new paradigm that cold accretion from the cosmic web fuels very high gas surface densities leading to enhanced, wide-scale star formation following a Schmidt-Kennicutt law.

With the observational avenues that have opened in the last few years, we

are now able to acquire more diversity of data and work with better refined models than ever before. This presents us the welcome challenge of transitioning from studying broad brush characterization of star formation in general to examining individual sources. Going forward, the [CII] line, [OI], PAHs, and other multiwavelength data will allow us an exceptional look at the dynamics of individual galaxies, building on the picture presented here, and allowing a much refined and detailed model of star formation and galaxy evolution.

CHAPTER 5

OVERVIEW, CONCLUSIONS, AND FUTURE WORK

In this thesis I have presented work concerning the evolution of galaxies over the last $\sim$10 billion years of the Universe's history. Insights gleaned on this subject in the last decade have been possible in large part due to the multi-wavelength, broad and deep surveys of distant galaxies enabling us to better characterize many stages of star and galaxy formation over cosmic time. Technological advances allowing observation in the sub-millimeter have been crucial to revealing the nature of infrared bright galaxies and dust-embedded regions at redshifts z$\sim$1-2 where rest frame optical and UV light suffers extremely high extinction.

Far infrared / sub-millimeter observations have long been anticipated as a promising avenue for observing high-z sources. Redshifted lines observed in these bands are very strong, optically thin, nearly unaffected by extinction, and often the primary coolant lines for the emission region and therefore useful diagnostic probes of the physical conditions within the emitting medium. The FIR continuum arises from warm dust heated by star light and/or short wavelength radiation from AGN. In dusty star forming galaxies the FIR continuum luminosity often exceeds the optical luminosity. In the most extreme examples, nearly all of the starlight is reprocessed by dust and emitted in the FIR bands.

The launch of Herschel in 2009 dramatically expanded the opportunity to observe in the sub-millimeter. Its ability to quickly map regions photometrically across a large portion of the FIR / sub-mm regime (70 - 500 μm in PACS and SPIRE) in any region of the sky has allowed ambitious surveys to study the early Universe in finer detail than ever before. Deep integrations in the HerMES and

PEP projects have probed down to confusion limited scales with SPIRE, and resolved much of the cosmic infrared background (∼50%) with PACS in the form of infrared galaxies [Oliver et al., 2010, Berta et al., 2010]. These surveys have also yielded new characterizations of galaxy luminosity functions and star formation histories via the L_{FIR}-SFR correlation.

The SDSS is an example of one of the broadest surveys in the history of astronomy. Its survey footprint (as of DR10) covers ∼35% of the sky [1]. Not only has it provided photometry on ∼90% of galaxies down to r magnitude 21.12, allowing broad brush categorization of most large galaxies in the local Universe, its extensive spectroscopic catalogs of galaxies allows an unprecedented statistical look at properties like extinction, star formation, metallicity, and even AGN presence. The SDSS represents one of the most significant steps in the last decade of characterizing the nearby Universe.

The SDSS has also detected several objects at higher redshifts (including a handful of QSOs at z∼6 [Fan et al., 2006, Jiang et al., 2006, 2008].) While these observations highlight some very interesting objects, the SDSS data by itself is not especially useful for characterizing the early Universe as a whole. High redshift objects spotted in SDSS tend to be the many-sigma stand outs which represent the most extreme systems. Furthermore, at a redshift ∼2, the red end of SDSS spectral coverage in the near infrared corresponds to the rest frame near UV, which is highly susceptible to dust extinction.

Again, the far infrared / sub-millimeter regime offers new access to galaxy properties through several extremely bright fine structure lines which can directly reveal the dynamics of dusty ISMs in high redshift galaxies. ZEUS, which

[1] http://www.sdss3.org/dr9/

saw first light in April 2006 [Stacey et al., 2007] is ideally suited for studying broad extragalactic fine structure lines, and in particular [CII] in galaxies at z=1-2. Its spectral resolution is well matched to their velocity-broadened line widths. Even with the obscuring effects of the atmosphere, the sensitivity to broad emission lines of ZEUS on the CSO surpasses that of SPIRE.[2] The early ZEUS observations of [CII] in galaxies at z=1-2 were formative in determining the nature of these sources, and ultimately led to the emerging paradigm shift that moderate intensity, spatially extended star formation is responsible for the much of the star formation in ULIRGs at high z. Not all star forming systems contain intense, localized star formation fueled by major mergers as is the case in many local ULIRGs [Stacey et al., 2010b]. The Herschel PACS spectrometer complements the capabilities of ZEUS. ZEUS readily detects [CII] at redshifts 1-2 while PACS can detect fine structure lines from O and O^{++} from the same systems. This combination of lines tightly constrains the PDR media gas density and FUV field strength and, through the O^{++} lines, indicates the number of upper main sequence stars capable of emitting the required strongly ionizing radiation.

The synergy between these instruments and surveys has allowed an unprecedented look at galaxy evolution and the underlying physics that shape them. Below I describe my conclusions based on this wealth of data, and also present near term extensions of these works which spring directly and build upon the work discussed. In section 5.3.1 I discuss future work that extends this science to higher redshifts in an attempt to understand galaxy evolution during the epoch of galaxy birth.

[2]In good weather, at 434 μm ZEUS on the CSO obtains a 5σ, 1 hour line sensitivity limit $\sim 2\times10^{-18}\mathrm{W/m^{-2}}$ for a line contained within two spectral bins (556 km/s) [e.g. Ferkinhoff et al., 2010, 2011]. The SPIRE instrument has a sensitivity of $13\times10^{-18}\mathrm{W/m^{-2}}$ (SPIRE observers manual).

5.1 The Deep SPIRE HerMES Survey: Spectral Energy Distributions and their Astrophysical Indications at High Redshift

We examined photometric Herschel observations of the GOODS-N and Lockman-N fields. SPIRE observations of both fields come from the HerMES project, and in Lockman-N we include PACS data from the PEP survey. These fields formed the deepest blind observations of early Herschel operation, and as such, were proving grounds for the true capability of Herschel to investigate the early Universe.

At the depths of these surveys, source confusion becomes a major issue, especially at the two longest SPIRE wavelengths, 350 and 500 μm. We found that a large fraction of sources detected by automated algorithms were in fact blended combinations of sources, as evident by their extended morphology, the existence of multiple underlying sources at shorter wavelengths, and SEDs that show emission uncharacteristic of a FIR dust peak. This is not surprising since the sources we extracted from initial HerMES catalogs had 500 μm flux densities ranging from 11 to 25 mJy, while Nguyen et al. [2010] characterized the 500 μm confusion noise as 6.8 mJy, implying that our sources are right on the edge of identifiability, extremely subject to the chance arrangement of nearby sources. At 350 μm the situation is similar - our sources of interest had flux densities ranging from 10 to 32 mJy with confusion noise estimated as 6.3 mJy, while at 250 μm the confusion noise marginally decreases to 5.8 mJy. Surveys probing down to or beyond the confusion limit can still be useful probes of cosmology in a statistical sense, (P(D) analysis, for instance allows source count statistics

below the confusion limit [Patanchon et al., 2009],) but to examine individual sources, it is crucial that one source be identifiable with one specific flux.

To this end, we established a metric, the 'purity index', which allowed us to reliably identify well isolated sources based on the underlying flux map at another wavelength with finer spatial resolution. The metric is simple to measure given a map of interest and another map with finer resolution, so invoking it is not computationally burdensome and it could be easily adapted to future confusion-limited surveys at other wavelengths. The Spitzer 24 μm MIPS resolution (5.9″), is fine enough that it can often pull apart sources that appear blended in SPIRE or PACS. At the same time, fluxes at 24 μm are correlated with longer wavelengths, allowing some predictive power over the relative contributions of different 24 μm sources to FIR intensity maps. We demonstrated the efficacy of the metric by selecting a set of 21 sources spanning redshifts 0.5-3 based on their high purity indices at PACS and SPIRE wavelengths. The compiled SEDs of these sources all included broad, single peaked FIR emission characteristic of locally observed galaxies - unlike randomly selected sources from automated detection algorithms which often resulted in 'broken' SEDs with multiple local peaks in the FIR.

As we concluded in Chapter 2, Our source SEDs were generally consistent with star forming galaxies which we fit using templates based on local galaxies in the [Siebenmorgen and Krügel, 2007] library. At the time of publication we used a straight forward fitting method that simply compared the absolute luminosity densities of the templates with the observations, as advocated by Siebenmorgen and Krügel [2007]. Retrospectively, we note that several of the fits were less than ideal. The sources noted as LN (D), (F), (G), (H), GOODS-N

(B), (C), (G), and (d) all show SEDs that appear physically plausible, but demonstrate excessive emission at $\gtrsim$100 μm over the best-fit template. In light of the picture that has emerged over the last several years this sub-mm excess is easily understood. As we addressed specifically in Section 4.4.2, in the S&K SED templates (based on local star forming galaxies,) there is a clear correlation between increasing dust temperature and increasing absolute luminosity. In the local Universe this is borne out by observations - having a very luminous star formation powered galaxy requires very intense localized star formation which increases dust temperatures and shifts the FIR dust peak to shorter wavelengths. At higher redshifts, we see numerous examples, the cited LN and GOODS-N sources being several, in which this is not the case - leading us to conclude that extended, modest intensity star formation is capable of powering ULIRGs with relatively low dust temperatures. The SED fits from this chapter that show submillimeter excesses can benefit from the scaling factor we introduce in chapter 4 which allows us to generate SED templates with the long wavelength FIR peak of modest star forming galaxies at the luminosities of ULIRGs. In Figure 5.1 we have refit the four LN and four GOODS-N sources cited above as showing a submillimeter excess. The new fits are much better at SPIRE wavelengths, and like our [CII] sources in chapter 4, require SEDs with cool dust peaks scaled up by factors of 9-1300.

While this explanation is consistent with other findings and accounts for the observed sub-mm excess, one might legitimately ask, in a blind deep field like those studied here, if it might be yet unidentified source blending at long wavelengths that is responsible for the inability of our local SED models to capture the sub-mm excess. It is difficult to give an absolute answer to this question; certainly given free reign over the luminosity, redshift, SED, and separation an-

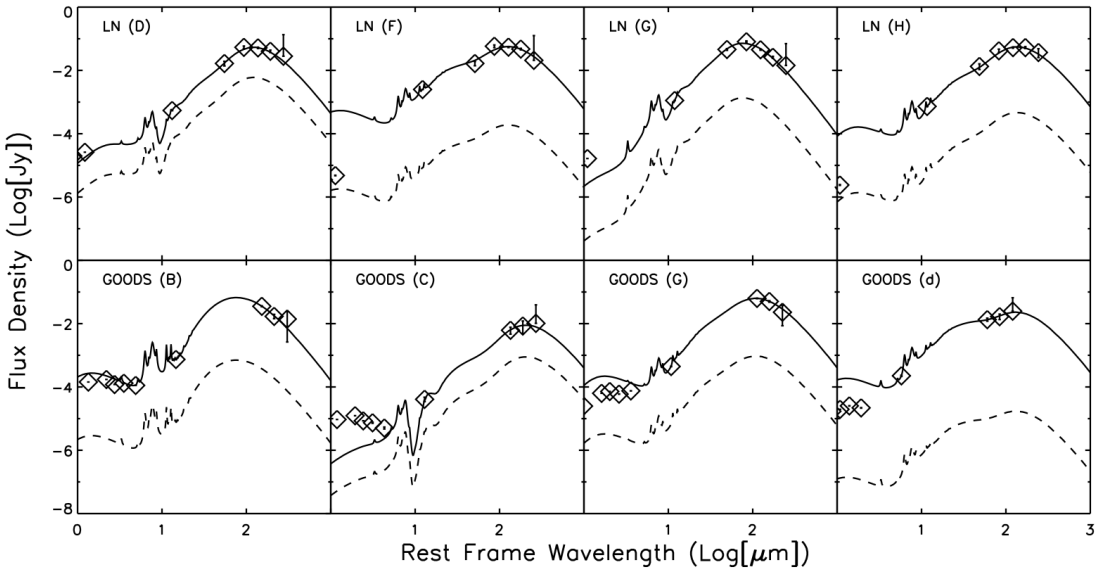

Figure 5.1 Galaxy SEDs from chapter 2 refit using the Siebenmorgen & Krugel SED library with an additional scaling factor. The intrinsic SED profile is plotted as a dashed line and the scaled up fit is the solid line. As in Figures 2.2,2.3, and 2.5, we fit based on photometry at 24 μm and longer, but include shorter wavelength data for display purposes only.

gle of a nearby source one could fine tune the parameters such that the primary source would be observed to have a sub-mm excess, and this is a possibility we admit in chapter 2. To understand how likely this explanation is, we have undertaken to explore the more limited question: "using unadulterated SEDs from Siebenmorgen and Krügel [2007] (without invoking multiplicative scale factors,) can a high luminosity, high redshift source, marginally blended with a moderate luminosity, local source demonstrate sub-mm excesses like those observed above?"

To explore this we selected 100 random 'primary' SED templates with bolometric luminosites $>10^{12}L_{\odot}$ and shifted them to z=2. We then paired each one with a randomly selected 'secondary' SED with luminosity $<10^{11}L_{\odot}$ at z=0.1 and assumed a separation from the primary source of 20". The separation an-

gle was chosen to give a good chance for selective source blending at SPIRE wavelengths while leaving the PACS bands relatively untouched, and the luminosities were chosen to represent the sources we were interested in at high redshifts, paired with relatively common sources which might exist undetected in the nearby Universe. We then calculated the simulated Herschel flux densities based on the intrinsic source SEDs and the PACS and SPIRE beam widths relative to the separation angle. Finally we took these calculated flux densities and attempted to fit them with a single SED at z=2 to evaluate the possibility that a blended SED might stymie the basic SED library.

We saw three characteristic results from the blended SEDs. The first characteristic result is the trivial case when the secondary source is far less luminous than the primary source and the blended SED is essentially the same as the primary SED. At long wavelengths the observed flux densities may be slightly inflated over the true primary SED, but it can still be fit by standard SED templates. Sixty three out of 100 blended SEDs demonstrate this result. The second characteristic result, which was quite common (occurring 28 times,) was the appearance of a 'broken' SED in which short wavelengths were clearly dominated by the primary source and longer wavelengths suddenly transitioned to being dominated by the secondary source. An example can be seen in Figure 5.2. This results when the secondary source is brighter in the FIR and the primary source SED peaks shortward of 100 μm. The resulting blended SED is distinctly unlike most observed galaxy SEDs and can't be well fit with a single template. The third characteristic result, also shown in Figure 5.2, is somewhat rarer, occurring 9 times when the secondary source was bright and the primary source has a fairly cool dust component, peaking beyond 100 μm. In this result we see a sub-mm excess like the ones we observed which are not well fit using a sin-

gle SED template without a scaling factor. Apparently then a simple blend of a high and low redshift source could create the profiles we have observed and attributed to very luminous galaxies with cool dust temperatures. Note, however, that if the secondary source dominates over the primary cool dust source in the FIR, *then it almost certainly dominates at shorter wavelengths as well.* The secondary source should therefore be well known and established at shorter wavelengths. Therefore it seems extremely unlikely that the submillimeter excesses we observe in these deep surveys could be the result of blending with a previously unidentified local object. In this case the secondary source would surely have been established in Spitzer 24 μm images. This is further evidence that we should be confident in our approach relying on multiwavelength data.

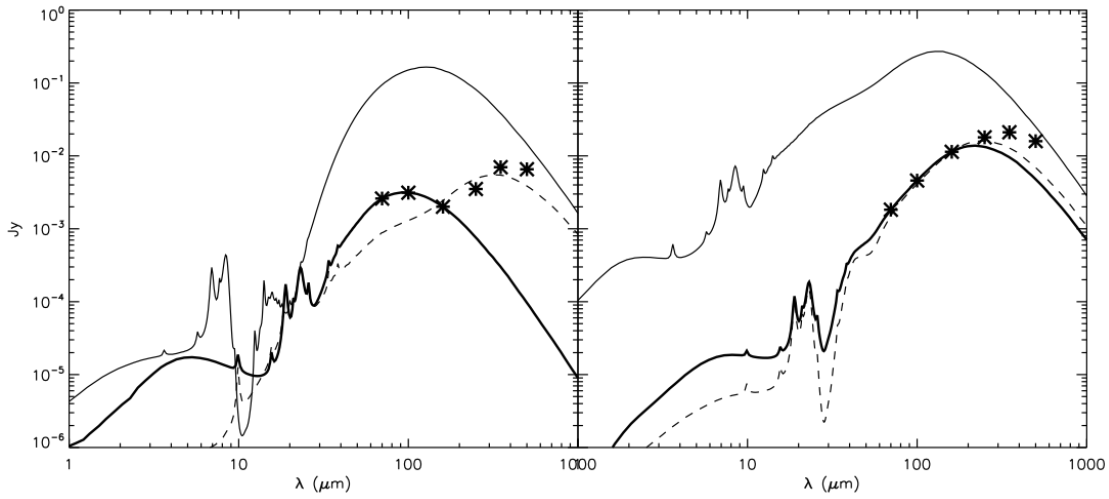

Figure 5.2 Two representative blended SEDs created assuming a primary high luminosity high redshift source and a secondary nearby lower luminosity source. Thick solid line represents the high redshift source, thin solid line represents the local source, and the dashed line represents the best fit to the blended Herschel observations (asterisks.) The 'broken' SED on the left cannot be well fit with a single dust temperature standard SED. The SED on the right demonstrates a sub millimeter excess similar to several of the high redshift sources observed in HerMES.

The compiled SEDs of our highly pure sources generally confirmed the

prevalence of ultra luminous, star formation powered, dust obscured sources in the early Universe. The particular selection of sources chosen in the paper may serve as a useful set of 'low hanging fruit' for spectroscopic follow up as they are robustly detected with known redshifts, and in many cases are very luminous (15 qualify as LIRGs or ULIRGs.) The overall performance of the purity index at selecting well isolated sources, along with the consistency of our findings based on those sources with the current theory, suggest that the metric is a useful tool.

5.2 Galaxy Mass, Metallicity, Radius and Star Formation Rates

Linked spectroscopic and photometric observations on $\sim 10^6$ sources from the SDSS are publicly available through the Max-Planck Institute for Astrophysics/ Johns Hopkins University catalog of SDSS galaxies [3]. We selected a sample of $\sim 10^5$ with which to examine bulk statistical relationships between mass, metallicity, radius, and star formation. The sample was selected to preserve sources with the best data (those with high S/N in a set of informative lines,) and to minimize the number of AGN present as identified by an emission line criterion established by Kauffmann et al. [2003a] (similar in style to the work of Baldwin et al. [1981],) with all sources confined to $0.07<z<0.3$ (representing $\sim$2.5 Gyr of the recent Universe.)

We characterized this sample by their stellar mass, star formation rate (as determined by Hα luminosity,) radius (photometric half-light radius,) and metallicity (based on various metal line ratios - see chapter 3.) We confirmed previous

[3] http://www.mpa-garching.mpg.de/SDSS/DR7/

findings of a very striking anti-correlation between star formation and metallicity: sources undergoing strong star formation have lower metallicity than quiescent sources. Furthermore, we found increased stellar mass moderated the effect: more massive galaxies show weaker metallicity depression during star formation episodes than less massive galaxies. The relationship can be seen at a glance in Figure 3.1.

The observed correlation is consistent with simple dilution of the galactic ISM by metal-poor gas accreting from pristine intergalactic reserves and simultaneously spurring star formation. We parameterized this toy model in the form of an equation:

$$Z_x = \frac{(\dot{M}_i \tau Z_i + M_g Z_0)}{(\dot{M}_i \tau + M_g)}, \tag{5.1}$$

where Z_x is the observed metallicity, M_g is the mass of native gas, Z_0 is the (relatively high) metallicity of native gas, Z_i is the (very low) metallicity of accreting gas, and $\dot{M}_i \tau$ is the accumulated mass of gas that has accreted in the current star formation episode. We linked the infalling mass to observable quantities by assuming the native gas mass is proportional to stellar mass and postulating that $\dot{M}_i \tau = \alpha (\mathrm{SFR})^{\gamma}$ where we found good results for $\gamma = 2/3$. In this form, α is the inverse of a star formation efficiency factor, relating how much star formation occurs given a certain amount of gas accretion.

Using our sample of 10^5 galaxies we were able to perform highly redundant fits on the handful of parameters that relate the physically observed quantities, and we found very good results for $Z_i < 0.25 \times 10^{-3}$ (N(O)/N(H) linear abundance), and $\alpha \tau_i M_* / M_g = 2.3 \times 10^9$ ($\mathrm{yr}^2\ \mathrm{M}_\odot$)$^{1/3}$. In section 3.7 we attempt to disentangle α, τ_i, and M_*/M_g based on other physical considerations, but due to the form of equation 5.1 these paramaters are not separable based on our data

alone. Of most interest is likely the finding of an upper limit to the accreting gas metallicity. If our toy model reflects reality, this finding implies that the average metallicity of material transiting galaxy halos and falling into galaxies will be very low, probably representing mostly pristine matter rather than heavily processed material previously ejected from galaxy disks.

5.2.1 Extensions

This remains an active area of research. With my support, Martin Harwit is leading the effort to refine this work. Among other improvements, we are attempting to more fully describe the physical model at work, incorporating explosive gas ejection, and the potential of galaxy magnetic fields to impede gas infall. We are also updating the work with a more recent understanding of metallicity, specifically considering alternate paths of nitrogen and oxygen enrichment in galaxies of varying mass and age.

5.3 Strong C^+ emission in galaxies at z$\sim$1-2: Evidence for cold flow accretion powered star formation in the early Universe

To extend the previous ZEUS survey of 13 galaxies at z=1 to 2 in the [CII] line, we have detected an additional eight. These eight sources were selected as known star formation dominated systems, seven of which have a reliable Spitzer IRS spectrum which show PAH emission. In addition to [CII] and PAHs, we have acquired [OI] observations on the majority of the sources and compiled photometry covering the FIR dust peak. This set of eight sources shows strong

[CII] emission. In several cases the [CII]/FIR ratio is in excess of 1%. Such high ratios stand out relative to the bulk of observed galaxies, but they are not unique outliers. There is precedent for such high ratios, observed both in local and high redshift systems, and also in several sub-galactic star forming regions.

The synthesis of all the data indicates that these systems are efficient star formers and lie on the galaxy 'main sequence' representing the proportionally high mass, high SFR range of 'normal' galaxies. The strong fine structure line emission along with the FIR continuum are consistent with PDR origins, and interpreted under this paradigm imply very extended star formation spread out over kpc scales. This may be the result of widespread infall from the cosmic web (as presented in our toy model in chapter 3.) Two systems have particularly high [CII]/FIR and [CII]/PAH ratios as well as cool dust temperatures, similar to several regions in Stephan's Quintet recently spatially resolved in [CII] observations by Appleton et al. [2013]. In these regions of Stephan's Quintet the major contributing source of the fine structure line emission appears to be diffuse lightly irradiated gas which is undergoing low velocity shocks. Such a scenario could explain the strong [CII] and [OI] emission without significantly contributing to PAH or FIR dust emission. In Stephan's Quintet the localized shocked regions are clearly undergoing major bulk motion and interaction with little to no active star formation. Our results are unique in that they apply to high redshift unresolved galaxies that are not already known to be undergoing an interaction with galactic neighbors. In our systems, it may be the same infalling gas that is powering star formation, also simultaneously leading to gas compression and shocks, powering a enhanced [CII] and [OI] emission above what normal PDRs explain.

In another source, SMM J03, for which we have additional information from a CO detection, PDR constraints are strong enough that we suggest ∼50% of the observed [CII] is coming from ionized gas, possibly indicating an especially OB star rich chapter of star formation, elevating the ionized gas fraction contributing to [CII] above the standard ∼30% that we would otherwise assume.

The PDR parameters found in our study bear out the findings of Stacey et al. [2010b], indicating modest UV fields ($G_0 \sim 10^{2-3}$) and therefore requiring extended star formation on ∼kpc scales to produce their (U)LIRG luminosities. This stands in stark contrast to ULIRGs in the local Universe which often have very low [CII]/FIR ratios, and much stronger UV fields, believed to be the result of major mergers between large galaxies. The significance of this result is clear. It suggests that star formation during the epoch of peak star formation at z∼1-2 occurs over extended, nearly galaxy wide scales, producing moderately intense UV fields rather than the intense UV fields present in many local ULIRGs.

This mode of star formation is probably not triggered by major mergers as such mergers lead to compact, and very intense star formation bursts, unlike the extended and less intense regions we observe. The process may be a simple extension of quiescent local star formation: cold flow accretion of gas from the cosmic web leads to a build up of gas densities that eventually result in dense molecular clouds which harbor star forming clusters. In the local Universe this may happen on a smaller scale, with streams of gas accreting over localized regions in galaxies (as supported by our work on local galaxies in the SDSS,) whereas in the early Universe it appears that a significant area of star forming galaxies are subject to gas accretion and star formation. In addition to reaffirming this general unifying picture of star forming galaxies in the early Universe,

our exceptional sources, SMM J03 and the two sources with suspected shock powered line emission, indicate that we are entering a level of sophistication in astronomical data where general trends have been established and further work will focus on the detailed pictures of smaller subcategories or individual systems.

5.3.1 Extensions

ZEUS also detected the [CII] line in radio source 3C 368 [Stacey et al., 2010b]. The [OI] 63 μm line was also strongly detected in this source as part of the Hailey-Dunsheath et al. [2014] Herschel program described. This source is unusual, however, in that it shows mixed signs of star formation and AGN dominance, with hints that the [CII] may be coming directly from the AGN emission region. This source is a High z Radio Galaxy (HzRG), a class of galaxies thought to be undergoing massive star formation on the scale of tens of kpc [Papadopoulos et al., 2000, De Breuck et al., 2003]. Although this type of source is likely to have an active central engine powering radio emission, it is thought that star formation dominates the infrared continuum in these sources due to the low level of polarization in the UV spectrum (indicating a largely stellar-powered UV emission.)

The detection of [CII] and [OI] in 3C 368 may be consistent with a star formation dominant origin, however the system also shows strong ionized emission lines in the infrared indicating large reserves of ionized gas. From the same Herschel survey that detected [OI] we also detect [OIII] 52 μm, [OIII] 88 μm, and [OIV] 26 μm, the last of which requires very hard radiation fields and strongly

implicates an AGN powered origin. The mid infrared IRS spectrum adds further evidence for very hard radiation fields. Figure 5.3 shows that the [Ne II], [Ne III], and [S IV] lines are all detected, but PAHs are conspicuously absent. Analysis is still in preliminary stages, however, the extremely high [CII]/PAH ratio is a mystery that seems at odds with the standard star formation powered PDR paradigm, and suggests an AGN origin for [CII]. The wealth of data available on this source, as well as its potentially unique nature, make it an exceptional target for in depth analysis. A unified approach modeling ionized and neutral gas simultaneously through the *Cloudy* radiative transfer simulation is a promising avenue for disentangling the multiple sources of emission that may be contributing to observations. Collaborative talks with Steve Hailey-Dunsheath and Gordon Stacey are underway.

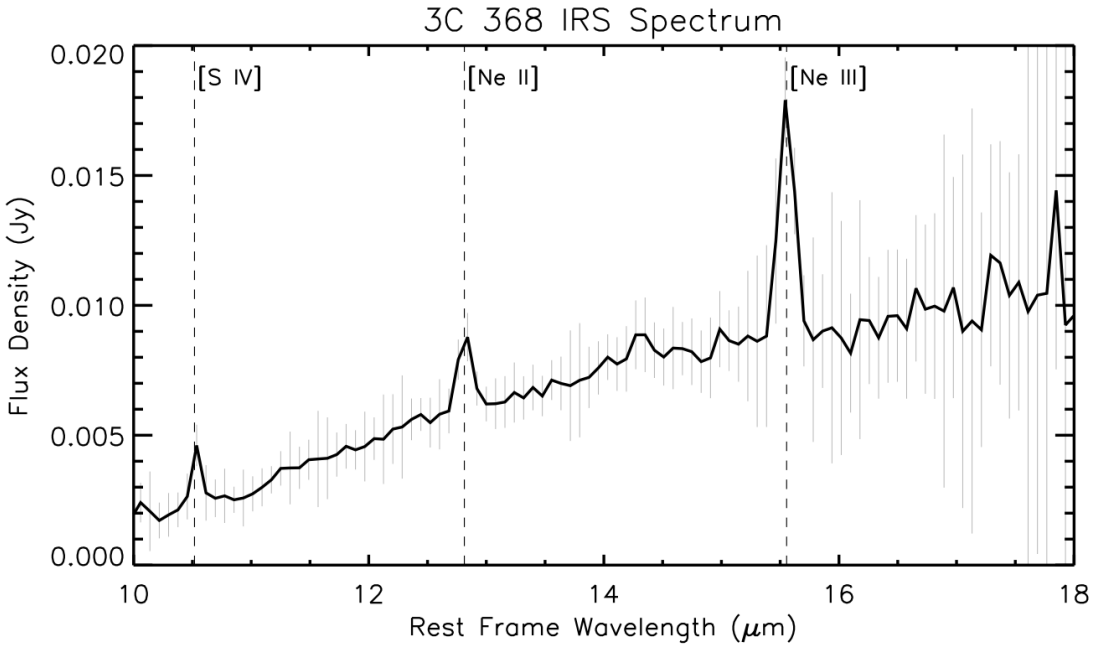

Figure 5.3 IRS spectrum of 3C 368. Light grey lines indicate error bars. Data from Cassis online, AORkey: 22912000 [Lebouteiller et al., 2011].

Another logical research extension is to turn to earlier epochs of the Universe. Metallicity is a fossil record of star formation in that gas phase elemental abundances will reflect the sum contributions of enrichment from generations of star formation, gas outflow, and gas accretion. At high redshifts many galaxies are still forming their first stellar populations and offer an ideal laboratory for studying the metal content in systems at early stages of galaxy evolution. Cosmological surveys suggest that average galactic metallicities may be undergoing rapid change prior to z$\sim$4. Surveys of rest-frame UV colors hint at a depression in chemical enrichment beginning around z $\sim$ 4-5 by showing a blueing of the UV spectral slope which increases in magnitude out to redshifts z$\sim$7 [Finkelstein et al., 2012]. This spectral blueing is likely due to decreased dust abundance at higher redshifts, but the relationship between dust extinction and metallicity is not well understood [cf. Issa et al., 1990, Inoue, 2003, Dunne et al., 2011]. In the rest frame UV there are also metal diagnostic lines which have been used to some effect in high redshift quasi-stellar objects (QSOs). Contrary to the other lines of evidence, high redshift QSO spectra indicate *enhanced*, usually supersolar, metallicity even out to z$\sim$6 [Juarez et al., 2009]. While it is tempting to take these observations as indications of galaxy-wide metallicities, they only apply to the broad line region, a relatively small spatial region that may not reflect the state of the overall host galaxy (and, in any case, does not reflect the broader population of non-QSO galaxies.)

I hope to begin to resolve the uncertain nature of metallicity in the early Universe by acquiring the first unambiguous metallicity measurements of star-forming galaxies at z>4. For a direct measurement of gas phase metallicity, we can turn to FIR fine structure lines coming from PDRs and ionized gas around O and B stars. Four fine structure lines are crucial to the survey: [NII] 205, [CII]

158, [OI] 146, and [NII] 122 μm. Based on the unique observing capabilities of ALMA, two epochs of the Universe are prime targets for this set of lines. All four lines will be observable in sources at 4.10<z<4.35 and 4.52<z<5.39. Below I describe the utility of these lines.

Nitrogen is generally considered a secondary element, created in the CNO cycle and requiring the prior seeding of other metals. Its production occurrs over multiple time-scales ranging from $\sim$0.1 to 1 Gyr [Pilyugin et al., 2003]. Carbon is a primary element. Models differ on the timescales over which carbon is produced [cf. Henry et al., 2000, Chiappini et al., 2003], but there is general agreement that the abundance ratio, N/C, increases with overall metallicity.

Since [CII] 158 and [NII] 205 are the two brightest fine structure lines with $\lambda_{rest} > 150$ μm they are enticing targets for ALMA at redshifts z>4. Furthermore, the lines have nearly identical critical densities when excited collisionally by electrons (44 and 46 cm^{-3} for [CII] and [NII] at 8000 K respectively) [Oberst et al., 2006]. Their ratio in HII regions will therefore be insensitive to density variations and since C^+ and N^+ lie in approximately the same ionization zones (C^+:11.3 to 24.4 eV, N^+: 14.5 to 29.6 eV), the [NII] 205/[CII] line ratio is a good indicator of the N/C abundance ratio. Despite its utility, the ratio, [NII]205/[CII], has only been determined in three high redshift sources [Nagao et al., 2012, Gallerani et al., 2012, Rawle et al., 2013]. Even a small number of additional detections would dramatically expand the sample of systems detected in both lines.

There is a complication in determining the N/C abundance ratio, however. The ionization energy of nitrogen is 14.5 eV so [NII] arises predominantly in HII regions. Carbon is ionized by 11.3 eV photons, so it arises largely from

PDRs with significant contributions from ionized gas. The fraction of bulk [CII] coming from ionized gas is highly variable, roughly 30±30% [Vasta et al., 2010, Oberst et al., 2011]. To precisely determine the underlying abundance ratio we need to determine the proportion of [CII] coming from neutral vs. ionized gas by characterizing both media. We can unravel this degeneracy by additionally observing [NII] 122 μm and [OI] 146 μm.

The [NII] 122 μm line is another useful probe of the ionized medium, and it has a higher critical density ($\sim$293 cm^{-3}) compared to [NII] 205 μm. The ratio of these two lines is therefore a sensitive probe of electron density in ionized regions, free of confounding abundance effects (see Figure 5.4) [Oberst et al., 2011]. Furthermore, since N^+ traces photons between 14.5 and 29.6 eV (above which N^{++} forms,) in star forming galaxies the [NII] lines directly measure early type stars, making them an excellent star formation indicator in dust obscured regions. Modulo variations in the stellar mass function, this will allow us to determine star formation rates in our high redshift sample with greater precision than is available from only the FIR continuum. Observations with ZEUS carried out by Ferkinhoff et al. [2011] are responsible for the only two detections of [NII] 122 μm at high redshift to date.

As explored in chapter 4, the strength of [CII] and [OI] 63 μm in conjunction with the FIR continuum (which we will detect in our [NII] 122 observations) can fully characterize the density and far UV (FUV) intensity in PDRs in extragalactic high redshift sources. In combination with the ionized gas lines, this allows us to break the degeneracy introduced by an uncertain PDR contribution to [CII] emission.

For the survey proposed here, the [OI] 146 μm line, (rather than the 63 μm

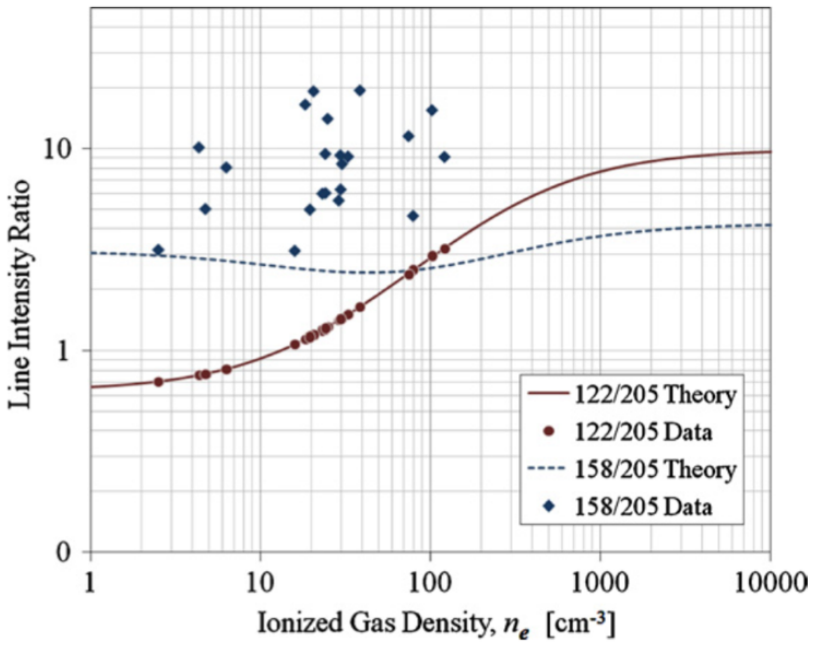

Figure 5.4 Modeled [NII]122/[NII]205 (red solid line) and [CII]/[NII]205 (blue dashed line) as a function of ionized gas electron density. Data is for the Carina Nebula. Reproduced from Figure 13 of [Oberst et al., 2011]. If all the observed [CII] line emission arises from ionized gas, then the [CII]/[NII] 205 μm ratio would be given by the blue dotted line. The further data points lie above the line, the greater the fraction of [CII] that does not arise from HII regions. This excess fraction arises in PDRs. The scatter in the [CII]/[NII]205 data is indicative of the variability of the fraction of [CII] coming from ionized vs. PDR gas.

line that we observed with Herschel/PACS for z$\sim$2 sources) will be used in conjunction with [CII]. The 146 μm line has advantages over the 63 μm line in that we can observe it in many of the same sources we observe the [NII] and [CII] lines, and, unlike the [OI] 63 μm line, it is optically thin [Stacey et al., 1983]. The different critical densities of [CII] and [OI] 146 (2.8×10^3 and 9.5×10^4 cm^{-3} respectively with hydrogen as the collision partner [Tielens and Hollenbach, 1985]) allow us to simultaneously determine the PDR hydrogen density (as seen in Figure 5.5). Furthermore, as we discuss in section 4.5, the observed FIR intensity measures the average FUV intensity within our telescope beam. Compared to the FUV intensity measured locally in PDRs by the fine structure

line ratios, we can find the PDR beam filling factor. The efficient [OI] and [CII] emission we observe at z$\sim$1-2, implying star formation with modest local UV fields spread over a multi-kpc extent was a major surprise in examining that epoch of the Universe. This proposed work will study the [CII] and [OI] lines simultaneously for the first time in galaxies at z$>$4.

Taken together, the four lines, [NII] 122, [OI] 146, [CII] 158, and [NII] 205, provide an unambiguous characterization of the ionized and PDR gas, allowing us to build a self consistent model to estimate the contribution of the ionized and neutral gas-phase components of the ISM to the [CII] emission and to determine a precise N/C abundance ratio. No previous high redshift work has wielded the synergy of all four (or even three) of these fine structure lines simultaneously.

By considering sources that have already been detected in [CII] or a lower-J CO line, we can determine a sample to confidently detect in all of our fine structure lines. At the accessible redshift intervals there are a few tens of such sources. For this initial foray into detailed fine structure line studies at z$>$4 the brightest star forming sources are the most promising. We find four sources in which we should detect all four fine structure lines with S/N of at least 5 in under 5 hours of ALMA observation total per source (not counting overhead time.) These sources are presented in Table 5.1. All of them also happen to have low-J CO detections, which will strengthen the precision with which we can constrain the source PDR properties.

The previous detections of [CII] or CO give confidence in detecting the other lines. For those detected in [CII] we need only attempt to observe the other three fine structure lines. Based on a set of $\sim$250 local sources in the Great Observatories All-sky LIRG Survey (GOALS), in which both [CII] and [NII] 205 were

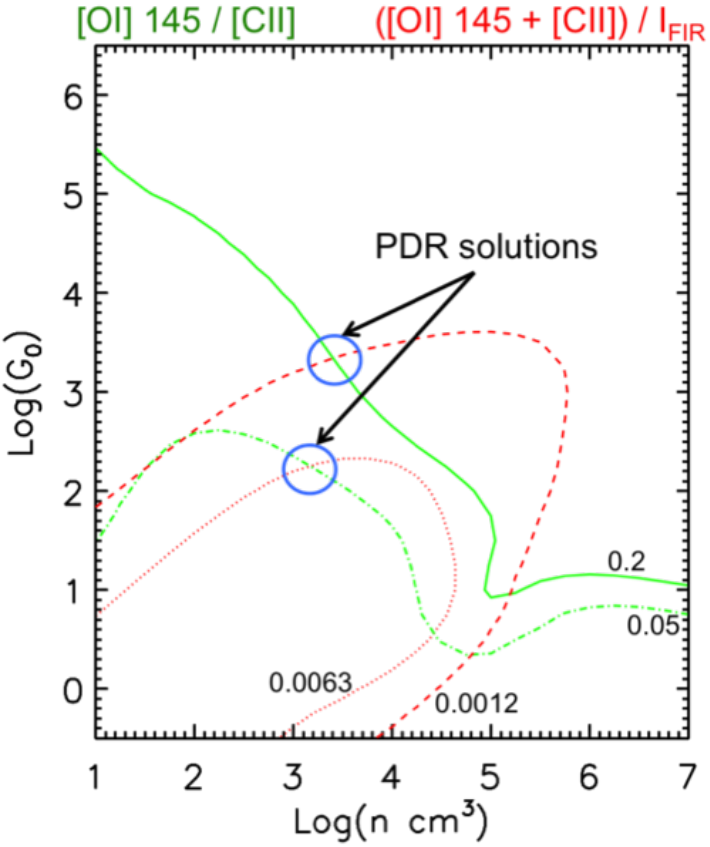

Figure 5.5 PDR models of the [OI] 146 /[CII] ratio (green) and ([OI] 146 + [CII])/I_{FIR} (red). We plot the predicted line ratio contours, parameterized by density (n) and FUV intensity (G_0). As examples of the diagnostic power of these two lines, we plot an example with intense UV fields (similar to local ULIRGs) (solid and dashed curves indicating [OI]/[CII]=0.2 and ([OI]+[CII])/I_{FIR}=0.0012) and moderate UV fields (dash-dotted and dotted curves indicating [OI]/[CII]=0.05 and ([OI]+[CII])/I_{FIR}=0.0063). The intersections of the line ratio contours represent n and G_0 values that satisfy both ratio values. The line ratios often yield two solutions for G_0 and n, but we note that the lower UV solution would require enormous sources, many tens of kpc in extent to account for the total UV luminosity that we observe reprocessed as FIR continuum. We therefore take the higher UV solutions (as indicated) which imply star formation over more reasonable scales (e.g. a few kpc for high z, high luminosity star forming galaxies). Data from online PDR Toolbox [Pound and Wolfire, 2008, Kaufman et al., 2006]

detected, we assume a minimum [NII] 205/[CII] line luminosity ratio of 0.04. This cut-off encompasses ∼95% of the GOALS sample. To estimate [OI] 146 we use an archival ISO sample from [Vasta et al., 2010]. In their sample of 28 extra-

galactic sources detected in [CII] and [OI] 146, all but three have [OI]146/[CII] $>$0.037. In the same ISO sample 12 sources were detected in both [CII] and [NII] 122. Eleven out of twelve have [NII]122/[CII]$>$0.06. We take these cut off ratios to very conservatively estimate fine structure line luminosities in our sources.

There are currently five high redshift sources which have published detections in [CII] and one of the other fine structure lines [Nagao et al., 2012, Gallerani et al., 2012, Rawle et al., 2013, Ferkinhoff et al., 2011]. Note that their ratios are above the minimum ratios used in estimating our line ratios. *Therefore, any non-detection would imply an extreme departure from the local population and have significant implications for the high redshift population. This would provide compelling evidence for peculiar emission mechanisms or depressed metallicity in the case of the nitrogen lines.*

In Table 5.1 we note our required sensitivities which are based on the minimum line flux estimates. Based on our extremely conservative line estimates we will achieve a signal to noise of five over a spectral bin equivalent to the FWHM of the [CII] (or CO) line used to estimate line fluxes. We will observe in a compact configuration with spatial resolution $\sim$1.5" to avoid over resolving the sources and requiring longer integration times.

From the observed [NII] lines we will directly calculate star formation rates. Using the spectral synthesis code, *Cloudy*, we will create a grid of self consistent line ratios for combined ionized gas and PDR models of varying densities, UV field intensities, and N/C abundances. Comparing our model grid to observed lines allows us to determine the fraction of [CII] from PDRs, PDR density and UV field intensity, and therefore star formation spatial extent, and the N/C abundance ratio.

Table 5.1 Summary of proposed sample and required sensitivities for S/N=5.

Source	z	Type	Known Line	ΔV (km/s)	Ref.	Target Line	Sensitivity (mJy)	Required Time (m)
HATLAS	4.243	lensed	[CII]	690	[26]	[NII] 122	1.10	31
J142413.9+022304		SMM				[OI] 146	0.81	30
						[NII] 205	1.23	28
BR	4.6906	SMM	[CII]	722	[27]	[NII] 122	0.14	301
1202-0725 N						[OI] 146	0.11	101
						[NII] 205	0.16	37
LESS	4.7534	SMM	[CII]	161	[29]	[NII] 122	0.52	278
J033229.4275619						[OI] 146	0.38	38
TN	5.2	star forming	CO (1-0)	300	[28]	[NII] 122	0.32	85
J0924-2201		radio galaxy				[OI] 146	0.24	53
						[CII] 158	6.97	28
						[NII] 205	0.36	36

The known line in column 4 represents the detected line which we use to estimate our minimum line luminosities. In all cases there are additional CO lines detected which we may use in our analysis but are less appropriate for estimating line luminosities. In column 5, ΔV is the FWHM of the [CII] (or CO) line. References refer to papers detecting the 'known line.' Sensitivity (column 8) is the required sensitivity for a line detection with S/N=5 binned over the ΔV noted in column 5. The Integration time is from the ALMA OT time estimate and includes overhead and calibrator time.

Representing a separate proposal in the same vein, the sample could be expanded to include sources which lack current [CII] line detections or spectroscopic redshifts, but have well constrained photometric redshifts and strong FIR continuum. The detection of the full set of fine structure lines is then riskier, but the sample size is larger. Spatially matching FIR surveys and photometric-z catalogs in COSMOS and ECDFS provide at least five additional candidates (possibly more depending on specific FIR luminosity and redshift precision criteria.) Given the uncertainty in their redshifts and fine structure line emission, this sample represents a riskier endeavor. As a companion proposal I would like to use ALMA to search for [CII] emission in these candidates. If [CII] is detected, their redshifts will be firmly established and they will be certain targets for observing the full set of lines in future proposals.

In summary, with a small ALMA survey I will establish a set of four galax-

ies which have well characterized densities, ionization parameters, and precise N/C abundance ratios. *This will give the first unambiguous indications of metallicity in galactic HII regions within ∼1.5 Gyr of the birth of the Universe.* All of this provides a compelling and logical extension of the star formation characterizations I have undertaken at z=1-2, and my metallicity investigation at $z<0.3$, allowing new insight into the evolution of the Universe.

APPENDIX A

ONE EXAMPLE OF SDSS SAMPLE SUMMARY TABLES FROM CHAPTER 3. (FULL SET AVAILABLE ONLINE.)

The following set of tables represent the summarized data for our SDSS sample of the low redshift, medium radius galaxies. Each bin in any table corresponds to a specific stellar mass (columns) and star formation rate (rows.) The stellar mass and star formation rate values are given in the first row and column, respectively, with units of ($10^{10}M_{\odot}$) and ($M_{\odot}/yr$). This particular set of tables along with eight similar sets corresponding to each other permutation of our three redshift ranges and three radius ranges are all available online at the Astrophysical Journal html publication of Brisbin and Harwit [2012].

Table A.1 SDSS extracted sample size as a function of SFR and M_*

M_*: SFR	0.126	0.178	0.251	0.355	0.501	0.708	1	1.41	2	2.82	3.98	5.62	7.94	11.2	15.8	22.4
0.035	1	0	0	8	14	13	11	4	1	0	0	0	0	0	0	0
0.05	1	0	5	20	51	52	28	22	11	4	2	0	0	0	0	0
0.071	2	2	10	47	100	118	121	79	33	20	7	1	1	0	1	0
0.1	0	3	24	88	174	271	243	184	113	55	25	3	3	1	0	0
0.14	0	0	27	78	260	374	386	352	274	142	55	21	7	2	1	0
0.2	0	3	16	86	242	445	520	494	390	240	119	62	12	3	1	0
0.28	1	4	10	65	175	399	575	535	493	339	203	87	24	12	3	1
0.4	0	0	5	35	100	261	424	501	489	439	234	97	40	8	3	0
0.56	0	1	2	15	60	134	261	390	436	421	254	114	55	14	5	0
0.79	1	0	0	8	27	58	111	238	291	334	251	128	54	14	2	1
1.12	0	1	0	5	1	20	52	119	173	207	182	125	57	19	7	0
1.58	0	0	0	4	2	8	21	40	82	131	128	91	52	11	3	0
2.24	0	0	0	0	0	4	3	10	36	54	64	52	33	10	2	0
3.16	0	0	0	0	0	1	2	7	8	18	30	38	30	8	1	0
4.47	0	0	0	1	0	0	2	1	3	7	14	23	13	2	0	0
6.31	0	0	0	0	0	0	0	1	1	0	5	4	2	4	0	0

Table A.2 SDSS sample median Petrosian half light radius (kpc).

M_*: SFR	0.126	0.178	0.251	0.355	0.501	0.708	1	1.41	2	2.82	3.98	5.62	7.94	11.2	15.8	22.4
0.035	4.56			4.54	4.45	4.37	4.6	4.58	4.8							
0.05	4.64		4.24	4.44	4.49	4.32	4.39	4.41	4.32	4.29	4.91					
0.071	4.34	4.93	4.12	4.3	4.4	4.35	4.35	4.44	4.27	4.58	4.38	4.73	4.05		3.93	
0.1		4.18	4.23	4.24	4.26	4.37	4.37	4.2	4.37	4.37	4.24	4.73	4.21	4.64		
0.14			4.23	4.17	4.21	4.24	4.36	4.32	4.36	4.34	4.32	4.55	4.08	4.61	4.75	
0.2		4.02	4.33	4.23	4.14	4.23	4.29	4.26	4.34	4.29	4.36	4.42	4.5	4.87	3.8	
0.28	4.94	4.28	4.23	4.08	4.06	4.16	4.22	4.24	4.32	4.28	4.37	4.35	4.39	4.35	4.26	3.75
0.4			4.31	4.12	4.1	4.14	4.17	4.17	4.23	4.28	4.36	4.31	4.4	4.58	4.49	
0.56		3.72	4.83	3.97	4	4.08	4.06	4.15	4.17	4.28	4.32	4.39	4.44	4.47	4.81	
0.79	4.93			3.98	4.06	4.05	4.03	4.05	4.14	4.21	4.31	4.38	4.36	4.54	4.85	4.66
1.12		4.11		3.93	3.81	4.01	4.02	4.09	4.05	4.19	4.31	4.3	4.3	4.49	4.39	
1.58				3.97	4.01	4.23	3.98	4.23	4.11	4.17	4.1	4.18	4.18	4.4	4.56	
2.24						4.33	4.51	4.13	3.94	4.1	4.16	4.32	4.23	4.38	4.42	
3.16						3.84	4.59	3.94	4.27	4.1	4.06	4.09	4.18	4.6	4.13	
4.47				3.89			3.96	3.92	4.07	3.86	4.15	4.19	4.22	4.65		
6.31								3.83	4.77		4.05	4.33	4.48	4.03		

Table A.3 SDSS sample median metallicity ((O/H)(10^{-3})).

M_*: SFR	0.126	0.178	0.251	0.355	0.501	0.708	1	1.41	2	2.82	3.98	5.62	7.94	11.2	15.8	22.4
0.035	0.66			0.97	1.02	1.15	1.23	1.56	1.51							
0.05	0.63		0.74	0.86	0.98	1.09	1.24	1.29	1.47	1.25	1.62					
0.071	0.59	0.66	0.78	0.83	0.96	1.07	1.18	1.27	1.31	1.29	1.4	0.7	1.46		1.23	
0.1		0.58	0.72	0.81	0.94	1.02	1.14	1.23	1.26	1.35	1.3	1.42	1.6	2.31		
0.14			0.65	0.78	0.88	1	1.08	1.19	1.26	1.3	1.3	1.33	1.22	1.69	0.98	
0.2		0.44	0.6	0.76	0.87	0.99	1.08	1.15	1.21	1.26	1.29	1.38	1.33	1.53	2.19	
0.28	0.79	0.57	0.65	0.73	0.85	0.96	1.06	1.14	1.18	1.25	1.28	1.33	1.34	1.25	1.75	0.97
0.4			0.63	0.67	0.79	0.93	1.04	1.12	1.19	1.22	1.24	1.3	1.39	1.5	1.75	
0.56		0.47	0.65	0.62	0.76	0.89	1.01	1.12	1.17	1.22	1.26	1.28	1.29	1.37	1.47	
0.79	1.23			0.56	0.71	0.81	1.03	1.1	1.18	1.24	1.28	1.27	1.3	1.36	1.44	0.97
1.12		0.86		0.51	0.71	0.82	0.98	1.07	1.15	1.24	1.29	1.26	1.3	1.31	1.17	
1.58				0.4	0.62	0.77	0.85	1.02	1.15	1.23	1.3	1.3	1.3	1.37	1.52	
2.24						0.84	0.66	0.92	1.12	1.21	1.29	1.29	1.35	1.37	1.38	
3.16						0.68	1.48	0.95	1.09	1.13	1.38	1.33	1.29	1.41	1.39	
4.47				1.16			0.78	0.85	1.1	1.11	1.25	1.31	1.28	1.64		
6.31								0.49	0.93		1.2	1.49	1.65	1.32		

Table A.4 SDSS sample metallicity standard deviation ((O/H)(10^{-3})).

M_*: SFR	0.126	0.178	0.251	0.355	0.501	0.708	1	1.41	2	2.82	3.98	5.62	7.94	11.2	15.8	22.4
0.035				0.09	0.23	0.12	0.14	0.13								
0.05			0.14	0.11	0.13	0.13	0.16	0.2	0.23	0.34	0.23					
0.071	0.05	0.11	0.1	0.13	0.12	0.14	0.17	0.22	0.22	0.16	0.13					
0.1		0.03	0.1	0.1	0.12	0.13	0.15	0.16	0.18	0.22	0.23	0.09	0.93			
0.14			0.13	0.11	0.12	0.12	0.13	0.16	0.18	0.21	0.28	0.22	0.34	0.69		
0.2		0.22	0.12	0.11	0.11	0.13	0.14	0.16	0.16	0.17	0.24	0.36	0.34	0.11		
0.28		0.06	0.13	0.11	0.13	0.14	0.14	0.14	0.17	0.18	0.19	0.23	0.45	0.55	0.53	
0.4			0.09	0.09	0.13	0.13	0.14	0.15	0.16	0.18	0.18	0.22	0.16	0.63	0.79	
0.56			0.09	0.21	0.11	0.15	0.14	0.16	0.18	0.19	0.17	0.22	0.22	0.48	0.54	
0.79				0.11	0.13	0.14	0.16	0.15	0.17	0.19	0.19	0.2	0.25	0.34	0.12	
1.12				0.07		0.15	0.23	0.16	0.18	0.19	0.19	0.18	0.2	0.25	0.44	
1.58				0.03	0.14	0.18	0.14	0.16	0.24	0.19	0.18	0.21	0.31	0.19	0.07	
2.24						0.18	0.17	0.11	0.21	0.21	0.22	0.17	0.16	0.25	0.61	
3.16							0.64	0.22	0.2	0.17	0.17	0.16	0.11	0.18		
4.47							0.13		0.07	0.21	0.15	0.13	0.15	0.22		
6.31											0.1	0.12	0.08	0.11		

APPENDIX B

PHOTOMETRY USED IN SED FITTING FOR CHAPTER 4.

The following table gives the photometry used to fit SEDs to our [CII] sources in section 4.4.2. Each entry gives instrument and wave band on the first line, followed by measurement and reference code on the second line. SPIRE 250, 350, and 500 μm uncertainties are set to 30% to account for potential confusion noise. In fitting the 24 μm photometry we used ten times the uncertainty quoted here to compensate for the inflexible treatment of PAH fluxes in the model grid. These photometry are not color corrected. In all cases, color correcting the PACS and SPIRE photometry resulted in changes less than 10%. References: [1][Fiolet et al., 2009], [2][Farrah et al., 2008], [3][Fadda et al., 2006], [4][Efstathiou and Siebenmorgen, 2009], [5][Hainline et al., 2009b], [6][Sajina et al., 2007], [7](Data from Herschel program GT1_dlutz_4 - flux extracted using standard HIPE methods), [8](this work), [9][Sajina et al., 2008], [10](HerMES image - flux extracted using [CII] position as prior), [11](HerMES source catalog), [12][Kovács et al., 2006], [13][Webb et al., 2003].

Table B.1

SWIRE 4-5	SWIRE 4-15	SWIRE 3-14	SWIRE 3-18	SWIRE 3-9	MIPS 22530	SDSS J12	SMM J03
MIPS 24	MIPS 24	MIPS 24	MIPS 24	MIPS 24	MIPS 24		MIPS 24
0.550±0.015 [1]	0.419±0.018 [1]	0.874±0.087 [2]	0.761±0.076 [2]	1.0±0.1 [2]	1.23±0.06 [3]		0.23±0.02 [4]
							0.47±0.05 [5]
					MIPS 70	PACS 70	PACS 70
					3.4±1.9 [6]	9.7±3.3 [7]	21.3±4.4 [8]
						PACS 100	PACS 100
						16.5±1.5 [7]	48.6±3.5 [8]
					MIPS 160	PACS 160	PACS 160
					38±9 [9]	39±21 [7]	64.8±6.5 [8]
SPIRE 250	SPIRE 250	SPIRE 250	SPIRE 250	SPIRE 250	SPIRE 250	SPIRE 250	
19.2±5.8 [10]	21.7±6.5 [10]	56±18 [10]	42±13 [10]	51±15 [10]	61±18 [11]	30.8±9.2 [7]	
SPIRE 350	SPIRE 350	SPIRE 350	SPIRE 350	SPIRE 350	SPIRE 350	SPIRE 350	SHARC2 350
17.1±5.1 [10]	31.5±9.5 [10]	61±18 [11]	49±15 [11]	48±14 [10]	53±16 [11]	15.5±4.7 [7]	42.2±9.8 [12]
		SPIRE 500	SPIRE 500	SPIRE 500	SPIRE 500	SPIRE 500	SCUBA 450
		40±12 [11]	32±10 [10]	29.2±8.8 [10]	26.3±7.9 [10]	14.9±4.5 [7]	<63 [13]
MAMBO 1200	MAMBO 1200				MAMBO 1200		SCUBA 850
2.75±0.76 [1]	2.36±0.62 [1]				2.11±0.56 [9]		4.4±1.3 [13]

BIBLIOGRAPHY

H. Aihara and et al. The Eighth Data Release of the Sloan Digital Sky Survey: First Data from SDSS-III. *ApJS*, 193:29, April 2011.

C.W. Allen and A.N. Cox. *Allen's Astrophysical Quantities, 4th ed.* Springer, 1999. ISBN 9780387987460.

P. N. Appleton, et al. Shock-enhanced C^+ Emission and the Detection of H_2O from the Stephan's Quintet Group-wide Shock Using Herschel. *ApJ*, 777:66, November 2013.

J. A. Baldwin, M. M. Phillips, and R. Terlevich. Classification parameters for the emission-line spectra of extragalactic objects. *PASP*, 93:5–19, February 1981.

A. J. Barger, L. L. Cowie, and W.-H. Wang. A Highly Complete Spectroscopic Survey of the GOODS-N Field1,. *ApJ*, 689:687–708, December 2008.

E. F. Bell, D. H. McIntosh, N. Katz, and M. D. Weinberg. The Optical and Near-Infrared Properties of Galaxies. I. Luminosity and Stellar Mass Functions. *ApJS*, 149:289–312, December 2003.

S. Berta, et al. Dissecting the cosmic infra-red background with Herschel/PEP. *A&A*, 518:L30, July 2010.

M. Béthermin, H. Dole, M. Cousin, and N. Bavouzet. Submillimeter number counts at 250 μm, 350 μm and 500 μm in BLAST data. *A&A*, 516:A43, June 2010.

Y. Birnboim and A. Dekel. Gravitational quenching by clumpy accretion in cool-core clusters: convective dynamical response to overheating. *MNRAS*, 415: 2566–2579, August 2011.

L. Blitz and E. Rosolowsky. The Role of Pressure in GMC Formation II: The H_2-Pressure Relation. *ApJ*, 650:933–944, October 2006.

A. D. Bolatto, A. K. Leroy, E. Rosolowsky, F. Walter, and L. Blitz. The Resolved Properties of Extragalactic Giant Molecular Clouds. *ApJ*, 686:948–965, October 2008.

N. Bouché, et al. The Impact of Cold Gas Accretion Above a Mass Floor on Galaxy Scaling Relations. *ApJ*, 718:1001–1018, August 2010.

R. J. Bouwens and G. D. Illingworth. Rapid evolution of the most luminous galaxies during the first 900million years. *Nature*, 443:189–192, September 2006.

R. G. Bower, A. J. Benson, R. Malbon, J. C. Helly, C. S. Frenk, C. M. Baugh, S. Cole, and C. G. Lacey. Breaking the hierarchy of galaxy formation. *MNRAS*, 370:645–655, August 2006.

J. R. Brauher, D. A. Dale, and G. Helou. A Compendium of Far-Infrared Line and Continuum Emission for 227 Galaxies Observed by the Infrared Space Observatory. *ApJS*, 178:280–301, October 2008.

D. Brisbin and M. Harwit. Galaxy Mass, Metallicity, Radius, and Star Formation Rates. *ApJ*, 750:142, May 2012.

A. M. Brooks, F. Governato, C. M. Booth, B. Willman, J. P. Gardner, J. Wadsley, G. Stinson, and T. Quinn. The Origin and Evolution of the Mass-Metallicity Relationship for Galaxies: Results from Cosmological N-Body Simulations. *ApJL*, 655:L17–L20, January 2007.

V. Buat, et al. Measures of star formation rates from infrared (Herschel) and UV (GALEX) emissions of galaxies in the HerMES fields. *MNRAS*, 409:L1–L6, November 2010.

E. M. Burbidge and G. R. Burbidge. Some Interconnected Multiple Extragalactic Nebulae. *ApJ*, 130:23, July 1959.

D. Calzetti and R. C. Kennicutt. The New Frontier: Galactic-Scale Star Formation. *PASP*, 121:937–941, September 2009.

J. A. Cardelli, G. C. Clayton, and J. S. Mathis. The relationship between infrared, optical, and ultraviolet extinction. *ApJ*, 345:245–256, October 1989.

G. Chabrier. Galactic Stellar and Substellar Initial Mass Function. *PASP*, 115: 763–795, July 2003.

G. Chabrier. The initial mass function 50 years later, ed corelli e., palla f., & zinnecker h, 2005.

S. C. Chapman, A. W. Blain, I. Smail, and R. J. Ivison. A Redshift Survey of the Submillimeter Galaxy Population. *ApJ*, 622:772–796, April 2005.

C. Chiappini, D. Romano, and F. Matteucci. Oxygen, carbon and nitrogen evolution in galaxies. *MNRAS*, 339:63–81, February 2003.

J. W. Colbert, et al. ISO LWS Spectroscopy of M82: A Unified Evolutionary Model. *ApJ*, 511:721–729, February 1999.

K. E. K. Coppin, et al. Herschel-PACS observations of [O I]63 μm towards submillimetre galaxies at z $\sim$ 1. *MNRAS*, 427:520–532, November 2012.

L. L. Cowie, A. J. Barger, and E. M. Hu. Lyα Emitting Galaxies as Early Stages in Galaxy Formation. *ApJ*, 738:136, September 2011.

M. K. Crawford, R. Genzel, C. H. Townes, and D. M. Watson. Far-infrared spectroscopy of galaxies - The 158 micron C(+) line and the energy balance of molecular clouds. *ApJ*, 291:755–771, April 1985.

K. V. Croxall, et al. Resolving the Far-IR Line Deficit: Photoelectric Heating and Far-IR Line Cooling in NGC 1097 and NGC 4559. *ApJ*, 747:81, March 2012.

E. Daddi, et al. Multiwavelength Study of Massive Galaxies at z$\sim$2. II. Widespread Compton-thick Active Galactic Nuclei and the Concurrent Growth of Black Holes and Bulges. *ApJ*, 670:173–189, November 2007.

E. Daddi, et al. Very High Gas Fractions and Extended Gas Reservoirs in z = 1.5 Disk Galaxies. *ApJ*, 713:686–707, April 2010.

J. J. Dalcanton. The Metallicity of Galaxy Disks: Infall versus Outflow. *ApJ*, 658: 941–959, April 2007.

D. A. Dale, G. Helou, J. R. Brauher, R. M. Cutri, S. Malhotra, and C. A. Beichman. [O I] 63 Micron Emission from High- and Low-Luminosity Active Galactic Nucleus Galaxies. *ApJ*, 604:565–571, April 2004.

A. Dalgarno and R. A. McCray. Heating and Ionization of HI Regions. *ARA&A*, 10:375, 1972.

R. Davé, K. Finlator, and B. D. Oppenheimer. Galaxy evolution in cosmological simulations with outflows - II. Metallicities and gas fractions. *MNRAS*, 416: 1354–1376, September 2011a.

R. Davé, B. D. Oppenheimer, and K. Finlator. Galaxy evolution in cosmological simulations with outflows - I. Stellar masses and star formation rates. *MNRAS*, 415:11–31, July 2011b.

C. De Breuck, et al. CO emission and associated H I absorption from a massive gas reservoir surrounding the z = 3 radio galaxy B3 J2330+3927. *A&A*, 401: 911–925, April 2003.

C. De Breuck, R. Maiolino, P. Caselli, K. Coppin, S. Hailey-Dunsheath, and T. Nagao. Enhanced [CII] emission in a z = 4.76 submillimetre galaxy. *A&A*, 530:L8, June 2011.

T. de Graauw, et al. The Herschel-Heterodyne Instrument for the Far-Infrared (HIFI). *A&A*, 518:L6, July 2010.

R. S. de Jong. Near-infrared and optical broadband surface photometry of 86 face-on disk dominated galaxies. IV. Using color profiles to study stellar and dust content of galaxies. *A&A*, 313:377–395, September 1996.

V. Desai, et al. Strong Polycyclic Aromatic Hydrocarbon Emission from z$\sim$2 ULIRGs. *ApJ*, 700:1190–1204, August 2009.

T. Díaz-Santos, et al. Explaining the [C II]157.7 μm Deficit in Luminous Infrared Galaxies - First Results from a Herschel/PACS Study of the GOALS Sample. *ApJ*, 774:68, September 2013.

L. Dunne, et al. The star formation history of K-selected galaxies. *MNRAS*, 394: 3–20, March 2009.

L. Dunne, et al. Herschel-ATLAS: rapid evolution of dust in galaxies over the last 5 billion years. *MNRAS*, 417:1510–1533, October 2011.

A. Efstathiou and R. Siebenmorgen. Starburst and cirrus models for submillimeter galaxies. *A&A*, 502:541–548, August 2009.

D. Elbaz, et al. GOODS-Herschel: an infrared main sequence for star-forming galaxies. *A&A*, 533:A119, September 2011.

S. L. Ellison, D. R. Patton, L. Simard, and A. W. McConnachie. Clues to the Origin of the Mass-Metallicity Relation: Dependence on Star Formation Rate and Galaxy Size. *ApJL*, 672:L107–L110, January 2008.

B. G. Elmegreen. The H to H2 transition in galaxies - Totally molecular galaxies. *ApJ*, 411:170–177, July 1993.

D. Fadda, et al. The Spitzer Space Telescope Extragalactic First Look Survey: 24 μm Data Reduction, Catalog, and Source Identification. *AJ*, 131:2859–2876, June 2006.

R. Fadely, et al. Mid-infrared Spectroscopy of Two Lensed Star-forming Galaxies. *ApJ*, 723:729–736, November 2010.

X. Fan, et al. A Survey of z$>$5.7 Quasars in the Sloan Digital Sky Survey. IV. Discovery of Seven Additional Quasars. *AJ*, 131:1203–1209, March 2006.

D. Farrah, et al. The Spatial Clustering of Ultraluminous Infrared Galaxies over $1.5 < z < 3$. *ApJL*, 641:L17–L20, April 2006.

D. Farrah, et al. The Nature of Star Formation in Distant Ultraluminous Infrared Galaxies Selected in a Remarkably Narrow Redshift Range. *ApJ*, 677:957–969, April 2008.

C.-A. Faucher-Giguère, D. Kereš, and C.-P. Ma. The baryonic assembly of dark matter haloes. *MNRAS*, 417:2982–2999, November 2011.

C. Ferkinhoff, S. Hailey-Dunsheath, T. Nikola, S. C. Parshley, G. J. Stacey, D. J. Benford, and J. G. Staguhn. First Detection of the [O III] 88 μm Line at High Redshifts: Characterizing the Starburst and Narrow-line Regions in Extreme Luminosity Systems. *ApJL*, 714:L147–L151, May 2010.

C. Ferkinhoff, et al. First Detections of the [N II] 122 μm Line at High Redshift: Demonstrating the Utility of the Line for Studying Galaxies in the Early Universe. *ApJL*, 740:L29, October 2011.

C. Ferkinhoff, et al. The Second-generation z (Redshift) and Early Universe Spectrometer. I. First-light Observation of a Highly Lensed Local-ulirg Analog at High-z. *ApJ*, 780:142, January 2014.

S. L. Finkelstein, et al. Candels: The Evolution of Galaxy Rest-frame Ultraviolet Colors from z = 8 to 4. *ApJ*, 756:164, September 2012.

K. Finlator and R. Davé. The origin of the galaxy mass-metallicity relation and implications for galactic outflows. *MNRAS*, 385:2181–2204, April 2008.

N. Fiolet, et al. Multi-wavelength properties of Spitzer selected starbursts at z $\sim$ 2. *A&A*, 508:117–132, December 2009.

N. Fiolet, et al. Mid-infrared spectroscopy of Spitzer-selected ultra-luminous starbursts at z $\sim$ 2. *A&A*, 524:A33, December 2010.

J. Fischer, et al. Herschel-PACS spectroscopic diagnostics of local ULIRGs: Conditions and kinematics in Markarian 231. *A&A*, 518:L41, July 2010.

D. J. Fixsen, E. Dwek, J. C. Mather, C. L. Bennett, and R. A. Shafer. The Spectrum of the Extragalactic Far-Infrared Background from the COBE FIRAS Observations. *ApJ*, 508:123–128, November 1998.

A. Gallazzi, S. Charlot, J. Brinchmann, S. D. M. White, and C. A. Tremonti. The ages and metallicities of galaxies in the local universe. *MNRAS*, 362:41–58, September 2005.

S. Gallerani, et al. Resolved [CII] emission in a lensed quasar at z = 4.4. *A&A*, 543:A114, July 2012.

S. Genel, R. Genzel, N. Bouché, T. Naab, and A. Sternberg. The Halo Merger Rate in the Millennium Simulation and Implications for Observed Galaxy Merger Fractions. *ApJ*, 701:2002–2018, August 2009.

A. E. Glassgold and W. D. Langer. Heating of Molecular-Hydrogen Clouds by Cosmic Rays and X-Rays. *ApJ*, 186:859–888, December 1973.

P. F. Goldsmith and W. D. Langer. Molecular cooling and thermal balance of dense interstellar clouds. *ApJ*, 222:881–895, June 1978.

J. Graciá-Carpio, et al. Far-infrared Line Deficits in Galaxies with Extreme L_{FIR}/H_2 Ratios. *ApJL*, 728:L7, February 2011.

M. J. Griffin, et al. The Herschel-SPIRE instrument and its in-flight performance. *A&A*, 518:L3, July 2010.

J. Guedes, S. Callegari, P. Madau, and L. Mayer. Forming Realistic Late-type Spirals in a ΛCDM Universe: The Eris Simulation. *ApJ*, 742:76, December 2011.

P. Guillard, et al. Turbulent Molecular Gas and Star Formation in the Shocked Intergalactic Medium of Stephan's Quintet. *ApJ*, 749:158, April 2012.

S. Hailey-Dunsheath. *Probing star formation at low and high redshift with ZEUS, a new submillimeter grating spectrometer*. PhD thesis, Cornell University, June 2009.

S. Hailey-Dunsheath, T. Nikola, G. J. Stacey, T. E. Oberst, S. C. Parshley, C. M. Bradford, P. A. R. Ade, and C. E. Tucker. Detection of the ^{13}CO J=6–5 transition in the Starburst Galaxy NGC 253. *ApJL*, 689:L109–L112, December 2008.

S. Hailey-Dunsheath, T. Nikola, G. J. Stacey, T. E. Oberst, S. C. Parshley, D. J. Benford, J. G. Staguhn, and C. E. Tucker. Detection of the 158 μm [C II] Transition at z = 1.3: Evidence for a Galaxy-wide Starburst. *ApJL*, 714:L162–L166, May 2010.

S. Hailey-Dunsheath, et al. in prep. 2014.

K. N. Hainline, A. E. Shapley, K. A. Kornei, M. Pettini, E. Buckley-Geer, S. S. Allam, and D. L. Tucker. Rest-Frame Optical Spectra of Three Strongly Lensed Galaxies at z $\sim$ 2. *ApJ*, 701:52–65, August 2009a.

L. J. Hainline, A. W. Blain, I. Smail, D. T. Frayer, S. C. Chapman, R. J. Ivison, and D. M. Alexander. A Mid-Infrared Imaging Survey of Submillimeter-Selected Galaxies with the Spitzer Space Telescope. *ApJ*, 699:1610–1632, July 2009b.

M. Harwit, J. R. Houck, B. T. Soifer, and G. G. C. Palumbo. The most luminous far-infrared extragalactic sources. *ApJ*, 315:28–45, April 1987.

R. B. C. Henry, M. G. Edmunds, and J. Köppen. On the Cosmic Origins of Carbon and Nitrogen. *ApJ*, 541:660–674, October 2000.

R. H. Hildebrand, R. F. Loewenstein, D. A. Harper, G. S. Orton, J. Keene, and S. E. Whitcomb. Far-infrared and submillimeter brightness temperatures of the giant planets. *Icarus*, 64:64–87, October 1985.

J. R. Houck, et al. The infrared spectrograph on the Spitzer Space Telescope. In J. C. Mather, editor, *Optical, Infrared, and Millimeter Space Telescopes*, volume 5487 of *Society of Photo-Optical Instrumentation Engineers (SPIE) Conference Series*, pages 62–76, October 2004.

J.-S. Huang, et al. Infrared Spectrograph Spectroscopy and Multi-Wavelength Study of Luminous Star-Forming Galaxies at z $\sim$ 1.9. *ApJ*, 700:183–198, July 2009.

A. K. Inoue. Evolution of Dust-to-Metal Ratio in Galaxies. *Publications of the Astronomical Society of Japan*, 55:901–909, October 2003.

M. R. Issa, I. MacLaren, and A. W. Wolfendale. Dust-to-gas ratio and metallicity variations in nearby galaxies. *A&A*, 236:237–241, September 1990.

R. J. Ivison, et al. Herschel and SCUBA-2 imaging and spectroscopy of a bright, lensed submillimetre galaxy at z = 2.3. *A&A*, 518:L35, July 2010.

R. J. Ivison, P. P. Papadopoulos, I. Smail, T. R. Greve, A. P. Thomson, E. M. Xilouris, and S. C. Chapman. Tracing the molecular gas in distant submillimetre galaxies via CO(1-0) imaging with the Expanded Very Large Array. *MNRAS*, 412:1913–1925, April 2011.

L. Jiang, et al. Probing the Evolution of Infrared Properties of z $\sim$ 6 Quasars: Spitzer Observations. *AJ*, 132:2127–2134, November 2006.

L. Jiang, et al. A Survey of z $\sim$ 6 Quasars in the Sloan Digital Sky Survey Deep Stripe. I. A Flux-Limited Sample at $z_{AB} < 21$. *AJ*, 135:1057–1066, March 2008.

M. Joy, D. F. Lester, and P. M. Harvey. Infrared emission from young stars in the nucleus of M82. *ApJ*, 319:314–324, August 1987.

Y. Juarez, R. Maiolino, R. Mujica, M. Pedani, S. Marinoni, T. Nagao, A. Marconi, and E. Oliva. The metallicity of the most distant quasars. *A&A*, 494:L25–L28, February 2009.

M. Juvela and N. Ysard. On the Gas Temperature of Molecular Cloud Cores. *ApJ*, 739:63, October 2011.

G. Kauffmann, et al. The host galaxies of active galactic nuclei. *MNRAS*, 346: 1055–1077, December 2003a.

G. Kauffmann, et al. Stellar masses and star formation histories for 10^5 galaxies from the Sloan Digital Sky Survey. *MNRAS*, 341:33–53, May 2003b.

M. J. Kaufman, M. G. Wolfire, and D. J. Hollenbach. [Si II], [Fe II], [C II], and H_2 Emission from Massive Star-forming Regions. *ApJ*, 644:283–299, June 2006.

R. C. Kennicutt, Jr. Star Formation in Galaxies Along the Hubble Sequence. *ARA&A*, 36:189–232, 1998a.

R. C. Kennicutt, Jr. The Global Schmidt Law in Star-forming Galaxies. *ApJ*, 498: 541, May 1998b.

L. J. Kewley and S. L. Ellison. Metallicity Calibrations and the Mass-Metallicity Relation for Star-forming Galaxies. *ApJ*, 681:1183–1204, July 2008.

A. A. Klypin, S. Trujillo-Gomez, and J. Primack. Dark Matter Halos in the Standard Cosmological Model: Results from the Bolshoi Simulation. *ApJ*, 740:102, October 2011.

C. Kobayashi, V. Springel, and S. D. M. White. Simulations of Cosmic Chemical Enrichment. *MNRAS*, 376:1465–1479, April 2007.

D. D. Kocevski, et al. CANDELS: Constraining the AGN-Merger Connection with Host Morphologies at z $\sim$ 2. *ApJ*, 744:148, January 2012.

A. Kovács, S. C. Chapman, C. D. Dowell, A. W. Blain, R. J. Ivison, I. Smail, and T. G. Phillips. SHARC-2 350 μm Observations of Distant Submillimeter-selected Galaxies. *ApJ*, 650:592–603, October 2006.

P. Kroupa. On the variation of the initial mass function. *MNRAS*, 322:231–246, April 2001.

M. R. Krumholz, C. F. McKee, and J. Tumlinson. The Star Formation Law in Atomic and Molecular Gas. *ApJ*, 699:850–856, July 2009.

M. R. Krumholz, A. Dekel, and C. F. McKee. A Universal, Local Star Formation Law in Galactic Clouds, nearby Galaxies, High-redshift Disks, and Starbursts. *ApJ*, 745:69, January 2012.

M. A. Lara-López, et al. A fundamental plane for field star-forming galaxies. *A&A*, 521:L53, October 2010.

D. R. Law, C. C. Steidel, D. K. Erb, M. Pettini, N. A. Reddy, A. E. Shapley, K. L. Adelberger, and D. J. Simenc. The Physical Nature of Rest-UV Galaxy Morphology during the Peak Epoch of Galaxy Formation. *ApJ*, 656:1–26, February 2007.

V. Lebouteiller, D. J. Barry, H. W. W. Spoon, J. Bernard-Salas, G. C. Sloan, J. R. Houck, and D. W. Weedman. CASSIS: The Cornell Atlas of Spitzer/Infrared Spectrograph Sources. *ApJS*, 196:8, September 2011.

N. Lehner and J. C. Howk. A Reservoir of Ionized Gas in the Galactic Halo to Sustain Star Formation in the Milky Way. *Science*, 334:955, November 2011.

D. Leier, I. Ferreras, P. Saha, and E. E. Falco. Resolving the Baryon-fraction Profile in Lensing Galaxies. *ApJ*, 740:97, October 2011.

S. N. Leitner and A. V. Kravtsov. Fuel Efficient Galaxies: Sustaining Star Formation with Stellar Mass Loss. *ApJ*, 734:48, June 2011.

A. K. Leroy, F. Walter, E. Brinks, F. Bigiel, W. J. G. de Blok, B. Madore, and M. D. Thornley. The Star Formation Efficiency in Nearby Galaxies: Measuring Where Gas Forms Stars Effectively. *AJ*, 136:2782–2845, December 2008.

P. Lesaffre, G. Pineau des Forêts, B. Godard, P. Guillard, F. Boulanger, and E. Falgarone. Low-velocity shocks: signatures of turbulent dissipation in diffuse irradiated gas. *A&A*, 550:A106, February 2013.

S. J. Lilly, O. Le Fevre, F. Hammer, and D. Crampton. The Canada-France Redshift Survey: The Luminosity Density and Star Formation History of the Universe to Z approximately 1. *ApJL*, 460:L1, March 1996.

H. Lin, et al. Discovery of a Very Bright, Strongly Lensed z = 2 Galaxy in the SDSS DR5. *ApJ*, 699:1242–1251, July 2009.

C. J. Lonsdale, et al. SWIRE: The SIRTF Wide-Area Infrared Extragalactic Survey. *PASP*, 115:897–927, August 2003.

C. J. Lonsdale, et al. MAMBO 1.2 mm Observations of Luminous Starbursts at z $\sim$ 2 in the SWIRE Fields. *ApJ*, 692:422–442, February 2009.

S. D. Lord, D. J. Hollenbach, M. R. Haas, R. H. Rubin, S. W. J. Colgan, and E. F. Erickson. Interstellar Properties of a Dual Nuclear Starburst: Far-Infrared Spectroscopy of M82. *ApJ*, 465:703, July 1996.

M. L. Luhman, S. Satyapal, J. Fischer, M. G. Wolfire, E. Sturm, C. C. Dudley, D. Lutz, and R. Genzel. The [C II] 158 Micron Line Deficit in Ultraluminous Infrared Galaxies Revisited. *ApJ*, 594:758–775, September 2003.

D. Lutz, et al. PACS Evolutionary Probe (PEP) - A Herschel key program. *A&A*, 532:A90, August 2011.

P. Madau, H. C. Ferguson, M. E. Dickinson, M. Giavalisco, C. C. Steidel, and A. Fruchter. High-redshift galaxies in the Hubble Deep Field: colour selection and star formation history to z$\sim$4. *MNRAS*, 283:1388–1404, December 1996.

B. F. Madore. Star Formation Timescales and the Schmidt Law. *ApJL*, 716:L131–L134, June 2010.

G. E. Magdis, D. Rigopoulou, J.-S. Huang, and G. G. Fazio. On the stellar masses of IRAC detected Lyman Break Galaxies at z $\sim$ 3. *MNRAS*, 401:1521–1531, January 2010.

B. Magnelli, D. Elbaz, R. R. Chary, M. Dickinson, D. Le Borgne, D. T. Frayer, and C. N. A. Willmer. Evolution of the dusty infrared luminosity function from z = 0 to z = 2.3 using observations from Spitzer. *A&A*, 528:A35, April 2011.

R. Maiolino, et al. First detection of [CII]158 μm at high redshift: vigorous star formation in the early universe. *A&A*, 440:L51–L54, September 2005.

R. Maiolino, et al. AMAZE. I. The evolution of the mass-metallicity relation at z $>$ 3. *A&A*, 488:463–479, September 2008.

R. Maiolino, P. Caselli, T. Nagao, M. Walmsley, C. De Breuck, and M. Meneghetti. Strong [CII] emission at high redshift. *A&A*, 500:L1–L4, June 2009.

S. Malhotra, et al. Far-Infrared Spectroscopy of Normal Galaxies: Physical Conditions in the Interstellar Medium. *ApJ*, 561:766–786, November 2001.

F. Mannucci, G. Cresci, R. Maiolino, A. Marconi, and A. Gnerucci. A fundamental relation between mass, star formation rate and metallicity in local and high-redshift galaxies. *MNRAS*, 408:2115–2127, November 2010.

G. Marsden, et al. BLAST: Resolving the Cosmic Submillimeter Background. *ApJ*, 707:1729–1739, December 2009.

S. C. Marsden, I. A. Waite, B. D. Carter, and J.-F. Donati. Doppler imaging and surface differential rotation of young open cluster stars - I. HD 307938 (R58) in IC 2602. *MNRAS*, 359:711–724, May 2005.

B. Mookerjea, et al. The Herschel M 33 extended survey (HerM33es): PACS spectroscopy of the star-forming region BCLMP 302. *A&A*, 532:A152, August 2011.

G. E. Morrison, F. N. Owen, M. Dickinson, R. J. Ivison, and E. Ibar. Very Large Array 1.4 GHz Observations of the GOODS-North Field: Data Reduction and Analysis. *ApJS*, 188:178–186, May 2010.

T. Nagao, R. Maiolino, and A. Marconi. Gas metallicity diagnostics in star-forming galaxies. *A&A*, 459:85–101, November 2006.

T. Nagao, R. Maiolino, C. De Breuck, P. Caselli, B. Hatsukade, and K. Saigo. ALMA reveals a chemically evolved submillimeter galaxy at z = 4.76. *A&A*, 542:L34, June 2012.

T. Negishi, T. Onaka, K.-W. Chan, and T. L. Roellig. Global physical conditions of the interstellar medium in nearby galaxies. *A&A*, 375:566–578, August 2001.

H. T. Nguyen, et al. HerMES: The SPIRE confusion limit. *A&A*, 518:L5, July 2010.

T. Nikola, N. Geis, F. Herrmann, S. C. Madden, A. Poglitsch, G. J. Stacey, and C. H. Townes. Star Formation in M51 Triggered by Galaxy Interaction. *ApJ*, 561:203–217, November 2001.

T. Nikola, G. J. Stacey, D. Brisbin, C. Ferkinhoff, S. Hailey-Dunsheath, S. Parshley, and C. Tucker. Mid-J CO Emission from NGC 891: Microturbulent Molecular Shocks in Normal Star-forming Galaxies. *ApJ*, 742:88, December 2011.

K. G. Noeske, et al. Star Formation in AEGIS Field Galaxies since z=1.1: Staged Galaxy Formation and a Model of Mass-dependent Gas Exhaustion. *ApJL*, 660:L47–L50, May 2007.

R. Nordon, et al. The star-formation rates of $1.5 < z < 2.5$ massive galaxies. *A&A*, 518:L24, July 2010.

T. E. Oberst, et al. Detection of the 205 μm [N II] Line from the Carina Nebula. *ApJL*, 652:L125–L128, December 2006.

T. E. Oberst, S. C. Parshley, T. Nikola, G. J. Stacey, A. Löhr, A. P. Lane, A. A. Stark, and J. Kamenetzky. A 205 μm [N II] Map of the Carina Nebula. *ApJ*, 739:100, October 2011.

S. J. Oliver, et al. HerMES: SPIRE galaxy number counts at 250, 350, and 500 μm. *A&A*, 518:L21, July 2010.

S. J. Oliver, et al. The Herschel Multi-tiered Extragalactic Survey: HerMES. *MNRAS*, 424:1614–1635, August 2012.

S. Ott. The Herschel Data Processing System - HIPE and Pipelines - Up and Running Since the Start of the Mission. In Y. Mizumoto, K.-I. Morita, and M. Ohishi, editors, *Astronomical Data Analysis Software and Systems XIX*, volume 434 of *Astronomical Society of the Pacific Conference Series*, page 139, December 2010.

F. N. Owen and G. E. Morrison. The Deep Swire Field. I. 20 cm Continuum Radio Observations: A Crowded Sky. *AJ*, 136:1889–1900, November 2008.

P. P. Papadopoulos, H. J. A. Röttgering, P. P. van der Werf, S. Guilloteau, A. Omont, W. J. M. van Breugel, and R. P. J. Tilanus. CO (4-3) and Dust Emission in Two Powerful High-Z Radio Galaxies, and CO Lines at High Redshifts. *ApJ*, 528:626–636, January 2000.

A. Parravano, C. F. McKee, and D. J. Hollenbach. An Initial Mass Function for Individual Stars in Galactic Disks. I. Constraining the Shape of the Initial Mass Function. *ApJ*, 726:27, January 2011.

G. Patanchon, et al. Submillimeter Number Counts from Statistical Analysis of BLAST Maps. *ApJ*, 707:1750–1765, December 2009.

M. S. Peeples and F. Shankar. Constraints on star formation driven galaxy winds from the mass-metallicity relation at z= 0. *MNRAS*, 417:2962–2981, November 2011.

Y. Peng, S. J. Lilly, A. Renzini, and M. Carollo. Mass and Environment as Drivers of Galaxy Evolution II: The quenching of satellite galaxies as the origin of environmental effects. *ArXiv e-prints*, June 2011.

Y.-j. Peng, et al. Mass and Environment as Drivers of Galaxy Evolution in SDSS and zCOSMOS and the Origin of the Schechter Function. *ApJ*, 721:193–221, September 2010.

J. Pety, A. Beelen, P. Cox, D. Downes, A. Omont, F. Bertoldi, and C. L. Carilli. Atomic carbon in PSS 2322+1944, a quasar at redshift 4.12. *A&A*, 428:L21–L24, December 2004.

G. L. Pilbratt, et al. Herschel Space Observatory. An ESA facility for far-infrared and submillimetre astronomy. *A&A*, 518:L1, July 2010.

L. S. Pilyugin, T. X. Thuan, and J. M. Vílchez. On the origin of nitrogen. *A&A*, 397:487–501, January 2003.

A. Poglitsch, et al. The Photodetector Array Camera and Spectrometer (PACS) on the Herschel Space Observatory. *A&A*, 518:L2, July 2010.

M. Polletta, et al. The Most Obscured AGN in the Chandra/SWIRE Survey in the Lockman Hole. In A. Wilson, editor, *The X-ray Universe 2005*, volume 604 of *ESA Special Publication*, page 807, January 2006.

A. Pope, et al. Mid-Infrared Spectral Diagnosis of Submillimeter Galaxies. *ApJ*, 675:1171–1193, March 2008.

M. W. Pound and M. G. Wolfire. The Photo Dissociation Region Toolbox. In R. W. Argyle, P. S. Bunclark, and J. R. Lewis, editors, *Astronomical Data Analysis Software and Systems XVII*, volume 394 of *Astronomical Society of the Pacific Conference Series*, page 654, August 2008.

T. D. Rawle, et al. [CII] and 12CO(1-0) Emission Maps in HLSJ091828.6+514223: A Strongly Lensed Interacting System at z=5.24. *ArXiv e-prints*, October 2013.

D. A. Riechers, J. Hodge, F. Walter, C. L. Carilli, and F. Bertoldi. Extended Cold Molecular Gas Reservoirs in z $\sim$= 3.4 Submillimeter Galaxies. *ApJL*, 739:L31, September 2011.

D. A. Riechers, et al. A dust-obscured massive maximum-starburst galaxy at a redshift of 6.34. *Nature*, 496:329–333, April 2013.

B. E. Robertson and A. V. Kravtsov. Molecular Hydrogen and Global Star Formation Relations in Galaxies. *ApJ*, 680:1083–1111, June 2008.

I. G. Roseboom, et al. The Herschel Multi-Tiered Extragalactic Survey: source extraction and cross-identifications in confusion-dominated SPIRE images. *MNRAS*, 409:48–65, November 2010.

W. Rujopakarn, et al. Large Binocular Telescope and Spitzer Spectroscopy of Star-forming Galaxies at $1 < z < 3$: Extinction and Star Formation Rate Indicators. *ApJ*, 755:168, August 2012.

A. Sajina, L. Yan, L. Armus, P. Choi, D. Fadda, G. Helou, and H. Spoon. Spitzer Mid-Infrared Spectroscopy of Infrared Luminous Galaxies at $z\sim2$. II. Diagnostics. *ApJ*, 664:713–737, August 2007.

A. Sajina, et al. Spitzer Mid-Infrared Spectroscopy of Infrared Luminous Galaxies at $z \sim 2$. III. Far-IR to Radio Properties and Optical Spectral Diagnostics. *ApJ*, 683:659–682, August 2008.

D. B. Sanders and I. F. Mirabel. Luminous Infrared Galaxies. *ARA&A*, 34:749, 1996.

S. Savaglio, et al. The Gemini Deep Deep Survey. VII. The Redshift Evolution of the Mass-Metallicity Relation. *ApJ*, 635:260–279, December 2005.

M. Schmidt. The Rate of Star Formation. *ApJ*, 129:243, March 1959.

S. Serjeant. Strong biases in infrared-selected gravitational lenses. *MNRAS*, 424: 2429–2441, August 2012.

Y. Shi, G. Helou, L. Yan, L. Armus, Y. Wu, C. Papovich, and S. Stierwalt. Extended Schmidt Law: Role of Existing Stars in Current Star Formation. *ApJ*, 733:87, June 2011.

R. Siebenmorgen and E. Krügel. Dust in starburst nuclei and ULIRGs. SED models for observers. *A&A*, 461:445–453, January 2007.

J. D. T. Smith, et al. The Mid-Infrared Spectrum of Star-forming Galaxies: Global Properties of Polycyclic Aromatic Hydrocarbon Emission. *ApJ*, 656:770–791, February 2007.

P. M. Solomon, A. R. Rivolo, J. Barrett, and A. Yahil. Mass, luminosity, and line width relations of Galactic molecular clouds. *ApJ*, 319:730–741, August 1987.

H. W. W. Spoon, J. A. Marshall, J. R. Houck, M. Elitzur, L. Hao, L. Armus, B. R. Brandl, and V. Charmandaris. Mid-Infrared Galaxy Classification Based on Silicate Obscuration and PAH Equivalent Width. *ApJL*, 654:L49–L52, January 2007.

V. Springel, et al. Simulations of the formation, evolution and clustering of galaxies and quasars. *Nature*, 435:629–636, June 2005.

G. J. Stacey, S. D. Smyers, N. T. Kurtz, and M. Harwit. Observations of the 145.5 micron O I forbidden emission line in the Orion Nebula. *ApJL*, 265:L7–L11, February 1983.

G. J. Stacey, N. Geis, R. Genzel, J. B. Lugten, A. Poglitsch, A. Sternberg, and C. H. Townes. The 158 micron C II line - A measure of global star formation activity in galaxies. *ApJ*, 373:423–444, June 1991.

G. J. Stacey, et al. ZEUS: the Redshift (z) and Early Universe Spectrometer. In A. J. Baker, J. Glenn, A. I. Harris, J. G. Mangum, and M. S. Yun, editors, *From Z-Machines to ALMA: (Sub)Millimeter Spectroscopy of Galaxies*, volume 375 of *Astronomical Society of the Pacific Conference Series*, page 52, October 2007.

G. J. Stacey, et al. The Energetics of Molecular Gas in NGC 891 from H_2 and Far-infrared Spectroscopy. *ApJ*, 721:59–73, September 2010a.

G. J. Stacey, et al. A 158 μm [C II] Line Survey of Galaxies at z $\sim$ 1-2: An Indicator of Star Formation in the Early Universe. *ApJ*, 724:957–974, December 2010b.

V. Strazzullo, M. Pannella, F. N. Owen, R. Bender, G. E. Morrison, W.-H. Wang, and D. L. Shupe. The Deep Swire Field. IV. First Properties of the sub-mJy Galaxy Population: Redshift Distribution, AGN Activity, and Star Formation. *ApJ*, 714:1305–1323, May 2010.

E. Sturm, et al. Herschel-PACS spectroscopy of IR-bright galaxies at high redshift. *A&A*, 518:L36, July 2010.

A. M. Swinbank, I. Smail, S. C. Chapman, A. W. Blain, R. J. Ivison, and W. C. Keel. The Rest-Frame Optical Spectra of SCUBA Galaxies. *ApJ*, 617:64–80, December 2004.

M. Swinbank, et al. An ALMA survey of Sub-millimetre Galaxies in the Extended Chandra Deep Field South: Detection of [C II] at z=4.4. *ArXiv e-prints*, September 2012.

M. Symeonidis, et al. The Herschel census of infrared SEDs through cosmic time. *MNRAS*, 431:2317–2340, May 2013.

L. J. Tacconi, et al. High-Resolution Millimeter Imaging of Submillimeter Galaxies. *ApJ*, 640:228–240, March 2006.

L. J. Tacconi, et al. High molecular gas fractions in normal massive star-forming galaxies in the young Universe. *Nature*, 463:781–784, February 2010.

T. Takata, K. Sekiguchi, I. Smail, S. C. Chapman, J. E. Geach, A. M. Swinbank, A. Blain, and R. J. Ivison. Rest-Frame Optical Spectroscopic Classifications for Submillimeter Galaxies. *ApJ*, 651:713–727, November 2006.

T. T. Takeuchi and T. T. Ishii. A General Formulation of the Source Confusion Statistics and Application to Infrared Galaxy Surveys. *ApJ*, 604:40–62, March 2004.

A. G. G. M. Tielens and D. Hollenbach. Photodissociation regions. I - Basic model. II - A model for the Orion photodissociation region. *ApJ*, 291:722–754, April 1985.

C. A. Tremonti, et al. The Origin of the Mass-Metallicity Relation: Insights from 53,000 Star-forming Galaxies in the Sloan Digital Sky Survey. *ApJ*, 613:898–913, October 2004.

T. M. Tripp, et al. The Hidden Mass and Large Spatial Extent of a Post-Starburst Galaxy Outflow. *Science*, 334:952, November 2011.

L. Trouille, A. J. Barger, L. L. Cowie, Y. Yang, and R. F. Mushotzky. The OPTX Project. I. The Flux and Redshift Catalogs for the CLANS, CLASXS, and CDF-N Fields. *ApJS*, 179:1–18, November 2008.

I. Valtchanov, et al. Physical conditions of the interstellar medium of high-redshift, strongly lensed submillimetre galaxies from the Herschel-ATLAS. *MNRAS*, 415:3473–3484, August 2011.

P. G. van Dokkum, M. Franx, D. Fabricant, D. D. Kelson, and G. D. Illingworth. A High Merger Fraction in the Rich Cluster MS 1054-03 at Z = 0.83: Direct Evidence for Hierarchical Formation of Massive Galaxies. *ApJL*, 520:L95–L98, August 1999.

M. Vasta, M. J. Barlow, S. Viti, J. A. Yates, and T. A. Bell. Testing PDR models against ISO fine structure line data for extragalactic sources. *MNRAS*, 404: 1910–1921, June 2010.

B. P. Venemans, et al. Detection of Atomic Carbon [C II] 158 μm and Dust Emission from a z = 7.1 Quasar Host Galaxy. *ApJL*, 751:L25, June 2012.

J. Wagg, et al. [C II] Line Emission in Massive Star-forming Galaxies at z = 4.7. *ApJL*, 752:L30, June 2012.

F. Y. Wang. The high-redshift star formation rate derived from gamma-ray bursts: possible origin and cosmic reionization. *A&A*, 556:A90, August 2013.

R. Wang, et al. Star Formation and Gas Kinematics of Quasar Host Galaxies at z $\sim$ 6: New Insights from ALMA. *ApJ*, 773:44, August 2013.

T. M. Webb, et al. The Canada-UK Deep Submillimeter Survey. VI. The 3 Hour Field. *ApJ*, 587:41–54, April 2003.

J. C. Weingartner and B. T. Draine. Photoelectric Emission from Interstellar Dust: Grain Charging and Gas Heating. *ApJS*, 134:263–281, June 2001.

B. C. Whitmore and F. Schweizer. Hubble space telescope observations of young star clusters in NGC-4038/4039, 'the antennae' galaxies. *AJ*, 109:960–980, March 1995.

C. J. Willott, A. Omont, and J. Bergeron. Redshift 6.4 Host Galaxies of 10^8 Solar Mass Black Holes: Low Star Formation Rate and Dynamical Mass. *ApJ*, 770: 13, June 2013.

M. G. Wolfire, A. G. G. M. Tielens, and D. Hollenbach. Physical conditions in photodissociation regions - Application to galactic nuclei. *ApJ*, 358:116–131, July 1990.

T. Wong and L. Blitz. The Relationship between Gas Content and Star Formation in Molecule-rich Spiral Galaxies. *ApJ*, 569:157–183, April 2002.

E. L. Wright. A Cosmology Calculator for the World Wide Web. *PASP*, 118: 1711–1715, December 2006.

L. Yan, et al. Spitzer Mid-Infrared Spectroscopy of Infrared Luminous Galaxies at z $\sim$ 2. I. The Spectra. *ApJ*, 658:778–793, April 2007.

R. M. Yates, G. Kauffmann, and Q. Guo. The relation between metallicity, stellar mass and star formation in galaxies: an analysis of observational and model data. *MNRAS*, page 2572, March 2012.

H. Zinnecker and H. W. Yorke. Toward Understanding Massive Star Formation. *ARA&A*, 45:481–563, September 2007.